Advances in Additive Manufacturing and Microfabrication

by

Martin de Beer

A dissertation submitted in partial fulfillment
of the requirements for the degree of
Doctor of Philosophy
(Chemical Engineering)
in The University of Michigan
2020

Doctoral Committee:

Professor Mark A. Burns, Chair
Professor Robert Kennedy
Professor Sunitha Nagrath
Professor Shuichi Takayama

Martin de Beer

mapadebe@umich.edu

ORCID iD: 0000-0002-7839-4375

For my family and friends

ACKNOWLEDGEMENTS

Words cannot express the gratitude I have for the people who have supported me throughout my graduate degree.

My friends and family:

David for always having a good (or bad) joke;

Jeff for always being the subject of a good story;

Shreyas for literally being the best;

Ben K for being a precious angel;

Ben L for his truly atrocious puns;

Avi for always breaking things;

Soos for always bringing good tea;

Phil for DABOW and bringing us Angelo;

Angelo for living life with no pulp;

Andrew Harrison for being such a nice young man;

Leigh for always taking things to eleven;

Michael Arwashan for always being down for anything;

Brendon Baker for the countless games of squash;

My girlfriend, best friend, and worst enemy, Kathy for always supporting me with encouragement, challenging me with constant mental battles, and frustrating me with some of the literal worst jokes I have ever heard (blasters fired).

My mom for forcing me to be the best I can be, nagging me to keep my life in order,

and always being proud of me;

My dad for being a quiet role-model in my life.

My labmates:

Sarah - I hope the world never jades you;

Alyse for always giving my research unwarranted hype;

Zach for being my greatest critic;

Brian Johnson for all your help over the years;

Corine for being a great research role model;

Tatyana and Adam Krieger for great conversation.

The administrative staff:

Susan Hamlin for always keeping my head above the murky waters of grad school bureaucracy;

Barbara Perry for the patient professionalism to deal with me;

Connie Bacus for being calm in even the most stressful situations;

Kelly Raickovich for making me feel at home in the department;

Sandy Swisher for always thinking of the graduate students in the department.

My advisor Mark Burns, and collaborator Tim Scott, thank you for allowing me to pursue the research direction I found most interesting and teaching me some valuable life lessons along the way.

Anyone I have forgotten, I'm truly sorry (this was never meant to be an exhaustive list), you guys are great and it has been an absolute pleasure to work alongside you all.

TABLE OF CONTENTS

LIST OF FIGURES

Figure

LIST OF APPENDICES

Appendix

LIST OF TABLES

Table

ABSTRACT

Additive manufacturing (AM), aided by enhanced computing, unprecedented connectivity, and monumental advances in material science, has been hailed as the "fourth industrial revolution". Despite this prestigious accolade, AM-manufactured products still only represent a tiny fraction of total production. Uncompetitive fabrication speeds and directionally-dependent material properties have historically plagued AM - hindering its adoption to only a few limited applications in niche markets. Continuous stereolithographic (SL) AM offers significant improvements in fabrication speed while delivering parts with uniform material properties. This work focuses on the development of a dual-wavelength initiation and inhibition system for continuous AM. Using a visible light initiator and novel UV-active photo-inhibitor molecule we are able to generate photo-inhibited dead zones and enable continuous AM. Dead zones created in this way are large, easy-to-control and enable the fastest reported vertical print speeds for continuous SL-AM. Dual-wavelength AM methods may, through increases in fabrication rates, make AM a viable alternative manufacturing technology. A challenge in continuous AM methods is a trade-off that exists between vertical 'resolution' and speed. In order to more accurately reproduce parts, vertical resolution is typically improved (at the expense of print speed) by addition of absorbing dyes. We develop a dose-based model and correction algorithm to modify exposures in continuous AM. The algorithm uses physical properties of the system and chemical properties of the resin to calculate the cumulative dose and, through a series of constraints, optimizes the projection images used during printing to im-

prove the resolution of the printed part. This method is verified experimentally in a number of test models and actual parts and found to achieve up to 85% reduction in unwanted gelation while maintaining high print speeds up to 750 mm/hr. Multilayer microfluidic devices are useful in a wide range of applications. Fabrication of these devices, however, is often a tedious, time-consuming and expensive process. We develop a protocol for multilayer microfluidic device fabrication using our dual-wavelength initiation and inhibition system. Using grayscale patterning of the initiating light we are able to pattern microfluidic channels in a two to three short (< 30 s) exposures. This protocol is demonstrated in multilayer microfluidic device fabrication with channels of sub-millimeter height in less than a minute compared with hours or days previous methods require. Fabrication in this way may lower the barrier-to-entry of microfluidic technology for research and commercial applications. Finally we investigate a technique for fabricating variable height microfluidic channels. The fabrication technique uses controlled non-uniform exposure to an etchant solution to create channels of arbitrary height that vary from the inlet to the outlet. Channels that vary in height are shown to effectively and reproducibly separate particles by size and red blood cells by their deformability. The macroscopic visualization of microparticle separation in these devices in addition to their ease of use, simple fabrication, low cost, and small size suggest the viability of such a device in point-of-care diagnosis with multiplexed microparticle assays.

CHAPTER I

Introduction

1.1 Motivation

Additive manufacturing (AM) (or 3D printing) was born in the late 1980s from advances in computing, optics and photopolymerization chemistry. The first commercial device, the SLA-1, developed by 3D Systems used an ultraviolet laser to solidify thin layers of photo-sensitive resin to build up three dimensional objects in a process called *stereolithography* (SL). In the following years, other AM technologies, such as selective laser sintering (SLS), fused deposition modelling (FDM), and laminated object manufacturing (LOM) were introduced. The expiration of key AM patents in the 2010s released the monopolistic control over key processes held by the original pioneers - allowing numerous players into the market and subsequently lowering costs, increasing accessibility and driving innovation. While the advantages of additive manufacturing (e.g. rapid time from design to device, high customization, few geometric limitations, and low equipment cost) are widely accepted they have not translated to significant displacement of traditional manufacturing methods (such as injection molding and polymer casting). Ultimately the low-production speed, anisotropic material properties and high per-part cost relegated additive manufacturing to application in only a few niche markets (e.g. manufacturing of dental

and jewellery products). For additive manufacturing to truly be disruptive in the manufacturing space advances in production speed, part isotropy and materials properties are essential.

1.2 Prevalent Methods and Recent Advances in Additive Manufacturing

AM of 3D objects is achieved by successive addition of '2D' layers. These layers represent cross-sections or 'slices' of the original design. The way in which these layers are formed ultimately underpins the differences between AM methods. The three most commonly used techniques are fused deposition modelling (FDM), selective laser sintering (SLS), and stereolithography (SL). FDM, originally developed by Stratasys and bolstered by the RepRap movement of the early 2000s [3], is arguably the most popular and accessible 3D printing method (particularly among hobbyists and 'makers'). This method melts and extrudes thermoplastic filament from a numerically-controlled heated nozzle to form layers. Low-cost commercial FDM devices can print with a wide range of thermoplastics (e.g. polylactic acid (PLA), acrylonitrile butadiene styrene (ABS), polyethylene terephthalate (PET), and nylon), giving users access to a vast palette of material properties. Selective laser sintering (SLS) uses a high power laser to sinter layers of powdered material (typically metals, ceramics or plastic).

Of particular interest to this work, however, is stereolithography (SL). Historically, layers in stereolithography were created by curing the surface of a photo-sensitive resin vat with a UV laser beam [4]. The part was then moved into the vat and another layer created at the surface. This method required large resin baths, and the vertical fabrication speed was limited by the use of a point curing laser. Modern devices increase speed by curing entire layers with patterned light from liquid crystal

displays (LCDs) [5] or digital light projection (DLP) [6] using proprietary digital micromirror devices (DMDs) from Texas Instruments. Additionally, newer devices project light from below the resin vat through a transparent projection window (typically constructed of glass-backed polydimethylsiloxane (PDMS) or thin polymer films). While decreasing the overall size of the device and the amount of resin needed, inclusion of a projection window results in unwanted adhesion of the newly-cured layer to the window. The part thus needs to be separated and fresh resin introduced before additional layers can be added. These separation and recoating steps increase the time required for each layer, resulting in achievable print speeds of only a few millimeters per hour. Furthermore, layer-by-layer addition of material introduces directionally-dependent material properties [7].

Continuous liquid interface production (CLIP) is a major advance in stereolithography [8]. In this method, the projection window is replaced with an oxygen-permeable membrane. Oxygen, a well-known radical photopolymerization inhibitor, diffuses through the projection window and dissolves in the photopolymer resin. This results in a thin region, or *dead zone*, at the window where polymerization does not occur. The dead zone eliminates adhesion and enables material to be added in a continuous, or *layerless*, printing at unprecedented speeds and elimination of layering creates parts with isotropic material properties [9]. Liquid resin reflow into the dead zone during printing imposes a force on the growing part, the magnitude of this force is dependent on the size of the part, viscosity of the resin and height of the dead zone, and ultimately imposes a maximum size (i.e. cross sectional area) achievable with CLIP - limiting parts to sparse lattices or thin-walled structures. More recently, continuous printing was enabled through the use of a high-density fluorinated oil in place of an inhibited layer [10]. This method, unimaginatively named high area rapid

printing (HARP), claims to remove heat (which arises from the exothermic polymerization reaction) enabling large area printing (although printing of large area parts is not demonstrated). While ancillary to the discussion of continuous printing, a recently published method termed computed axial lithography (CAL) could be described as the first true 3D printing method. This method eliminates the need for cross-sectional layers altogether, instead generating a dynamically evolving light field from computed tomography which, when projected into a revolving vat of resin, cures the desired regions forming the 3D part [11]. Since parts are formed free-floating in the resin vat, parts have isotropic material properties and aren't limited by resin reflow allowing larger parts with a wider palette of material properties.

1.3 Additive Manufacturing in Microfluidic Device Construction

Microfluidic device fabrication is a tedious and time-consuming process. The prevalent fabrication method is replica molding by *soft lithography* [12]. This process creates microchannels and features by curing an elastomeric polymer (polydimethyl siloxane or PDMS) over a microfabricated master, typically SU-8 [13]. This process involves numerous time-consuming steps, making it poorly suited to mass production or rapid prototyping of devices. Additionally, any adjustments to the device design are impossible without fabrication of a new master. Multi-layered devices, which give microfluidic devices improved functionality [14], require one iteration of the entire soft lithography process for each layer (and additional steps aligning, bonding and interfacing between layers) - increasing the time, complexity and graduate student frustration of fabricating complex devices. Additive manufacturing of microfluidic devices is therefore extremely attractive due to the flexibility, short design-to-device times and ability to fabricate complex three-dimensional structures with little to no

additional effort [15, 16]. FDM and SL additive manufacturing have both demonstrated application in device [17, 18, 19, 20, 21] and mold [22, 23, 24] fabrication. As mentioned above, SL uses patterned light to cure layers of material from a liquid photopolymer resin. Typical commercial SL printers can fabricate enclosed channels of 200-300 μm [25, 20], but much smaller channels (<100 μm) are possible with custom setups and optimised resin formulations [26, 27, 28].

1.4 Organization of this Dissertation

This dissertation outlines advances in continuous additive manufacturing and microfluidic device fabrication. In chapter II, we introduce a new method for continuous additive manufacturing. This method uses complementary, orthogonal, photo-initiation and photo-inhibition chemistries individually activated by irradiation with ultraviolet and visible light. We demonstrate that this dual-wavelength chemistry is able to generate dead zones an order of magnitude larger than previously reported methods. We develop a steady-state model which accurately describes the static dead zone height under concurrent irradiation. The applicability of this new photo-initiation and photo-inhibition chemistry in a number of radical polymerization chemistries is validated. Finally, the usefulness of this chemistry in rapid additive manufacturing and topographical surface patterning is shown.

In chapter III we demonstrate a method for improving vertical print resolution, or print fidelity, in continuous additive manufacturing. We develop a model to calculate the accumulated dose from a series of image exposures during continuous AM and demonstrate its ability to gelation and the appearance of unwanted curing. We define the desirable dose profile over a given feature and fundamental constraints to achieving a particular profile in terms of physical and chemical parameters of the

system. We develop a image slice modification algorithm to computationally generate slices to correct cure errors in the continuous additive manufacturing process. Finally we experimentally demonstrate cure-through correction in a variety of continuously printed test parts and models. We discuss the benefits of slice optimization as a viable method for improving part quality while maintaining high vertical print speeds.

The application of the dual-wavelength system to *in-situ* fabrication of microfluidic devices is explored in chapter IV. We develop a transient model for gelation height under initiating and inhibiting irradiation. The conditions required, and theory of, microfluidic device fabrication with dual-wavelength photoinitiation and photoinhibition is described. A model acrylate resin is formulated, characterized, and used to demonstrate our microfabrication process. Exemplary microfluidic devices are demonstrated and the benefits of this method over conventional microfluidic device fabrication (i.e. lithography) are discussed.

In chaper V we present a new simple fabrication procedure for microfluidic channels with sloping, variable height. The usefulness of these devices in separating large numbers of microparticles and cells by differences in size and deformability is demonstrated experimentally. The potential for these devices in multi-analyte bead-based assays in point-of-care devices is discussed.

Chapter VI summarizes the conclusions and presents possible future directions for this work.

CHAPTER II

Rapid, Continuous Additive Manufacturing by Volumetric Polymerization Inhibition Patterning

This work was done in collaboration with Dr. Harry van der Laan. My contributions to this work were in the conception of a dual-wavelength system for continuous additive manufacturing, experimental work, modelling, and data analysis. Dr. van der Laan's contribution was in the FT-IR work validating the activity of *o*-Cl-HABI as a photo-inhibitor in various radical polymerizations.

2.1 Introduction

Additive manufacturing (AM) methods enable facile fabrication of exceptionally complex objects with internal features unobtainable by conventional methods [29]. Commonly called 3D printing, these technologies typically produce three-dimensional structures by successive addition of thin layers of material. The simple operation and near limitless design choice have made AM very attractive for producing custom and prototype parts [30] finding utility in applications ranging from the fabrication of bespoke medical devices [31, 32, 33] and athletic equipment tailored to an individual's anatomy [34], to the low volume production of automotive and aerospace components [35]. A wide variety of materials, including thermoplastics, polymeric resins and inorganic powders, have been employed as AM media for methods ranging from

material extrusion [36, 37, 38] to powder bed fusion [39] and binder jetting [40]. A particular method of interest, stereolithographic AM (SL or SLA) [40, 5], uses photopolymerizable resin and a patterned illumination source to cure cross-sectional layers of the desired geometry. The speed of many layer-by-layer SLA devices is, depending on the build platform translation direction, limited either by adhesion of cured polymer to the projection window or by resin surface disturbances, necessitating time-consuming separation or recoating steps between successive layers. Consequently, the print speeds in these systems range from only a few millimeters to several centimeters per hour. The recently-described continuous liquid interface production (CLIP) technique [8, 9, 41] addresses this deficiency by employing an oxygen-permeable projection window to create a thin, polymerization-free resin layer adjacent to the projection window, enabling continuous part production at translation speeds of several hundred millimeters per hour. Nevertheless, contemporary AM systems are ill-suited for the production of arbitrary 3D objects without movement of the build platform. We have developed an additive manufacturing system that can print continuously at relatively high linear velocities in addition to printing three-dimensional structures using a single exposure. Our process, shown in Fig. 2.1 uses a build head that is drawn upwards out of a photopolymerizable resin and two illumination sources at different wavelengths. Patterned illumination through a transparent glass window initiates polymerization of the resin while illumination at a second wavelength inhibits the polymerization reaction immediately adjacent to the glass window, eliminating adhesion and enabling continuous operation. Print speeds of approximately two meters per hour have been achieved, and the process is compatible with a wide variety of resins including acrylates, methacrylates, and vinyl ethers. In addition, by varying the intensity of the light source on a per-pixel

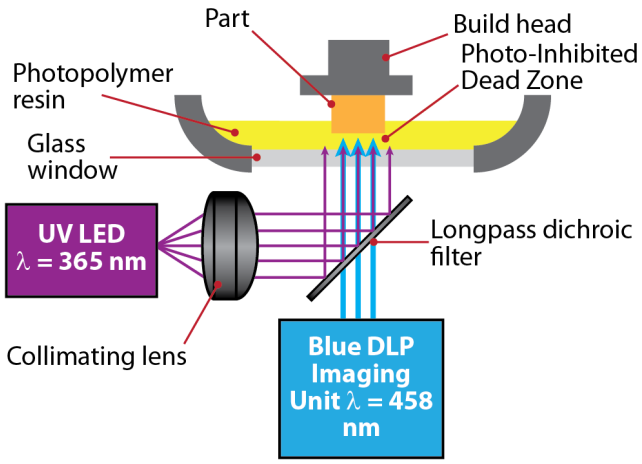

Figure 2.1: Optical setup for dual-wavelength, stereolithographic AM by concurrent photopolymerization and photoinhibition. Near UV (365 nm) is superimposed onto patterned blue (458 nm) with a dichroic mirror and projected through a transparent window into a photopolymerizable resin vat

basis, the system can perform surface topographical patterning in a single exposure with no stage translation.

2.2 Results

2.2.1 Dual-Wavelength Volumetric Photopolymerization Confinement

A unique aspect of our system is the use of multi-color irradiation to achieve volumetric patterning by the photochemical generation of both polymerization-initiating and polymerization-inhibiting species. Common amongst all contemporary SLA devices is the use of a single wavelength of light to initiate polymerization patterned in a plane. In contrast, we use one wavelength to photochemically activate polymerization and a second wavelength to inhibit that reaction. Here, photopolymerizable resins are formulated with camphorquinone (CQ, Fig. 2.2(a)) and ethyl-4-(dimethylamino)benzoate (EDAB, Fig. 2.2(b)), as a visible light photoinitiator and co-initiator, respectively [42], and bis[2-(o-chlorophenyl)-4,5-diphenylimidazole] (*o*-Cl-HABI, Fig. 2.2(c)) as a photoinhibitor. Whereas HABIs are well known as

effective photoinitiators in the presence of complementary, hydrogen-donating co-initiators [43], in the absence of co-initiators, the lophyl radicals transiently generated upon HABI photolysis efficiently inhibit radical-mediated, chain-growth polymerization (Fig. A.1) by rapidly recombining with propagating, carbon-centered radicals and thus can be used to prevent polymerization adjacent to the illumination window.

Independently controlling initiation and inhibition necessitates that photoinitiating and photoinhibiting species have complementary absorbance spectra. As shown in Fig. 2.2(d), *o*-Cl-HABI exhibits very weak absorbance in the blue region of the spectrum and moderate absorbance in the near UV, complementing the absorbance spectrum of CQ which absorbs blue light ($\lambda_{\max} = 470$ nm) but absorbs poorly in the near-UV. This minimal overlap in the absorbance spectra of CQ and *o*-Cl-HABI in the near-UV to blue region of the spectrum enables polymerization to be selectively initiated with blue light and inhibited with UV light. The dead zone height can be controlled by varying the ratio of the intensities of the two illuminating light sources. When both UV and blue light are supplied to the resin, a dead zone with no polymerization is generated adjacent to the window. Above this region, polymerization occurs allowing the continuous printing of objects, such as those shown in Fig. 2.2(f), without deleterious window adhesion. Importantly, the dead zone height (i.e., the vertical distance into the resin from the transparent window in which no polymerization occurs) is dependent on the incident initiating and inhibiting light intensities, ($I_{\text{blue},0}$ and $I_{\text{UV},0}$, respectively) such that:

$$\text{Dead Zone Thickness} = \frac{\log(\frac{\beta I_{\text{UV},0}}{I_{\text{blue},0}})}{\frac{1}{h_{\text{UV}}} - \frac{1}{h_{\text{blue}}}} \tag{2.1}$$

Here, the inhibition coefficient (β) is a constant for a given resin composition,

and incorporates the ratio of inhibitor to initiator absorbance cross sections, quantum yield, and reaction rate constants (20). The absorption height of a material, h_{UV} and h_{blue}, is defined as the inverse of the sum of the concentrations of all absorbing species (c_{i}) multiplied by their wavelength-specific absorptivity (ϵ_{i}) (i.e., $h_{\mathrm{i}} = \frac{1}{\sum \epsilon_{\mathrm{i}} c_{\mathrm{i}}}$) and is equal to the depth into an absorbing medium at which the light is 90% attenuated. Fig. 2.2(e) shows that dead zone height, calculated using a subtractive technique [8], is controlled by varying both the ratios of the incident radiation and the concentration of the UV absorber. Adjustment of $I_{\mathrm{UV},0}/I_{\mathrm{blue},0}$ changes the relative rates of initiating and inhibiting radical generation within the resin (trimethylolpropane triacrylate (TMPTA)) and can be used to control the inhibition thickness. Alternatively, the UV absorber concentration (Tinuvin 328, see Fig. A.3) can be changed to achieve a similar control over the dead zone height. Increasing the UV absorber concentration to decrease h_{UV} selectively confines UV light, and hence generation of inhibiting radicals, to progressively thinner regions above the projection window. It is important to note that a minimum intensity ratio at which initiation and inhibition rates are balanced is required to generate a dead zone and can be shown to equal $(I_{\mathrm{UV}}/I_{\mathrm{blue}})_{crit} = 1/\beta$ (see Appendix A.1). In this TMPTA-based system, $1/\beta$ is found to be approximately one; nevertheless, this value is dependent on resin composition, necessitating experimental determination for specific resin formulations. The dead zone height is a critical parameter for continuous stereolithographic fabrication. Previously reported dead zones resulting from oxygen inhibition are typically only tens of micrometers thick [8, 9]. Although this inhibition layer eliminates adhesion to the window, its small thickness curtails resin reflow underneath the emergent object, especially in objects with large cross-sectional areas [44], and necessitates the use of low viscosity resins or fabrication of objects with small cross-sections. Here, the

dead zone height can be modulated by altering the UV absorbance of the resin or by varying the intensities of the initiating and inhibiting light sources such that dead zone heights in the hundreds of microns are readily obtained. These thick dead zones are particularly desirable when using viscous resin formulations, further expanding the monomer palette, or to allow resin reflow into the print area for objects with large cross-sectional areas. Nevertheless, increases in the dead zone heights are typically accompanied by decreased polymerization rates, and hence slower print speeds, owing to attenuation of the initiation wavelength intensity within the resin bath. Notably, the system described here can negate this limitation and achieve equivalent polymerization rates for different dead zone height by accompanying any variation in the inhibition wavelength intensity with a corresponding initiation wavelength intensity change (see Fig. A.2).

2.2.2 Continuous Additive Manufacturing

The large dead zones, in conjunction with high photoinitiation rates, facilitate continuous and rapid part production. Notably, the high photoinitiation wavelength intensities that effect rapid polymerization rates also exacerbate separation and resin reflow issues in conventional and diffusion-reliant methods [8, 45]. These high rates, though, can be used in this system since the inhibiting intensity can be adjusted to maintain a constant dead zone. The maximum print speed for continuous printing in this system is a function of the absorption heights at the inhibiting and initiating wavelengths, h_{UV} and h_{blue}, the intensity of the initiating and inhibiting wavelength ($I_{\mathrm{blue},0}$ and $I_{\mathrm{UV},0}$ here respectively), and the amount of energy required to cure the resin, E_c, such that (see Appendix A.2):

$$\text{Max. Print Speed} = \frac{I_{\mathrm{blue},0} h_{\mathrm{blue}} - \beta I_{\mathrm{UV},0} h_{\mathrm{UV}}}{E_{\mathrm{c}}} \tag{2.2}$$

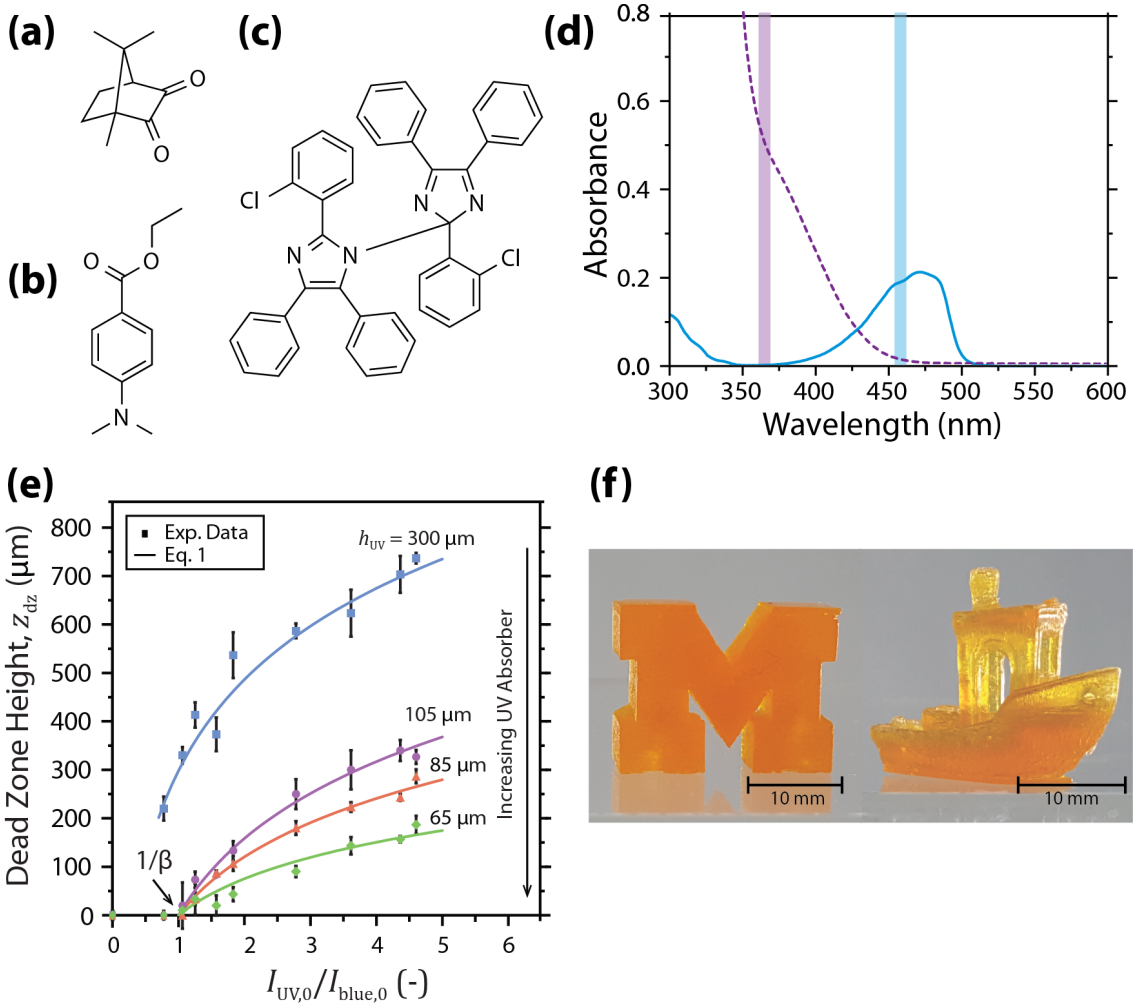

Figure 2.2: Structures of (a) photoinitiator CQ, (b) co-initiator EDAB, and (c) photoinhibitor *o*-Cl-HABI. (d) UV-visible spectra of CQ (solid blue line) and *o*-Cl-HABI (dashed violet line) in THF. The UV and blue wavelengths employed by the two-color AM system are highlighted by the violet and blue vertical bars, respectively. (e) The dead zone height is affected by varying intensity ratios of the incident irradiation wavelengths ($I_{\mathrm{UV},0}/I_{\mathrm{blue},0}$) and resin absorbance ($h_{\mathrm{UV}}$). (f) A solid block M (left) and tug boat (model detailed in [1]) (right) printed using the two-color, photopolymerization/photoinhibition stereolithography system at 500 mm/hr and 375 mm/hr, respectively.

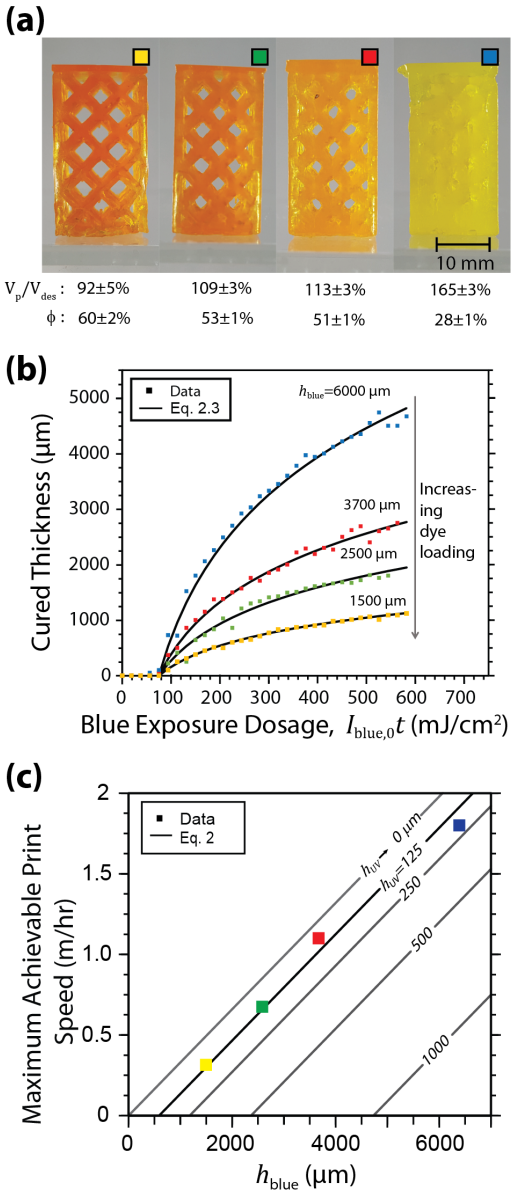

Figure 2.3: Rapid, continuous additive manufacturing with two-color photoinitiation and photoinhibition. (a) Argyle models printed using photoinhibition to enable continuous printing, with the percentage void (ϕ) and volume of the printed part (V_p) relative to the designed part (V_des) shown below each part. The designed void was $\phi = 57\%$. (b) Cured thickness versus dosage of blue light for four acrylate-based resin formulations prepared with varying blue-absorbing dye (Epolight 5675) loadings. (c) Maximum vertical print speeds achievable for varying blue absorbance heights. All printing was done with $I_{\mathrm{blue},0}$ of 110 mW/cm^2 and $I_{\mathrm{UV},0}$ of 130 mW/cm^2 with h_UV of 125 μm. The influence of varying h_UV, and hence dead zone height, on the predicted maximum achievable print speed as determined by Eq. 2.2, are shown as solid lines.

Reducing the dead zone height by decreasing h_{UV} at constant irradiation intensity is predicted to increase print speeds as polymerization proceeds closer to the projection window where limited blue light attenuation affords high initiation wavelength intensity. Practically, the theoretical maximum print speed is difficult to achieve owing to lingering inhibiting radicals, mechanical properties of the cured resin, and reflow limitations dictated by the resin viscosity. Nevertheless, we are able to print parts at speeds up to approximately 2 meters per hour for the argyle structures shown in Fig. 2.3(a).

In this system, the depth to which light penetrates and ultimately cures resin is controlled by modulating the resin's blue absorbance (Fig. 2.3(b)) with the cured thickness for a given irradiation dose of initiating light given by:

$$\text{Cured Thickness} = h_{\mathrm{blue}} \log\left(\frac{I_{\mathrm{blue},0} t}{E_{\mathrm{c}}}\right) \tag{2.3}$$

where $I_{\mathrm{blue},0}t$ [46] is the product of the irradiation intensity and time, or the incident dose. At the slowest print speed, the apparent void percentage of the printed argyle structure exceeded that of the design (Fig. 2.3(a)), attributable to polymerization-induced shrinkage [47]; however, deviation of the printed part volumes from their design increased with raised print speed, due to unwanted polymerization beyond the designed feature (known as "cure-through"). Although adding blue-absorbing dyes (e.g., Epolight 5675, see Fig. A.3) can rectify cure-through to improve the fidelity of printed parts to their design, a compromise between vertical resolution and print speed exists in continuous AM systems (Fig. 2.3(c)), as has been previously reported (15). Print fidelity can also be improved by using resin formulations that exhibit inherently low polymerization shrinkage or by modifying the projected images to correct for shrinkage. Nevertheless, increasing the print speed at

a constant dye loading results in decreased gel fractions of the completed part (see Fig. A.5) owing to lower light doses for faster-printed parts.

2.2.3 Hexaarylbiimidazoles as Radical Polymerization Photoinhibitors

The concurrent photoinitiation and photoinhibition described here can be applied to a range of monomer classes for use in this AM system. HABIs exhibit several attributes favoring their potential as universal photoinhibitors of radical-mediated, chain-growth polymerizations, including their favorable absorbance spectra and the inability of HABI-derived lophyl radicals to directly initiate polymerization of (meth)acrylates [48], greatly expanding the compatible monomer palette. To demonstrate the broad applicability of our photoinitiator/photoinhibitor system, acrylate, methacrylate, and vinyl ether/maleimide (i.e., electron donor and electron acceptor monomers) resins (see Fig. 2.4(a)-(e)) formulated with CQ, EDAB, and *o*-Cl-HABI displayed rapid curing upon blue irradiation, suggesting that the HABI did not produce polymerization rate-retarding chain transfer reactions, and, while under exclusive near UV irradiation, very limited to no curing was observed. Upon concurrent blue and near-UV irradiation, polymerization rates decreased precipitously relative to those observed under exclusively blue irradiation for all resin formulations examined, approaching zero for the (meth)acrylates (Fig. 2.4(f)-(h)). Note that other two-color irradiation schemes have been demonstrated previously for sub-diffraction, direct-write photolithography [49, 50, 51]. These systems used CQ and EDAB as a blue light photoinitiator system and tetraethylthiuram disulfide (TETD) as a UV-active photoinhibitor. Unfortunately, the utility of TETD in rapid additive manufacturing is hindered by its participation in chain transfer reactions with propagating radical species [52], resulting in significantly reduced photopolymerization rates at raised TETD concentrations even under exclusively photoinitiating irradia-

tion, while co-irradiation at the photoinhibition wavelength yields reduced polymerization rates but does not completely cease polymerization [49]. Moreover, TETD has only been shown to effectively inhibit methacrylate resins, limiting the palette of compatible monomers.

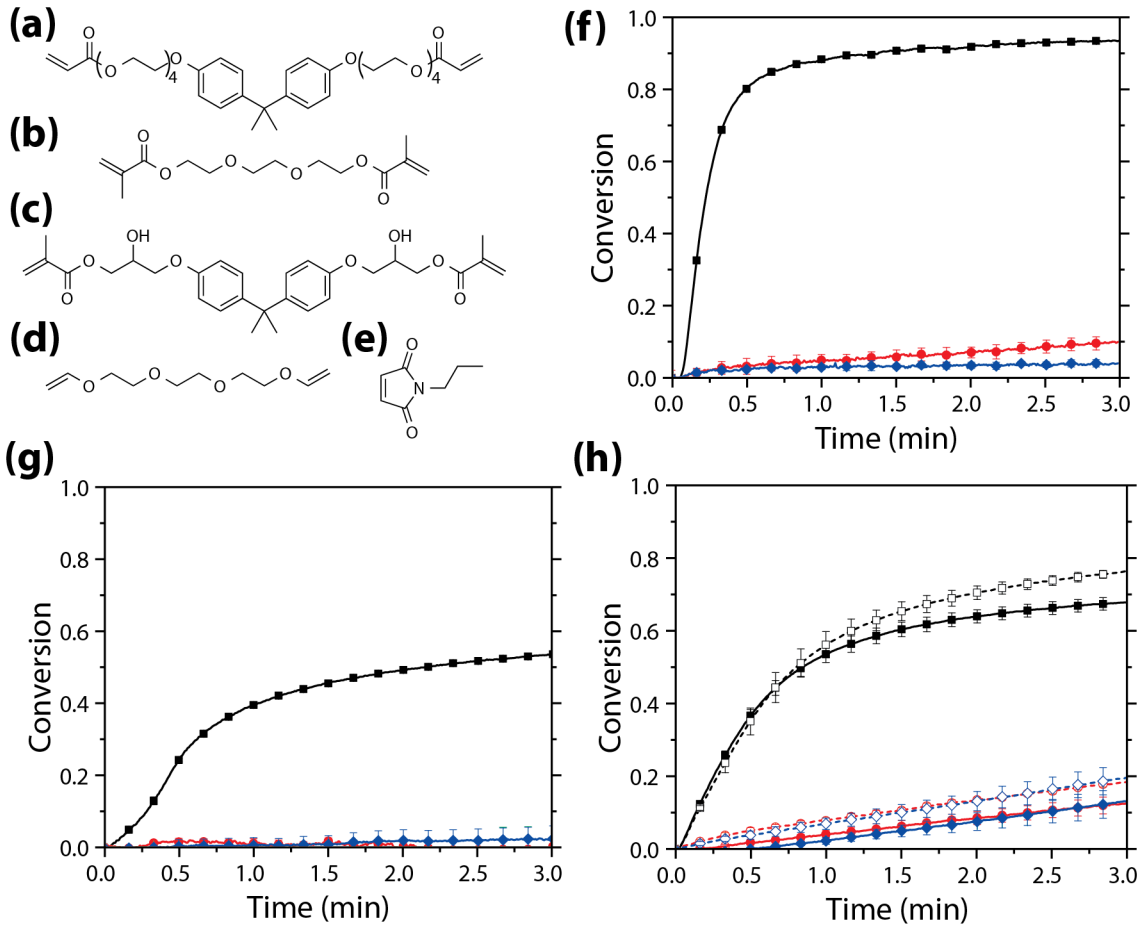

Figure 2.4: Wavelength-selective photoinitiation and photoinhibition of radical-mediated, chain growth photopolymerization. Monomers examined include (a) bisphenol A ethoxylate diacrylate (BPAEDA, n $\approx$ 4); (b) triethylene glycol dimethacrylate (TEGDMA); (c) bisphenol A glycerolate dimethacrylate (bisGMA); (d) triethylene glycol divinyl ether (TEGDVE); and (e) N-propylmaleimide (NPM). Alkene conversion versus time for resin formulations of (f) BPAEDA, (g) bisGMA/TEGDMA,and (h) TEGDVE/NPM (vinyl ether and maleimide conversions denoted by solid and dashed lines, respectively) under continuous irradiation with exclusively 470 nm @ 100 mW/cm^2 (black line, squares), 470 nm @ 100 mW/cm^2 and 365 nm @ 30 mW/cm^2, (red line, circles), and 365 nm @ 30 mW/cm^2 (blue line, diamonds).

2.2.4 Single Exposure Surface Topographical Patterning

A significant and unique attribute of our system is that, by employing the concurrent photoinitiation and photoinhibition in conjunction with spatial variation in light intensity, our system has the ability to produce complex, three-dimensional surface features with a single, two-color exposure. Projecting blue images of variable intensities (i.e., varying the intensity on a pixel-by-pixel basis) against a constant UV background affords spatial variation of $I_{\mathrm{UV},0}/I_{\mathrm{blue},0}$, consequently varying the dead zone height according to Equation 2.1. This modulation creates a complex, three-dimensionally patterned dead zone and enables localized surface patterning of features, both of which are unattainable by current methods. Fig. 2.5(a) shows a schematic of this procedure where the single-exposure topographical patterning was demonstrated with resin formulated with CQ/EDAB and *o*-Cl-HABI contained between two glass slides. The resin was exposed to a blue image of varying intensity, and this image was superimposed on a uniform, collimated UV light source (Fig 2.5(a)). A single ten second exposure yields cured features with a thickness variation of up to 700 μm and height differences as small as 125 μm (Fig. 2.5(b)); however, these magnitudes can be readily varied by adjusting the UV- and blue-absorbing dye loadings to refine the wavelength-dependent absorption characteristics of the resin (i.e., by adjusting h_{UV} and h_{blue}). The ability to use this technique to produce patterned features with three-dimensional structures is demonstrated with a four intensity-level image (Fig. 2.5(c)). The cured resin resulting from exposure to the image in Fig. 2.4(c) shows the expected variation in thickness (Fig. 2.5(d)), with the 200 μm text features able to be easily resolved.

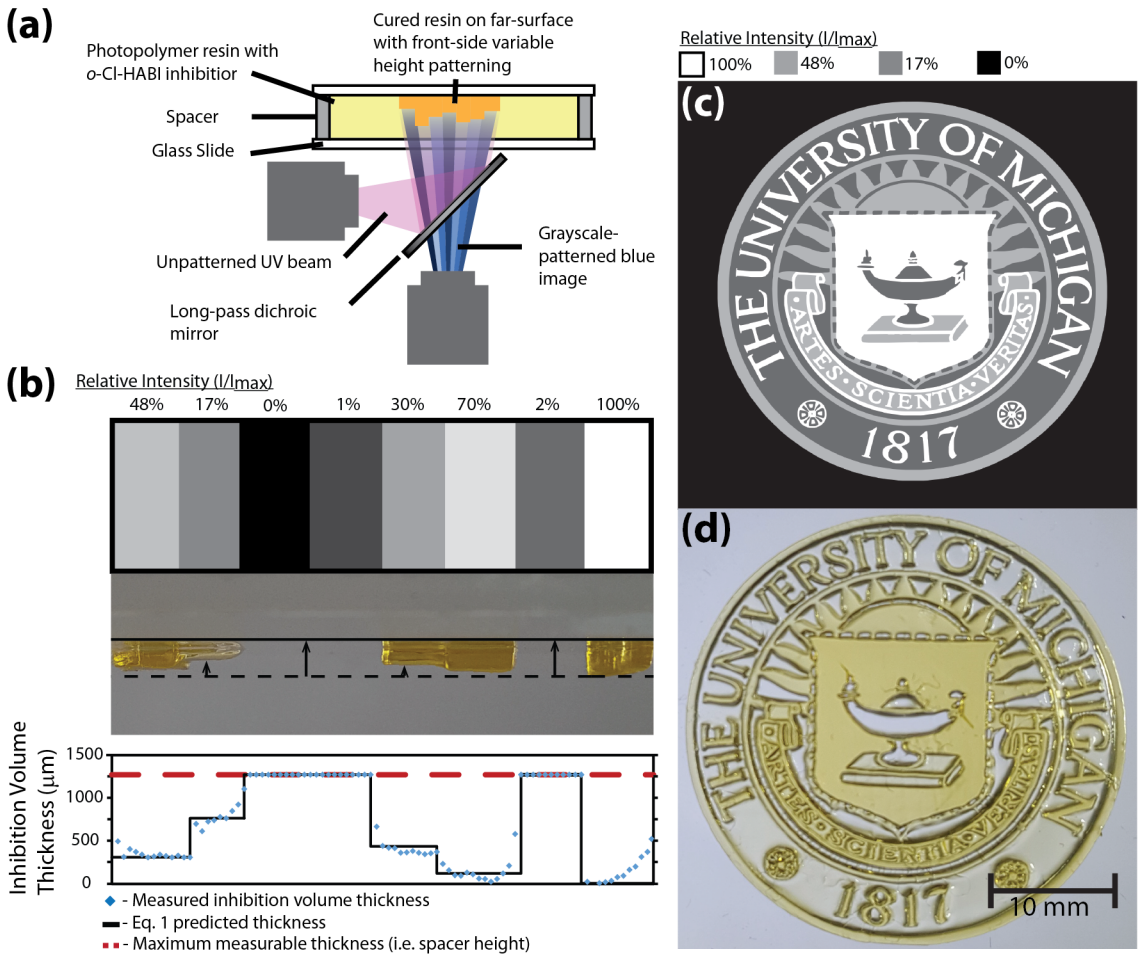

Figure 2.5: Two-color photoinitiation and photoinhibition enables controllable, far-surface patterning of complex 3D structures. (a) Setup used for intensity-patterned printing. (b) Use of variable intensity images enables pixel-wise adjustment of $I_{\mathrm{UV},0}/I_{\mathrm{blue},0}$, producing variation in inhibition height and, therefore, printed part topography. (c) Four-level intensity image of the University of Michigan seal. (d) Variable thickness part produced by a single, intensity-patterned exposure.

2.3 Discussion

The controllable, concurrent photoinitiation and photoinhibition used in this fabrication system has, in addition to high vertical print speeds, considerable advantages over contemporary approaches. By eliminating the need for thin, O_2-permeable projection windows this process has the potential to be scaled for rapid production of very large objects. Moreover, by dynamically controlling inhibition using this

method, reflow into the dead zone during printing can be optimized to ameliorate reflow problems associated with production of large cross-sectional area parts, significantly broadening the applicability of AM for mass production. Using variable-intensity irradiation with concurrent photoinitiation and photoinhibition allows single step fabrication of cured materials with intricate surface topographies, enabling rapid generation of personalized products or overcoming numerous time-consuming steps currently used in microfabrication. The application of multi-wavelength systems to SLA is a new direction in additive manufacturing where, in addition to the volumetric polymerization control described here, two-color systems designed to effect orthogonal reactions may enable fabrication of parts with localized variation of material and chemical properties [53].

2.4 Materials and Methods

Triethylene glycol dimethacrylate (TEGDMA, Esstech Inc., Essington, PA, USA) and bisphenol A glycidyl methacrylate (bisGMA, Esstech) were formulated as a mixture consisting of 50 wt.% TEGDMA and 50 wt.% bisGMA. N-(n-propyl)maleimide (NPM, Alfa Aesar, Haverhill, MA, USA) and triethylene glycol divinyl ether (TEGDVE, Sigma-Aldrich, St. Louis, MO, USA) were formulated as a mixture such that the maleimide and vinyl ether functional groups were present at a 1:1 stoichiometric ratio. Bisphenol A ethoxylate diacrylate, EO/phenol 4.0 (BPAEDA, Sigma-Aldrich) was used without comonomers. (±)-Camphorquinone (CQ, Esstech) was used as a blue light-active photoinitiator in conjunction with ethyl-4-dimethylaminobenzoate (EDAB, Esstech) as a co-initiator at the concentrations indicated. 2,2'-Bis(2-chlorophenyl)-4,4',5,5'-tetraphenyl-1,2'-biimidazole (*o*-Cl-HABI, TCI America, Portland, OR, USA) was used as a photoinhibitor at the concen-

trations indicated. Owing to poor solubility of *o*-Cl-HABI in the monomers, *o*-Cl-HABI was dissolved in tetrahydrofuran (THF, containing 0.025% butylated hydroxytoluene as preservative, Fisher Scientific, Hampton, NH, USA) as a 30 wt.% solution prior to formulating the resins. The bisGMA/TEGDMA monomer mixture was formulated with 0.2 wt.% CQ, 0.5 wt.% EDAB, and 3 wt.% *o*-Cl-HABI. BPAEDA was formulated with 0.2 wt.% CQ, 0.5 wt.% EDAB, and 2 wt.% *o*-Cl-HABI. The TEGDVE/NPM monomer mixture was formulated with 1.0 wt.% CQ, 0.5 wt.% EDAB, and 5 wt.% *o*-Cl-HABI. All monomer quantities were adjusted to account for the THF in which *o*-Cl-HABI was dissolved. For the *o*-Cl-HABI photoinitiation testing, bisGMA/TEGDMA was formulated with 1 wt.% *o*-Cl-HABI and either no co-initiator or 0.5 wt.% of either EDAB or 2-mercaptobenzothiazole (MBT, Sigma-Aldrich). Photopolymerizable resins for 3D printing were prepared with a 1/0.5/3 wt.% mixture of CQ, EDAB, and *o*-Cl-HABI, respectively. Dead zone height tests were conducted with exclusively trimethylolpropane triacrylate (TMPTA, Alfa Aesar) as monomer. Resins used for continuous 3D printing and varying intensity printing were mixtures of monomers, oligomers and reactive diluents, including TMPTA, TEGDMA, 1,6-hexandiol diacrylate (HDDA, TCI America, Portland, OR, USA), Sartomer CN2920 (Sartomer, Exton, PA, USA), Sartomer CN981 (Sartomer), and isobornyl acrylate (TCI America). Tinuvin 328 (BASF, Florham Park, NJ, USA) was used as a UV absorber and Epolight 5675 (Epolin, Newark, NJ, USA) was used as a blue light absorber. All chemicals were used as received. All polymerizations were conducted at room temperature.

2.4.1 UV-Vis Spectrophotometry

UV-visible spectrophotometry was performed on 1 wt.% solutions of *o*-Cl-HABI and CQ in tetrahydrofuran, and 1.1×10^{-4} M Tinuvin 328 and 1×10^{-2} g/L Epolight

5675 in isopropyl alcohol using an Agilent Technologies Cary 60 UV-Vis spectrophotometer. Spectra were collected from 200 to 800 nm with 1 nm spacing on solutions using a 1 mm path length quartz cuvette in the dark.

2.4.2 FT-IR Spectroscopy

Blue light was provided by a collimated, LED-based illumination source (Thorlabs M470L3-C1) with an emittance centered at 470 nm (FWHM 25 nm), used in combination with a current-adjustable LED driver (Thorlabs LEDD1B) for intensity control. UV light was provided by a UV spot curing system (Omnicure LX500, Excelitas Technologies) equipped with an Omnicure LED MAX head with an emittance centered at 365 nm. Irradiation intensities were measured with an International Light IL1400A radiometer equipped with a GaAsP Detector (model SEL005), a 10× attenuation neutral density filter (model QNDS1), and a quartz diffuser (model W). Resin formulations were introduced between NaCl crystal windows (International Crystal Laboratories) separated by spacers (26 μm thick for bisGMA/TEGDMA, 51 μm thick for BPAEDA, and 13 μm NPM/TEGDVE to maintain constant sample thickness during polymerization. Each sample was placed in a Thermo Scientific Nicolet 6700 FTIR spectrometer equipped with a horizontal transmission accessory, as described previously [54], and spectra were collected from 650 to 4000 cm^{-1} at a rate of 2 Hz. The functional group conversion upon irradiation was determined by monitoring the disappearance of the peak area centered at 1635 cm^{-1} for the methacrylate stretch, 1636 cm^{-1} for the acrylate stretch, 1618 cm^{-1} for the vinyl ether stretch, and 829 cm^{-1} for the maleimide C=C double bond stretch. The respective sample thicknesses for the formulations were chosen to ensure that the functional group peaks remained within the linear regime of the instrument detector while affording good signal to noise and maintaining optically thin and isothermal

polymerization conditions. All experiments were performed in triplicate, and the photoinitiator and photoinhibitor concentrations and irradiation intensities were as indicated in the materials section and figure captions.

2.4.3 Dead zone thickness measurements

UV light from a high powered light emitting diode (LED) (λ_{max} = 365 nm, 1400 mA, Thorlabs #M365LP1) was collimated using an aspheric condenser lens (ϕ=2 in., f=32 mm, NA=0.76, Thorlabs #ACL50832U) and focused with an adjustable collimation adapter (Thorlabs #SM2F). Optical components were held in place with a 60 mm cage cube system (Thorlabs #LC6W). A high powered blue LED (λ_{max} = 458 nm, I_F=1400 mA, Osram LE B Q7WP-5C8C-24) was retrofitted into a commercial DLP projector (Optoma ML750). Light from the blue projection system passed through a bi-convex (ϕ=2 in., f=100 mm, NA=0.76, Thorlabs LB1630) lens to reduce the focal distance and superimposed with the UV light using a longpass dichroic mirror (ϕ2", 425 nm cutoff, Thorlabs DMLP425L). The UV LED was driven by a BuckPuck LED driver (I=1000 mA, LEDdynamics Inc. 3023-D-E-1000) and the blue LED was driven by a constant current power supply (10000 mA, Mean Well HLG-120H-12B). The intensity of the LEDs were controlled using a custom LabVIEW virtual instrument (VI) which output a 0-5 V analog signal to adjust the current from the LED driver. Light intensity at a given voltage was calibrated by using an International Light IL1400A radiometer. 800 μm thick, 3D printed (Markforged Mark II, Nylon) spacers were affixed to a glass slide using epoxy adhesive to create a well for the photopolymer. Resin was pipetted into the well and sealed with another glass slide. The resin was then cured for 10 s at I_{blue} = 78.5 mW/cm^2 under varying UV irradiation intensities to give $0 < I_{UV}/I_{blue} < 2$. The cured resin was rinsed using isopropanol and re-exposed to blue light for an additional minute to

complete curing. The thickness of the cured part was measured with a micrometer. The height of the dead zone was then calculated from $h_{\mathrm{IV}} = h_{\mathrm{s}} - h_{\mathrm{c}}$ where h_{IV}, h_{s}, and h_{c} are the heights of the dead zone, spacer, and cured plug, respectively.

2.4.4 Continuous 3D Printing

A custom build head was designed using Autodesk Fusion 360 and fabricated with nylon using 3D printing (Markforged Mark II). A metal base plate was attached at the base of the build head using two wingnuts. The build head was attached to a commercially available linear screw actuator (Rattmmotor CBX1605-300A) to enable vertical motion. Motion was controlled using an on/off digital signal from a custom LabVIEW VI to start/stop a signal from a signal generator (Agilent 33220A). Models were designed using DesignSpark Mechanical 2.0 or Autodesk Fusion 360 and exported as STL files. Image slices were created from STL files using the slicing feature in Autodesk Netfabb 2017. All models were sliced using a slice height of 25 μm to ensure a short slicing time while maintaining good feature resolution. During printing, image slices were displayed concurrently with movement of the build head using a LabVIEW VI. Parts were rinsed with isopropanol after printing to remove uncured resin.

2.4.5 Gas Pycnometry

A gas pycnometer (MVP-60C, Quantachrome Instruments) was used to measure the volume of 3D printed parts. Each sample mass was placed in a cylindrical sample cell and pressurized with helium gas. The release of pressure resulted in the volume expansion of helium gas, which was converted to volume of the sample.

2.4.6 Determination of Gel Fraction

Samples prepared through continuous 3D printing were dried in the dark at 60°C for 24 hours and weighed. The samples were then extracted with THF for 24 hours using a Soxhlet apparatus, dried again at 60°C for 24 hours and weighed to determine lost mass.

CHAPTER III

Modelling and Correcting Cure-Through in Continuous Stereolithographic 3D Printing

This work was done in close collaboration with Mr. Zachary Pritchard. My contributions to this work were in the formulation of the project, discussions with Mr. Pritchard, experimental validation of the model and data analysis.

3.1 Introduction

Additive manufacturing (AM), commonly called 3D printing, refers to a number of technologies through which objects are created by progressive addition of material.[55, 56] With its simplicity and nearly unlimited design choice, AM is attractive for producing custom, limited-quantity, and prototype parts. AM has found numerous applications in fields including biomedical engineering,[57, 58, 59, 60, 61] bio-inspired materials,[62, 63, 64] functional materials,[65, 66, 67, 68, 69, 70, 71] and the DIY "maker" industry.[72] In projection stereolithography, a widely-used AM method, photopolymerizable resin is exposed to patterned light to cure cross-sections of a desired 3D part. Typically, stereolithography produces parts in discrete layers. Exposed areas are cured through the full layer height, whereupon the part is repositioned and recoated with resin before the next layer is exposed. Recently, continuous stereolithographic technologies have been developed which increase print

speeds by eliminating the time-consuming repositioning and recoating steps.[8, 73] Print speed in continuous stereolithography is dependent on the resin absorbance height, with low-absorbance resins allowing extremely high print speeds of up to 2,000 mm h^{-1} at the cost of part fidelity.

In stereolithography, the penetration depth of light in the resin limits accuracy along the vertical axis: unaccounted-for light propagation can cause undesired curing, known as cure-through, overcure,[74, 75] the back-side effect,[20] or print-through error.[8, 76] This phenomenon can also contribute to cross-linking heterogeneity, introducing internal stresses which can deform the part and further reduce fidelity.[28] The prevalent strategy to mitigate cure-through is to add nonreactive light absorbers to the resin formulation.[74, 27, 77, 78, 28] Highly-absorbing resins have been widely adopted despite the slower print speeds needed to ensure fully cured layers. Alternatively, cure-through can be mitigated without sacrificing speed by modifying the projected images (slices) based on modelling of the curing process. Optimization-based methods to eliminate cure-through by adjusting model dimensions have been developed for external surfaces and internal voids in traditional stereolithography.[75, 76, 79] Manual adjustments to account for cure-through have also been reported.[80]

Nevertheless, slice correction has not been described for continuous stereolithography, where cure-through is a more significant and complex problem. Furthermore, existing models of continuous stereolithography are not tailored to this application.[81, 82, 83]

Here, we present a curing model and a slice correction algorithm for continuous stereolithography. Previous non-continuous approaches used iterative and heuristic processes to find optimal corrections and were restricted to black and white pix-

els; our correction method uses grayscale, which has previously only been used to improve lateral resolution,[84] along with an exact mathematical solution to precisely set the dose profile within a part. We also present experimental validation of our model and correction approach using a recently-developed two-color continuous stereolithographic 3D printer.[73]

Figure 3.1(a) shows how our correction process fits into the existing 3D printing workflow. To demonstrate the applicability of the slice correction method to typical parts, we printed corrected and uncorrected versions of two open-source models (Figure 3.1(b – c)).[85, 2] In both cases, parts printed with uncorrected slices significantly deviate from the design as a result of cure-through. Applying slice correction to these parts significantly reduces the occurrence of cure-through, with corrected parts showing increased accuracy in the z-direction.

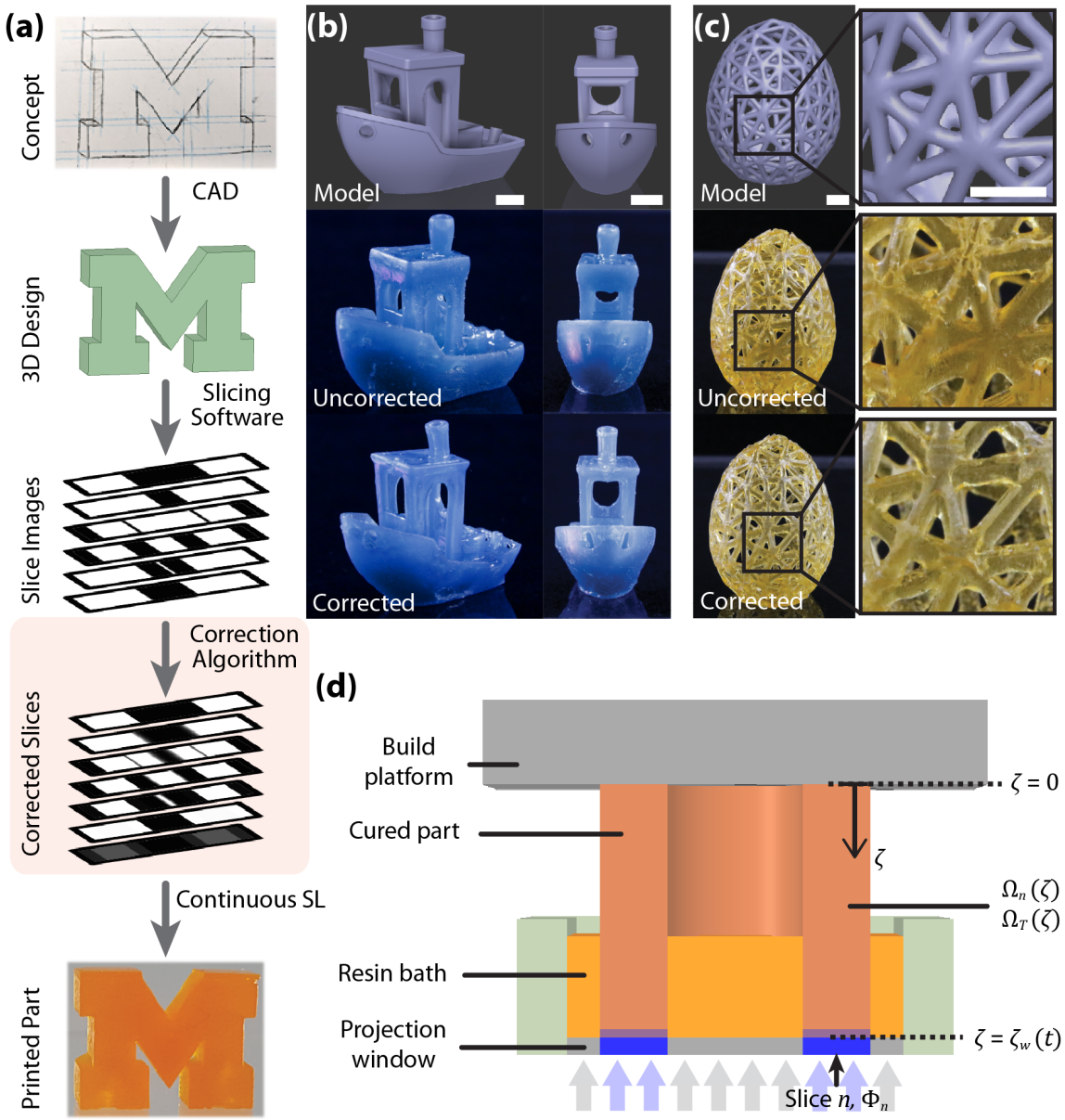

Figure 3.1: a) Cure-through correction is incorporated into the 3D printing workflow by computationally processing slice images. b,c) Correction applied to real models, reducing the extent of cure-through while maintaining print speed. Scale bars are 5 mm. b) #3DBenchy [1] printed at 800 mm h^{-1} (h_a = 1500 μm, D_c = 230 mJ cm^{-3}), and c) hollow egg [2] printed at 800 mm h^{-1} (h_a = 2000 μm, D_c = 173 mJ cm^{-3}). d) Vertical cross-section of printer setup showing nondimensionalized variables of interest: ζ, Ω_n, and Φ_n are the dimensionless z-position, dose, and light intensity, respectively.

3.2 Results and Discussion

3.2.1 Dose-Based Correction for Continuous 3D-Printing

A schematic of the printer and coordinate system is shown in Figure 3.1(d). The coordinate system is defined with respect to the build platform, with $z = 0$ at the platform and increasing towards the projection window (i.e., downward). The coordinates x and y are omitted from our notation for simplicity; however, the presented equations must be applied at fixed (x, y) positions since the projected slices are patterned. The build platform begins in contact with the window and continuously moves upward while printing. The curing model, then, includes simultaneous continuous and discrete processes: as the build platform continuously ascends, exposure patterns change at discrete intervals with each slice projected in sequence. To account for the discrete projection of slices, the total accumulated dose at a point is a sum of contributions from each slice projected. $D_{\mathrm{T}}(z)$ is the total dose delivered to position z in the final part, and the contribution of slice n to the total dose is $D_{\mathrm{n}}(z)$. Thus, $D_{\mathrm{T}}(z) = \sum_{\mathrm{n}=0}^{N} D_{\mathrm{n}}(z)$ where slices are numbered from zero to N in order of exposure. From Beer's Law, the time-derivative of dose as a slice is projected is

$$\frac{d}{dt} D_{\mathrm{n}}(z,t) = I_{\mathrm{n,w}} 10^{-[z_{\mathrm{w}}(t)-z]h_{\mathrm{a}}^{-1}} \tag{3.1}$$

where $I_{\mathrm{n,w}}$ is the light intensity at the window, $z_{\mathrm{w}}(t)$ is the time-varying position of the window, and h_{a} is the resin absorbance height (i.e., the inverse of the absorption coefficient). With the build platform continuously ascending, $D_{\mathrm{n}}(z)$ is determined for each slice by integrating over the time period when the slice is projected. Since the coordinate system is fixed with respect to the build platform, time-dependence can be incorporated via the continuously increasing value of $z_{\mathrm{w}}(t)$ and the print speed $s = dz_{\mathrm{w}}/dt$. Integrating Equation 3.1 over the exposure of slice n yields Equation

3.2:

$$D_{\mathrm{n}}(z) = \frac{I_{\mathrm{n,w}} h_{\mathrm{a}}}{s \ln 10} (10^{-(n h_{\mathrm{s}} - z) h_{\mathrm{a}}^{-1}} - 10^{-[(n+1) h_{\mathrm{s}} - z] h_{\mathrm{a}}^{-1}}) \tag{3.2}$$

where h_{s} is the slicing height. Equation 3.2 applies if the cross-section at height z is exposed to slice n (i.e., when $z \leq \mathrm{n} h_{\mathrm{s}}$); otherwise, $D_{\mathrm{n}}(z) = 0$. The total accumulated dose at a point, $D_{\mathrm{T}}(z)$, is obtained by summing Equation 3.2 over all slices to which z is exposed:

$$D_{\mathrm{T}}(z) = \sum_{n=z h_{\mathrm{s}}^{-1}}^{N} \frac{I_{\mathrm{n,w}} h_{\mathrm{a}}}{s \ln 10} (10^{-(n h_{\mathrm{s}} - z) h_{\mathrm{a}}^{-1}} - 10^{-[(n+1) h_{\mathrm{s}} - z] h_{\mathrm{a}}^{-1}}) \tag{3.3}$$

or, in dimensionless form,

$$\Omega_{\mathrm{T}}(\zeta) = \sum_{n=\zeta}^{N} \Phi_{\mathrm{n}} (10^{-(n-\zeta)\eta} - 10^{-[(n+1)-\zeta)]\eta}) \tag{3.4}$$

with dimensionless variables $\Omega \equiv D D_{\mathrm{c}}^{-1}$ (where D_{c} is the experimentally determined critical dose), $\zeta \equiv z h_{\mathrm{s}}^{-1}$, $\Phi \equiv I_{\mathrm{w}} I_{\mathrm{c}}^{-1}$ (where I_{c} is the minimum intensity needed to reach D_{c}), and $\eta \equiv h s h a^{-1}$. Equation 3.4 allows calculation of Ω_{T} for any integer value of ζ in the final printed part. Equation 3.4 can be simplified to quickly perform dose calculations and slice corrections by writing $\Omega_{\mathrm{T}}(\zeta)$ as a function of $\Omega_{\mathrm{T}}(\zeta + 1)$:

$$\Omega_{\mathrm{T}}(\zeta) = \Omega_{\zeta}(1 - 10^{-\eta}) + \Omega_{\mathrm{T}}(\zeta + 1) 10^{-\eta} \tag{3.5}$$

Starting at the bottom of the part (i.e., $\zeta = N$) and moving upwards, the total dose may be calculated for each integer value of ζ by considering only the current layer and the preceding layer. Expressions for Ω_{T} at several values of ζ, along with a full derivation, are available in Appendix B.1. The above mathematical model allows calculation of the accumulated optical dose at any position in the part and any time in the printing process. Since D_{c} defines the threshold for curing, an accurate dose profile has $\Omega_{\mathrm{T}} \geq 1$ within designed features and $\Omega_{\mathrm{T}} < 1$ outside features. At

points where these conditions are not met, the printed part will exhibit undercure or cure-through artifacts.

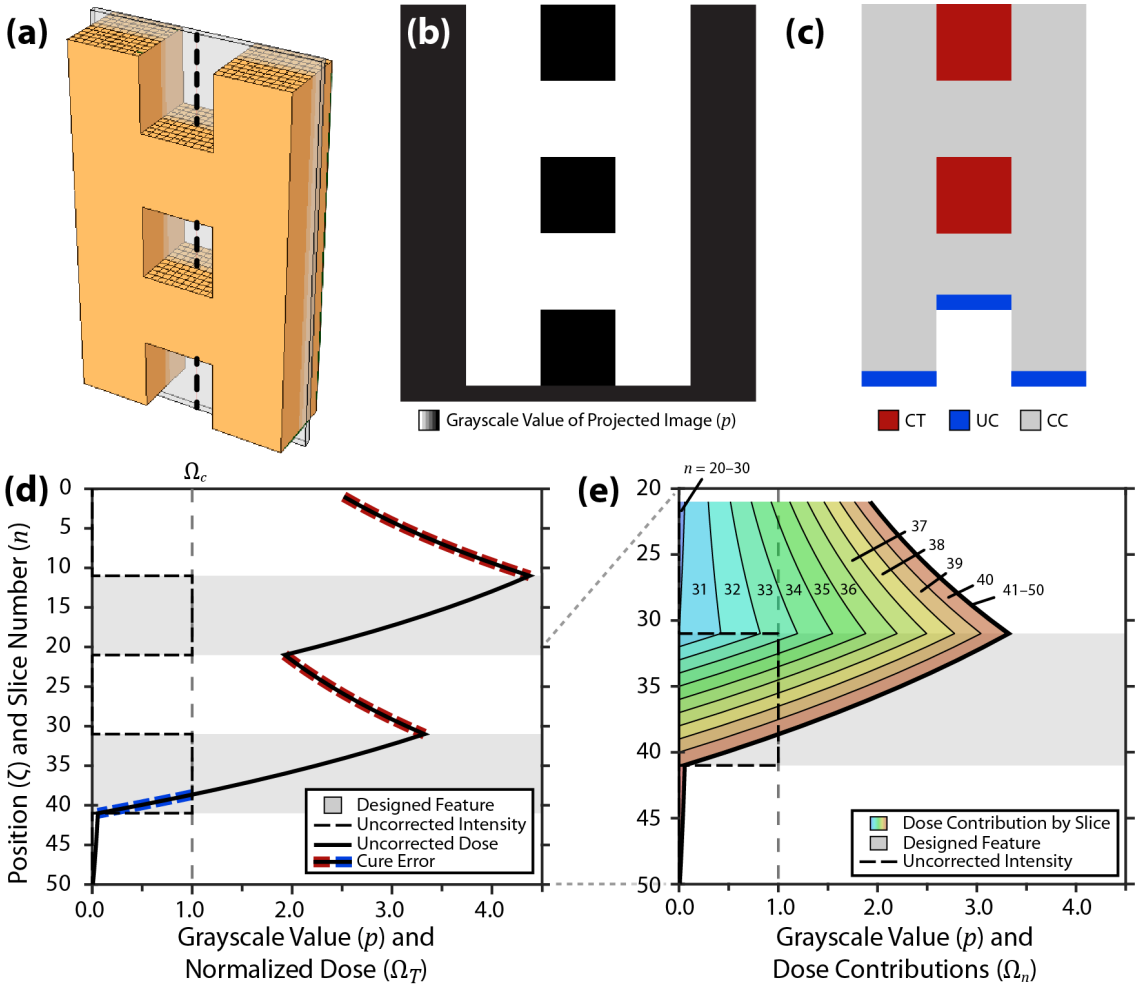

Figure 3.2: a) Test model. b) Vertical stack of uncorrected grayscale projections along the plane indicated in (a). Note that only black and white ($p = 0$ and $p = 1$) are used by default. c) Model prediction from slices in (b) showing areas with cure-through (CT, red) and undercuring (UC, blue). Gray regions of the part are correctly cured (CC). d) Grayscale value as a function of n and total accumulated dose as a function of ζ for the (x,y) position indicated by the dashed line in (a). $D_c = 50$ mJ cm^{-2}, $h_s = 50$ μm, $h_a = 2000$ μm, and $s = 1{,}000$ mm h^{-1}. $\zeta = 0$ corresponds to the top of the part (i.e., the surface attached to the build platform). The grayscale value p relates to the intensity of the projected pixel when $\zeta_w = n$ (calibration curve available in Fig. 3.6). Shaded areas indicate designed features. The dose curve indicates the normalized total dose Ω_T at position ζ on completion of the print, with cure errors indicated in red (cure-through) or blue (undercure). (e) Evolution of the total dose curve shown in (d) for $n = 21$ to $= 50$. The total dose is the sum of contributions from individual slices, each labeled and represented by a color.

Figure 3.2 shows modeled results for a ladder-like digital twin of a part printed using the default slicing approach, in which the maximum intensity is projected whenever an intended feature is adjacent to the window. There is significant cure-through into the gaps, and the bottom of the second feature is undercured. Rather than producing the desired two features, the conventional approach yields a single, large feature.

The total dose profile shown in Figure 3.2(d) is the result of contributions from all slices projected, as expressed in Equation 3.4. A closer look at the bottom feature highlights the causes of cure-through and undercure: Figure 3.2(e) shows the contribution of each slice to the total dose for this feature and, thus, the evolution of the dose curve during the continuous printing process. The uncorrected slices use only the maximum and minimum projector intensities ($p = 1$ and $p = 0$, respectively). While the maximum intensity is projected ($n = 31$ to 40), the accumulated dose rapidly increases for all $\zeta \leq n$. The nonzero minimum intensity results from light scatter in the projection system and is related to the projector contrast ratio (see Appendix B.2). Dose contributions while the minimum intensity is projected ($n = 21$ to 30 and $n = 41$ to 50) are relatively small. In the gap from $\zeta = 21$ to 30, the small contributions from minimum-intensity slices are overwhelmed by the contributions from maximum-intensity slices, resulting in cure-through. The feature is correctly cured from $\zeta = 31$ to ~ 38 then undercured through its designed bottom edge at $\zeta = 41$, highlighting that a point must be exposed over several slices to fully cure—even when projecting the maximum intensity. Finally, the gap below the feature correctly remains uncured. From this simple example, it is apparent that cure-through and undercure are inevitable when using unmodified slices with low-absorbance resins. This analysis also suggests that carefully designed slice images

could achieve the desired geometry.

The primary requirement for correcting cure-through and undercure is that the full height of each feature is cured without gelling non-features. However, as has been recently discussed with respect to tomographic printing, it is not possible to deliver exactly the critical dose within features and exactly zero dose outside features: to do so requires the ability to effectively "subtract" dose using negative intensities.[11] Clearly, not all dose profiles are achievable. Physically attainable dose profiles must be continuous and are limited by resin properties and printing parameters. These considerations define a set of three constraints, illustrated in Figure 3.3 and derived in Appendix B.3:

i. For all points within a feature, $\Omega_T \geq 1$; for all other points, $\Omega_T < 1$. Since Ω_T varies continuously with ζ, features will only be reproduced accurately if $\Omega_T = 1$ along edges.

ii. The maximum projector intensity, print speed, and resin absorbance height determine the maximum rate at which the dose can increase. With $\Omega_T = 1$ fixed at the bottom edge of the feature, these parameters define a maximum dose within the feature and a minimum dose below the feature.

iii. From Equation 3.4, the minimum dose at point ζ is limited by the minimum projector intensity, the print speed, the resin absorbance height, and the dose at point $\zeta + 1$. With the dose at the top edge set at the critical dose, these parameters define a maximum dose within the feature and a minimum dose above the feature.

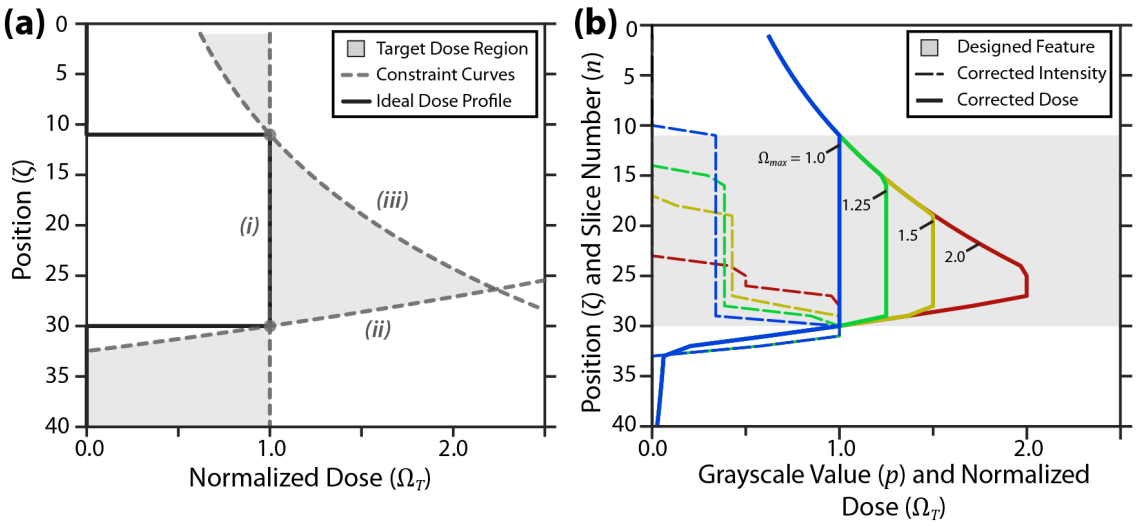

Figure 3.3: a) Three constraints which define the target dose region (shaded): *(i)* curing of features while non-features remain uncured, *(ii)* exposure at the maximum dose at the bottom of the feature, and *(iii)* exposure at the minimum dose at the top of the feature. b) Valid dose profiles defined by maximum dose $\Omega_{\max}$ with corresponding intensity profiles. Here, shading indicates the designed feature height. For a given set of parameters, the intensity profile can be tailored to achieve either a uniform dose or a high peak dose within features while still eliminating cure errors.

If any of these constraints are violated, the feature's edges will shift from their designed positions. The three constraints define *target dose regions*, indicated by shading in Figure 3.3(a). These regions are demonstrated here for a particular feature, but they can be generated for any feature height by shifting curves (ii) and (iii) along the ζ-axis such that the edges of the feature remain at the critical dose. Since the doses at adjacent points are interrelated, it is not possible to generate arbitrary dose profiles within the regions. However, there are an infinite number of achievable profiles which fall entirely within the target dose regions and thus produce an accurate part.

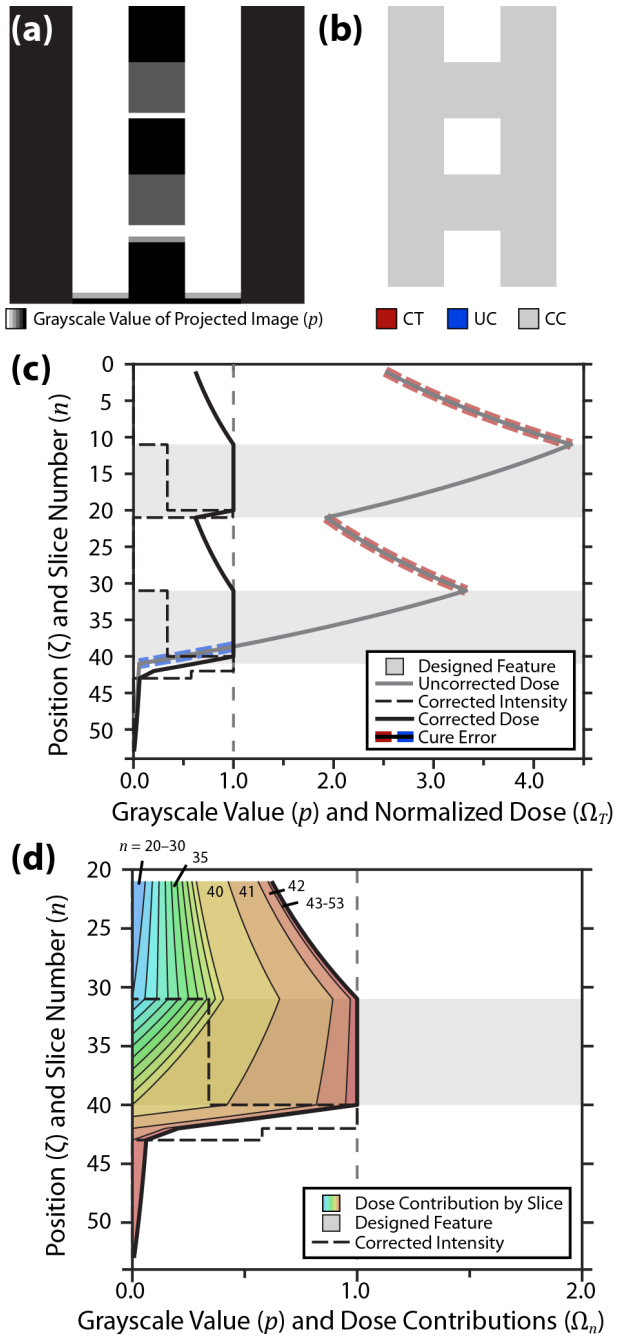

Figure 3.4: Correction for model in Figure 3.2(a) with $\Omega_{\max} = 1$. a) Vertical stack of corrected grayscale projections along the plane indicated in Figure 3.2(a). b) Model prediction from slices in (a) showing no cure-through (CT, red) or undercure (UC, blue). The full part is correctly cured (CC, gray). (c) Corrected grayscale value and dose for the (x, y) position indicated by the dashed line in Figure 3.2(a). Note that the correction process required additional slices beyond the original 50 to ensure the bottom of the part was fully cured. $D_c = 50$ mJ cm^{-2}, $h_s = 50$ μm, $h_a = 2,000$ μm, and $s = 1,000$ mm h^{-1}. (d) Contributions of individual slices to the accumulated dose curve shown in (c) for $n = 21$ to $n = 53$.

For the important case of $\Omega_{max} = 1$, the critical dose is uniformly delivered throughout the feature. We applied this correction to the model in Figure 3.2(a), with results illustrated in Figure 3.4. A comparison of Figure 3.4(a) and 3.2(b) shows how the correction process modifies slices. For the rung-like inner features, the intensity is reduced through most of the feature and a high-intensity burst is delivered at the bottom. Since there is no possibility of cure-through for the outer features, they are exposed at the maximum intensity. Figure 3.4(b) indicates that the correction has completely eliminated cure-through and undercure in our modeled result. Figure 3.4(c–d) show how the corrected slices achieve the desired dose profile. The high intensity burst at the bottom of the feature ensures all layers reach the critical dose. From the bottom-up perspective of the correction calculations, a constant intensity maintains the dose from one layer to the next after the critical dose is achieved at the bottom of the feature. From Equation 3.5, the intensity required to maintain a dose between two layers is $\Phi_n = \Omega_T$. Thus, to maintain the critical dose $\Phi_n = \Omega_c = 1$.

To achieve higher maximum doses, features must be exposed at higher intensities for shorter periods, as shown in Figure 3.3(b); a smaller fraction of the feature is exposed so that constraint (iii) is not violated. Though the edges of the feature are at the critical dose for each intensity profile, the interior dose varies considerably. As a result, it is important to optimize $\Omega_{max} = 1$ as well as D_c to ensure good part quality: high doses drive additional cross-linking, improving the part's green strength (i.e., its tensile strength before post-processing) to ensure a rigid and printable structure but also introducing heterogeneous internal stresses that can deform the part. Conversely, low maximum doses with long exposure times might not sufficiently cure the part since flow is not perfectly uniaxial and the resin bath is not infinitely deep. The optimal correction parameters depend in some degree on the irradiation system,

the geometry of the part, the flow profile in the resin bath, and the chemical and mechanical properties of the resin.

3.2.2 Experimental Validation

To test the correction algorithm and optimize its parameters, low-absorbance photopolymer resins were prepared (Table 3.1) for use with a previously-described two-color continuous stereolithographic 3D printer.[20] Experimental results are shown in Figure 3.5. The absorbance height h_a and gelation dose D_{gel} were determined from the resin working curves Figure 3.5(a)), and the test geometry in Figure 3.5(b) was used to investigate the effect of the critical dose parameter on print fidelity. We printed test parts using several values of D_c and an unconstrained maximum dose ($\Omega_{max} = \infty$), with results shown in Figure 3.5(b–d). Supplying exactly the measured gelation dose (i.e., $D_c = D_{gel}$) results in missing features and poor fidelity; feature sizes increase as D_c increases, and at higher values of D_c cure-through is observed (Figure 3.5(c)). As discussed above, a critical dose higher than the gelation dose is likely required due to the simplifying assumptions used in the correction algorithm and the need for a part of sufficient green strength. For the geometry, resin, and print conditions considered, $D_c = 5D_{gel} = 65$ mJ cm^{-2} is the optimal critical dose, achieving a marked improvement in fidelity without reducing print speed (see Figure 3.5(b)). Additional optimization details are available in Appendix B.4.

To further improve fidelity, the traditional approach of adding dyes or pigments to reduce light propagation can be used in conjunction with slice correction (Figure 3.5(e)). As previously reported, the addition of dyes necessitates slower print speeds.[8, 73] Regardless, applying slice correction at any dye loading or print speed improves the resolution, with higher dye loadings enabling printing of small features with less cure-through.

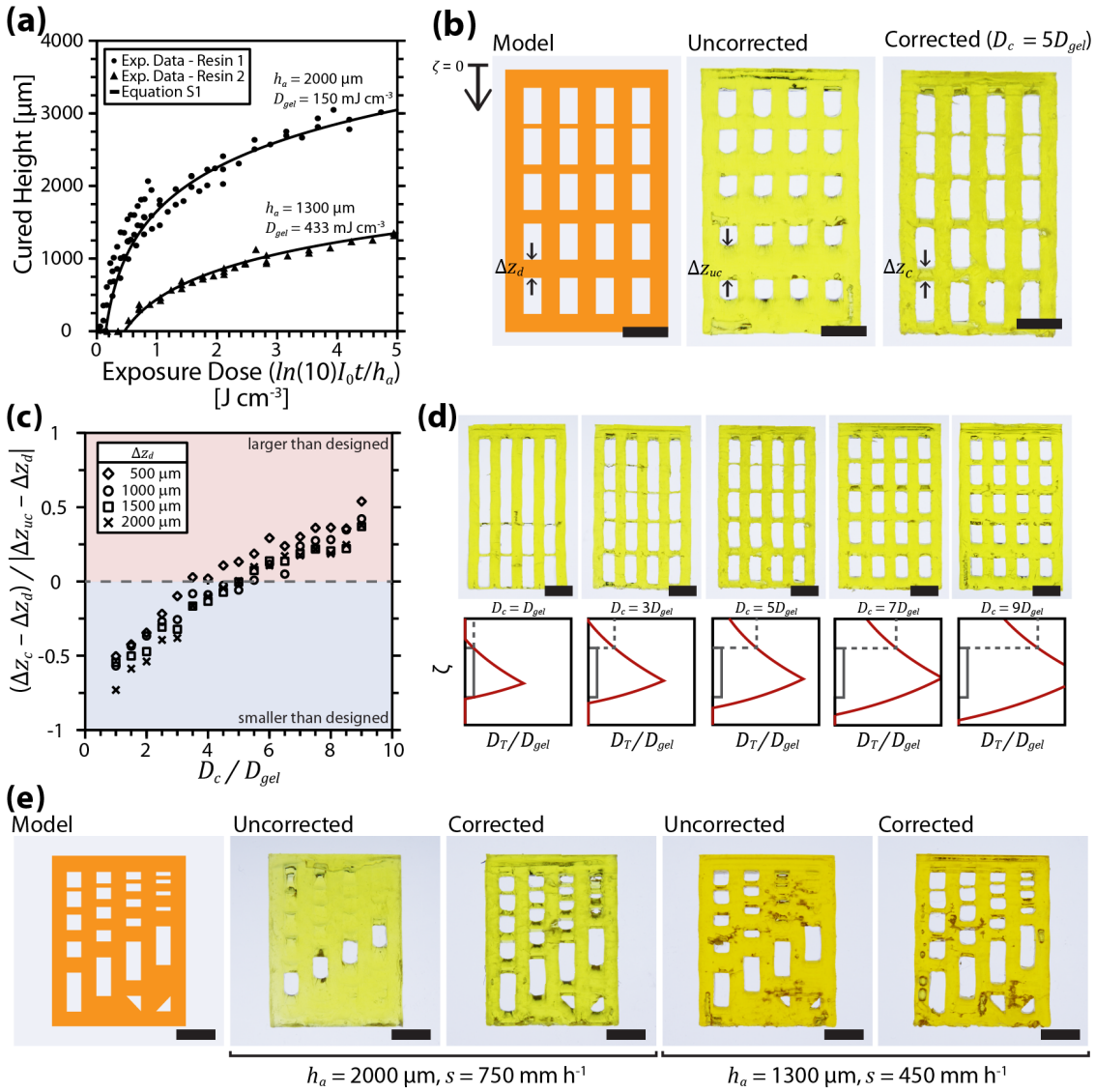

Figure 3.5: a) Cured thickness versus exposure dose of blue light for two acrylate-based resins (see Table 3.1) with differing concentrations of blue light absorber. b) Test model (left), uncorrected test part (center), and corrected test part printed with $D_c = 5D_{gel} = 65$ mJ cm^{-2} (right). Parts printed in Resin 1 at 750 mm h^{-1}. (c) Ratio of height errors (corrected-to-uncorrected) for a range of feature sizes and values of D_c. A ratio of zero corresponds to a perfectly corrected feature. d) Parts printed at 750 mm hh^{-1} using slices corrected with different values for D_c. e) Corrected and uncorrected test parts for two resins with different absorber loadings (i.e., h_a) and print speeds. All scale bars are 10 mm.

3.3 Conclusion

In summary, we have demonstrated a method for improving print fidelity on a two-color continuous stereolithographic 3D printer using resins with moderate to high absorbance heights. The approach analyzes and modifies the slice images for a model, using grayscale to precisely tune the dose profile throughout the final printed part. Though not demonstrated here, this technique is applicable to other continuous stereolithographic technologies such as CLIP and, with minor adjustments, to non-continuous stereolithography. Furthermore, this approach allows control over the dose delivered within features, enabling continuous 3D printing of parts with dose-dependent functionality.[86] Practically, this approach is limited by the resin green strength and the fluid dynamics of resin flow. Models that consider these effects or that vary critical dose with feature height might further improve fidelity. Nevertheless, this approach has afforded significant improvement in print quality for our system while maintaining high print speeds. Slice correction opens the door for the use of less-absorbing resins in stereolithographic systems, enabling faster print speeds and expanding the range of applications for additive manufacturing.

3.4 Materials and Methods

3.4.1 Modeling and Correction

Computational models and slice correction algorithms were implemented in MATLAB R2018b (MathWorks) and run on a desktop computer (Intel Xeon E5-1660 v4 @ 3.2 GHz, 32 GB RAM). Simulations and corrections completed within several minutes for all models.

Dose Modeling: Slice images are initially read into the program and stored as a three-dimensional array. The dimensions of this array correspond to the number of

slices and their dimensions in pixels. A typical slice image is 1,280 by 800 pixels and the number of slices is equal to the height of the designed part divided by the slicing height, h_s. In cases where the model does not utilize the full slice resolution (e.g., a 200-pixel-wide model in the center of a 1,280-pixel-wide image), the excess pixels outside the model volume are trimmed from the matrix to improve computational performance. The values in this matrix are grayscale pixel values (p) ranging from zero to one and correspond to the light intensities that will be projected at each pixel during each slice; zero and one represent the minimum and maximum blue-light intensities, respectively. The relationship between pixel value and light intensity is not linear, and pixel values are converted into intensities using a calibration curve (Figure 3.6) generated with a radiometer (International Light IL1400A).

Dose calculation begins at the bottom of the part, where the final slice is projected, and proceeds upward. The top cross-section of the part is exposed to every slice and each successive layer is exposed to fewer and fewer slices. By starting at the bottom of the part, we consider the cross-sections of the part exposed only to the final slice, then those exposed to the final two slices, then those exposed to the final three slices, and so on. As shown in Equation 3.5 and Table B.1, the total dose at ζ is the sum of the dose contribution from slice $n = \zeta$ and the total dose at $\zeta + 1$ multiplied by a factor of $10^{-\eta}$.

Slice Correction: The unedited images from the slicing software are taken to represent the "true" model and are converted into matrix form as above. Each feature within the part is identified. As with dose modeling, slice correction begins at the bottom of the part and works upward. Pixel values at the backside of the feature are set to reach D_c as quickly as possible (i.e., using the maximum intensity), and pixel values inside the feature are set to match a desired internal dose profile

using Equation 3.5. All pixel values are assumed to be zero (minimum intensity) unless specifically set otherwise. Finally, the matrix of corrected pixel values is converted back to a series of image files to be sent to the 3D printer.

3.4.2 3D Printing

Part Design: Test parts were designed in DesignSpark Mechanical 2.0 (SpaceClaim Corp.) and exported as STL files. Models were sliced using Autodesk Netfabb Standard 2018 (Autodesk) with default settings for the Ember 3D Printer (Autodesk) and 10 μm slice height. Slices from Netfabb are used with the MATLAB code to model final printed parts and produce corrected slices.

3D Printer: We printed test parts on a previously-described dual-color continuous stereolithographic 3D printer.[20] The DLP LED projector (Optoma ML750) was modified by removing power to the green and red LEDs and powering the blue LED by an external 0-5A LED driver circuit controlled by a custom LabVIEW virtual instrument.

Resin Formulations: Polymer resin was formulated as a mixture of oligomer, reactive diluent, photoinitiators, photoinhibitor, and light absorbers. For this work, the oligomer Sartomer CN991 (Sartomer) was used with 1,6-hexanediol diacrylate (HDDA, TCI America) as a reactive diluent. (±)-Camphorquinone (CQ, Esstech) was used as a blue-light photoinitiator and ethyl-4-dimethylaminobenzoate (EDAB, Esstech) was used as a co-initiator. 2,2'-Bis(2-chlorophenyl)-4,4',5,5'-tetraphenyl-1,2'-biimidazole (*o*-Cl-HABI, TCI America) was used as a UV-activated photoinhibitor. Epolight 5675 (Epolin) was used as the blue light absorber and Tinuvin 328 (BASF) was used as the UV absorber. Commercial blue epoxy pigment (Makerjuice Labs) was also used as a light absorber. The compositions of resins used are given in Table 3.1.

Table 3.1: Resin Formulations

Component	Function	Concentration (wt.%)		
		Resin 1	Resin 2	Resin 3
o-Cl HABI	Photoinhibitor	2.8	2.8	2.8
Camphorquinone	Photoinitiator	1.9	1.9	1.9
EDAB	Co-initiator	0.95	0.95	0.95
Tinuvin 328	UV absorber	0.47	0.47	0.47
Epolight 5675	Blue light absorber	0.001	0.003	-
CN991	Oligomer	56.3	56.3	56.3
HDDA	Reactive diluent	56.3	56.3	56.3
Blue pigment	lightabsorber	-	-	0.002

3.4.3 Measurement of $D_{\mathbf{gel}}$ and $h_{\mathbf{a}}$

The two resin properties required for input into the correction algorithm are the absorbance height ha and the gelation dose Dgel. These properties are fitted using the least-squares method with a cured height vs. dose working curve similar to that developed by Jacobs[[87]]:

$$z_{\mathrm{ct}} = h_{\mathrm{a}} \log\left(\frac{I_0 t}{D_{\mathrm{gel}}}\right) \tag{3.6}$$

Liquid photopolymer is cured into plugs by exposing to curing light of intensity I_0 for varying lengths of time t. The height of the cured plug is measured using a digital micrometer with an accuracy of 10 mum. Light intensities used in these experiments were measured using an International Light IL1400A radiometer with a GaAsP detector (model SEL005), a 10x attenuation neutral density filter (model QNDS1), and a quartz diffuser (model W).

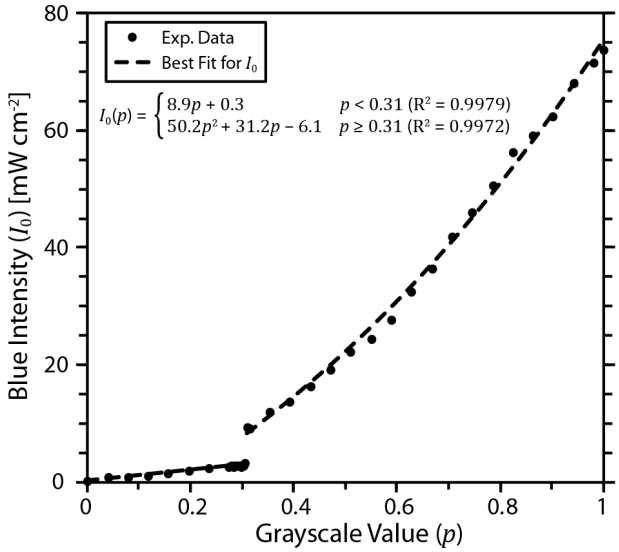

Figure 3.6: Measured blue intensity, I_0, as a function of the grayscale value, p, of the displayed image. The calibration curve is found to be a piece-wise function typical of manufacturer color balancing encoded into projector firmware.

CHAPTER IV

Dual-Wavelength Fabrication of Multilayered Microfluidic Devices

4.1 Introduction

Microfluidic devices, with length scales typically on the order of tens to hundreds of micrometers, offer researchers predictable, precise fluid flow while utilising small reagent quantities. As such, applications of microfluidics in analytical chemistry[88], cell-based assays[89], and molecular biology[90] are widespread. The most ubiquitous fabrication technique for microfluidic devices is replica molding by *soft lithography*[12]. The most widely used embodiment of this technique creates channels by curing polydimethylsiloxane (PDMS), an elastomeric polymer, over a microfabricated SU-8 master[13]. The number of steps involved in PDMS soft lithography make this process unsuited for rapid production or prototyping of microfluidic devices. Furthermore, adjustment of device design is impossible without fabrication of a new master and multilayered PDMS devices[91, 92, 93] require one iteration of this process for each individual layer (and additional steps to bond and interface between layers) - increasing the time, complexity, and graduate student frustration of fabricating complex devices. Additive manufacturing (or 3D printing) of microfluidic devices is attractive due to the short design-to-device times and ability to fabricate complex three-dimensional structures with little to no additional effort[15, 16].

Fused deposition modelling (FDM) and stereolithographic (SL) additive manufacturing are the most common 3D printing methods, and have demonstrated applications in device[17, 18, 19, 20, 21] and mold fabrication[22, 24, 23]. SLA uses patterned light to cure layers of material from a liquid photopolymer resin bath. Typical commercial SLA printers use near-UV polymerizing light and can fabricate enclosed channels of 200-300 μm[25, 20] although custom SLA setups with optimised resin formulations are able to achieve much smaller features[26] and enclosed channels[27]. Continuous SLA additive manufacturing is a recently reported method significantly improved the production speed of additive manufacturing, while eliminating the directional non-uniformity of material properties[8]. Continuous printing is enabled through the creation of a *'dead zone'* (a constant liquid layer of resin chemically inhibited from polymerizing) by incorporating an oxygen permeable projection window[8] or light-activated photo-inhibition chemistry in a dual-wavelength system[73].

We recently reported dual-wavelength continuous additive manufacturing uses two orthogonal radical generating reactions active at different wavelengths on the electromagnetic spectrum. In this system camphorquinone (CQ, Fig.4.1(a)) and ethyl 4-(dimethylamino) benzoate (EDAB, Fig.4.1(b)) readily generate initiating radicals under visible light irradiation whereas *o*-Cl-HABI (2,2'-Bis(2-chlorophenyl)-4,4',5,5'-tetraphenyl-1,2'-biimidazole, Fig.4.1(c)) when irradiated with ultraviolet (UV) light generates stable, non-reactive radicals. These radicals have been demonstrated to inhibit curing in a wide range of (meth)acryate resins by recombining with propagating carbon-centered radicals during polymerization. Concurrent irradiation of visible and UV light into a vat of photopolymer (formulated with CQ,EDAB, and *o*-Cl-HABI), results in a photo-inhibited dead zone above the incident surface. The thickness of this dead zone is dependent on the resin properties and, more impor-

tantly, the intensity of the incident visible and ultraviolet light. Grayscale exposures from digital light projection (DLP) systems are able to spatially vary intensity in a single exposure and hence control the thickness of the dead zones. Here we report the development of a single-step stereolithographic method for fabrication of multi-layered microfluidic devices using this dual-wavelength system.

4.2 Materials and Methods

4.2.1 Exposure Setup

A custom dual-wavelength exposure setup was created by modification of the software of a previously-described two-color 3D printing setup [CITATION]. 365 nm ultraviolet light from a 1400 mA UV light emitting diode (Thorlabs, M365LP1) is collimated with an adjustable collimation adapter (Thorlabs, SM2F) and an aspheric condenser lens (Thorlabs, ACL50832U) and superimposed over 455 nm blue light from a commercial 700 Lumen DLP projector (Optoma ML750) using a longpass dichroic mirror (Thorlabs, DMLP425L). The red and green channels of the DLP projector were removed. The blue projector and UV LEDs are independently controlled by a 0-5V analog signals from a custom Labview VI to external LED driver circuits. The intensity at the imaging plane was calibrated for input analog voltage and image greyscale value using a digital radiometer (International Light Technologies, ILT2400) with a UV-Vis GaAsP detector (International Light Technologies, SED005/U) and a 10x attenuation filter (International Light Technologies, QNDS2).

4.2.2 Materials

DL-Camphorquinone (CQ, Fisher Scientific) and ethyl 4-(dimethylamino)benzoate (EDAB, ACROS Organics) are used a visbile light initiator and co-initiator respectively, 2,2'-Bis(2-chlorophenyl)-4,4',5,5'-tetraphenyl-

1,2'-biimidazole (*o*-Cl-HABI, Hampford Research Inc) was used a ultraviolet photoinhibitor. A proprietary aliphatic polyester-based urethane diacrylate (CN991, Sartomer Americas) was used as the oligomer and 1,6-hexanediol diacrylate (HDDA, TCI America) was used as the reactive diluent and 3-(trimethoxysilyl)propyl methacrylate (TMSPM, Sigma-Aldrich) was added to improve adhesion to the glass substrate. Resins were prepared by dissolving 1/0.5/2.5 wt.% CQ/EDAB/*o*-Cl-HABI in tetrahydrofuran (THF, 99+%, ACROS Organics) by dropwise addition of THF until clear, and mixing with 1/40/55 wt.% TMSPM/CN991/HDDA, solvent was evaporated off under flowing air. Two-part polydimethylsiloxane elastomer (PDMS, Sylgard 184, Dow Corning) or 3D printing was used to fabricate spacers (see below). Isopropanol (IPA, laboratory grade, Fisher-Scientific) was used as a solvent to remove uncured material in gelation height experiments and to flush uncured material from channels. Standard food coloring was used to color deionized water to improve visibility of channels within the cured material. All materials were used as received and all polymerizations were conducted at room temperature.

4.2.3 UV-Vis Spectroscopy

UV-visible spectrophotometry was performed on all resin components to determine their mass absorptivity at 365 and 460 nm using a Shimadzu Spectrophotometer (UV 1900i). Spectra were collected from 300 to 600 nm with 0.5 nm spacing using a 1 cm path length polystyrene cuvette. THF was used as a reference as well as a diluent to vary the concentration of samples.

4.2.4 Resin Curing Tests

A series of images of a 5x5 grid of different exposure times was generated by slicing of an appropriately designed solid. The grayscale of the images (and hence

the intensity of the projections) was quickly varied using a Matlab script. A 5 mm well for liquid resin was 3D printed and affixed to a 2×3" glass slide using standard two part epoxy adhesive. The well was filled with resin and blue light was projected into the resin using the aforementioned images for different times ranging from 0.1 to 25 s. Uncured liquid resin was rinsed from the gelled material using IPA and the gelled material was further cured under a white light for 5 minutes. The height of the gelled material is then measured with a dial caliper (Starrett, USA) with a resolution of 12.5 μm.

4.2.5 Dead Zone Measurements

Liquid resin was sandwiched between two 2×3" glass slides spaced 800 μm apart using plastic shims. The resin is then exposed for 15 s to images with different grayscale blue intensities and a constant UV intensity of ≈50 mW/cm^2. The resulting gelled material is rinsed with IPA, dried at 60 ∘C for 30 min and measured with a micrometer with an accuracy of 1 μm. The dead zone height is calculated by subtraction using the formula: $z_{\mathrm{dz}} = z_{\mathrm{sp}} - z_{\mathrm{gel}}$, where z_{dz}, z_{sp}, and z_{gel} are the dead zone, spacer, and gelled material heights respectively.

4.2.6 Microfluidic Device Fabrication and operation

Liquid resin was sandwiched between two 2×3" glass slides spaced 2000 μm with PDMS spacers. The PDMS spacers were prepared by the two part PDMS kit in a 10:1 monomer:crosslinker ratio, degassing and curing at 60 °C for 2 hours in between two 1/2 in. polycarbonate sheets spaced 2 mm apart with two 1 mm thick glass slides. The top glass slide has holes drilled for use as inlet and outlet ports. For drilling, the slides were reversibly bonded to a backing wafer using Crystalbond 555 (Ted Pella) heated to 70°C. Drilling layouts were prepared in Autodesk Fusion 360

and exported as gcode to a CNC mill (Tormach PCNC). A peck-drilling operation with a 750 μm diamond micro drill (Amplex S-Series .030") was used with a drill speed of 10 000 RPM, peck height of 100 μm and feed rate of 5 mm/min. The glass-resin-glass sandwich is placed at the focal plane of the projector and exposed to grayscale images of the microfluidic device for a given amount of time. The devices are designed on Adobe Illustrator and exported as 1280×800 .png images. The exposure time and grayscale value required to give a particular channel height are given by equations 4.3 & 4.4 and the calibration curves in Appendix C.1. After exposure, the uncured resin is flushed from the channel with IPA by connecting tubing to the drilled inlet and outlet using a magnetic microfluidic adapter (Cor-Solutions microfluidic connectors BMP-LP-2X) and pneumatic pressure applied by hand. Once the channels were flushed the device is fully cured under a white LED lamp for 5 minutes. For other microfluidic experiments PTFE electrical-insulating sleeve washers (McMaster-Carr) were bonded to the channel inlets and outlets using UV-curable optical adhesive (Norland) to enable porting with 90 deg luer-lock syringe tips.

4.3 Results and Discussion

4.3.1 Initiation / Inhibition Model Development

Camphorquinone (CQ, Fig.4.1(a)), ethyl 4-(dimethylamino) benzoate (EDAB, Fig.4.1(b)) and *o*-Cl-HABI (2,2'-Bis(2-chlorophenyl)-4,4',5,5'-tetraphenyl-1,2'-biimidazole, Fig.4.1(c)) enables polymerization initiation with visible light irradiation and inhibition with UV (or combined) visible and UV irradiation. Initiation and inhibition are controllable with two independent wavelengths (here we use $\lambda_{\text{init}} = 463$ nm and $\lambda_{\text{inhib}} = 365$ nm) due, not only to favourable chemistry[94, 73], but also to complementary absorbance spectra (Fig.4.1(d)). *o*-Cl-HABI absorbs

strongly <400 nm and, fortuitously, CQ/EDAB has a region of exceptionally low absorbance from 350-375 nm while absorbing strongly from 450 - 500 nm allowing chemically orthogonal processes to be activated under irradiation with visible light and UV light.

We developed a does-based model to describe gelation under conditions of concurrent initiation and inhibition (See C.2). The model describes the distribution of delivered dose, D by blue and UV irradiation into a static resin sample.

$$D = \left(I_{\text{blue},0}e^{-z/h_{\text{blue}}} - \beta I_{\text{UV},0}e^{-z/h_{\text{UV}}}\right)^m t \tag{4.1}$$

where z is the height into the resin, $I_{0,\text{blue}}$ and $I_{\text{UV},0}$ are the incident intensities of the initiating and inhibiting lights, h_{blue} and h_{UV} are the absorbance heights at the initiating wavelength and inhibiting wavelengths, D_c is the curing dose, t is the exposure time, β is the *inhibition coefficient*, and m is a constant related to the molecularity of chain growth termination. h_{blue} is a commonly used notation in additive manufacturing literature and is defined as the inverse of the sum of the concentrations of all absorbing species (c_i) multiplied by their wavelength-specific molar absorptivity (ϵ_i) (i.e. $h_i = 1/\sum \epsilon_i c_i$). It is important to note ambiguity in the use of *decadic* (ϵ_{10}, base 10) and *Napierian* (ϵ_e, base e) molar absorptivities (and hence absorbance heights), these are used interchangeably in different disciplines (much to the frustration of investigators). This study will use exclusively the *Napierian* representation.

When the dose delivered is equal to the threshold dose required for gelation (i.e. $D = D_c$) we arrive at an equation for the gelled height, $z$gel, in a dual-wavelength system:

$$D_c = \left(I\text{blue},0e^{-z_{\text{gel}}/h\text{blue}} - \beta I\text{UV},0e^{-z_{\text{gel}}/h_{\text{UV}}}\right)^m t \tag{4.2}$$

Under exclusively initiating light (i.e., $I_{\text{UV},0} = 0$) Eq. 4.2 simplifies to an equation

for z_{gel} similar to the commonly used 'Jacobs' Curve':

$$z_{\text{gel}} = \frac{h_{\text{blue}}}{m} \ln\left(\frac{I_{\text{blue},0}^{m} t}{D_c}\right) \tag{4.3}$$

However, under co-irradiation it must be noted that Eq.4.2 has two positive roots (i.e. two values of z_{gel} which satisfy the equation) for all $I_{\text{UV},0} > I_{\text{blue},0}/\beta$. The physical significance of these roots are the two gelation interfaces present in a photoinhibited system. These interfaces are the positions of the incipient gelling material on the back and frontside of the gelled *plug* formed under irradiation. It is important to note that as t approaches ∞ the backside gelation height tends to infinity while the frontside tends to the previously reported[73], steady-state dead zone height (see Fig C.2) as calculated by:

$$z_{\text{dz}} = \frac{ln\frac{\beta I_{\text{UV}}}{I_{\text{blue}}}}{\frac{1}{h_{\text{UV}}} - \frac{1}{h_{\text{blue}}}} \tag{4.4}$$

Controlling these interfaces by controlling $I_{\text{blue},0}$, $I_{\text{UV},0}$, and exposure time, t, when exposing a confined region of resin allows us to pattern uncured regions on the front and back of the resin which, when flushed, can be used as microfluidic channels.

4.3.2 Conditions for Microfluidic Channel Fabrication

Fabrication of microfluidic channels using this method relies on two phenomena: the progression of gelled polymer due to initiating irradiation to create backside channels, and photo-inhibition to create frontside channels. Volumetrically confining resin between glass slides, spaced z_{sp} apart, enables a multiple permutations of gelled material, and hence, channel configurations. In a single exposure there are seven configurations. The configuration achieved upon irradiation depends on the incident initiating and inhibiting doses ($D_{\text{i},0} = I_{\text{i},0}^{m} t$) delivered as shown graphically in Fig. 4.2. The dose can be varied by either varying the exposure intensity or the exposure time. The decision on which to vary is dependent on the configuration of the optical

setup. If UV light can be patterned, it is preferable to vary the intensity maintaining a constant exposure time. However, if UV cannot be patterned (as is the case in our system shown in Fig. 4.2(b)) the same effect can be achieved with multiple exposures of varying times. In this system, the channel height for the frontside is equal to the dead zone height (i.e. $z_{c,fs} = z_{dz}$) and the channel height for the backside is the difference between the spacer height and the gelled height from Eq. 4.3 (i.e. $z_{c,bs} = z_{sp} - z_{gel}$).

4.3.3 Resin Initiation and Inhibition Characterization

We prepared photo-polymerizable resin to demonstrate the applicability of photo-inhibition in microfluidic device fabrication. The identity, concentration and function of the different resin components is summarized in Table 4.1.

As previously mentioned CQ/EDAB + *o*-Cl-HABI is applicable to a wide range of (meth)acrylate monomers. That being said, monomer choice is not arbitrary and properties such as viscosity, reactivity, 'inhibitability' and optical transparency must be carefully considered when choosing a monomer. The viscosity of CN991 (660 cP @ 60 °C) makes working with it difficult, necessitating the addition of reactive diluent to decrease the viscosity. 1,6-hexanediol diacrylate (HDDA) is added to reduce the viscosity. HDDA was found to be particularly susceptible to photo-inhibition with *o*-Cl-HABI ($\beta \approx 25$) while having high reactivity (as evidenced by relatively low D_c)

Table 4.1: Resin components used in microfluidic device fabrication

Component	Function	Concentration (wt.%)
CQ	Visible photo-initiator	1
EDAB	Co-initiator	0.5
o-Cl-HABI	UV photoinhibitor	2.5
CN991	Oligomer	40
HDDA	Reactive diluent	55
TMSPM	Promote SiO_2 adhesion	1
Epolight 5675	Visible dye	0.01

when compared with other diluents tested (see Table C.1). Furthermore, polymerization shrinkage - a well known problem in (meth)acrylate photopolymerizations[95] - needs to be considered and was found to be particularly problematic in highly functionalized diluents (e.g. trimethylolpropane triacrylate (TMPTA)). Monomers typically don't have meaningful absorbance in the visible range, as is often desirable in a large variety of coating applications, but may have significant UV absorbance which effects h_{UV} and z_{dz}. The high optical transparency of CN991/HDDA in the UV and visible region, as seen by the low absorbances in Fig 4.1(b), are therefore desirable in this application.

To determine the reactivity, absorbance height, and intensity dependence of the resin we conducted gelled height experiments whereby photopolymer resin was irradiated with visible light ($\lambda_{\max} = 458$ nm) of various intensities ($I_{0,\mathrm{blue}} = [210, 144, 86, 44, 16]$ mW/cm^2) for different times and the gelled height measured. This experiment yields a cured height curve analogous to the *working curve* typically used in stereolithography[96, 87] which allows a 'calibration' for gelled height and intensity/exposure time as shown in Fig. **??**(a). An assumption in the conventional stereolithography working curve, however, is that of uniform intensity irradiation which is reasonable when considering the mechanism of conventional stereolithography but ill-suited to this method which spatially varies intensity using digital light projection (DLP). By fitting Eq. 4.3 to experimental data at different intensities, we obtain the resin parameters: $D_c = 240$ (mW/cm^{-2})^{m}s, $h_{\mathrm{blue}} = 1630$ μm, and $m = 1.02$. It is prudent to note that while it is possible to determine h_{blue} (and h_{UV}) from UV-Vis spectroscopy, the value obtained differs slightly to that from a gelation height experiment. This difference is most likely attributed to the broad emission spectrum of the LEDs used in gelation height experiments. Intensity varia-

tion (i.e. grayscale) in this system (as with all DLP projection systems) is achieved by pulse width modulation (PWM) of a digital micromirror device (DMD). While not strictly an 'intensity variation' any difference between grayscale modulation and a strict intensity variation were not observed in this system.

As previously mentioned co-irradiation of this resin with visible and UV light results in photo-inhibition and a dead zone at the incident surface of the resin bath. To determine the effect of UV light on this particular resin composition we experimentally calculated z_{dz} at different ratios of inhibiting to initiating intensities ($I_{\mathrm{UV},0}/I_{\mathrm{blue},0}$) as shown in Fig. 4.3(b) using a previously described method.[73, 8]. In these experiments, $I_{\mathrm{UV},0}/I_{\mathrm{blue},0}$ is varied by adjusting $I_{\mathrm{blue},0}$ through the grayscale value of the exposure image. Decreases in $I_{\mathrm{blue},0}$ result in higher $I_{\mathrm{UV},0}/I_{\mathrm{blue},0}$ and subsequently thicker dead zones due to the higher relative rate of inhibition to polymerization. Since these experiments are done on a relatively short time scale ($t = 15$ s), the experimental data is fitted to the unsteady-state model (Eq. 4.2 by varying h_{UV} and β. The values which minimized the objective function were found to be $h_{\mathrm{UV}} \approx 132$ μm and $\beta \approx 4.3$. An important aspect of the unsteady state model for a given exposure time there exists a cut-off $I_{\mathrm{UV},0}/I_{\mathrm{blue},0}$ ratio above which no polymer will cure, for this experiment this is shown with a dashed line in Fig. 4.3(b).

4.4 Fabrication of Microfluidic Channels

4.4.1 Minimum Channel Size

Microfluidic channels in this method are created by patterning gelation in a photopolymerizable resin confined between two glass slides. Once channels are patterned, the uncured liquid resin needs to be flushed from the channel in order to realize a usable channel. The ability to fabricate channels and successfully flush uncured resin is affected by a number of system variables such as channel dimensions, resin vis-

cosity, gelled green strength and glass adhesion strength. To evaluate which channel dimensions are achievable with our resin in our system, we fabricated a number of channels on the front- and backside of the confined resin. The channel width was varied by varying the pixel width in the image of the channel design. Widths from 650 to 3900 μm (which corresponded to a variation of 5 to 30 pixels, since 1 px $\approx$ 130 μm in our system). The exposure intensities (and hence channel heights) were varied by varying the grayscale value of the projected image. The channel heights for a given exposure are calculated from Eq. 4.3 and Eq. 4.4. Uncured resin was flushed from these channels and the channels were characterized based on the ability to flush uncured resin from them as shown in Fig. 4.4. From this experiment we found that channels with sub-millimeter heights are easily fabricated on the front- and backside of the resin, however as both the height and width of the channels decreased it became increasingly difficult to fabricate channels. The difficulty to fabricate narrow channels is most likely due to the optical setup, diffusion of light within the resin and resin viscosity effects. Improvements by varying these factors were not explored in this proof-of-concept study, smaller channels are certainly achievable with changes to these factors. One interesting aspect of the backside channels, however, is that it seems possible to create channels with 'negative' height (i.e., which are cured past the back surface) which still allowed flow to be forced through. This is due to the relatively shallow intensity decay (resulting from the high blue absorbance height in this resin) resulting in gelled material at the back gelation interface with insufficient material strength to resist fluid piercing through. This is not as pronounced in the frontside channels due to the much smaller absorbance height of UV. Decreasing h_{blue}, by the addition of blue absorbing dye or increasing the concentration of CQ will improve the properties of the partially gelled material at the gelation interface.

4.4.2 Multi-layer Microfluidic Channel Fabrication

To demonstrate the utility of this fabrication technique we designed two multi-height microfluidic devices. The first design we used to demonstrate this method is that of a three-dimensional mixer similar to the design developed by Liu *et al*[97] as shown in Fig. 4.5(a). This design has numerous serpentine 'C-shaped' mixing segments moving in and out any given horizonal plane and typically requires multiple lithography steps to fabricate. Realizable channel heights and widths are chosen based on 4.4, in this case, $z_{\mathrm{c,bs}} \approx 300$ μm, $x_{\mathrm{c,bs}} = 2000$ μm, $z_{\mathrm{c,fs}} \approx 200$ μm, and $x_{\mathrm{c,fs}} = 2500$. z_{sp} in these experiments was chosen to be 2000 μm. Since we do not have pixel-level control over the ultraviolet intensity, the backside and frontside channels need to be patterned with two separate exposures (shown in 4.5(b)). The first ten second exposure uses blue light only to gel the area around the channels and form the backside channels (leaving the area where frontside channels will be created empty). The second twenty second exposure uses simultaneous exposure of blue and UV to form the frontside channels. After exposure, the uncured resin is rinsed from around the device and flushed from the channel. Since the material is only partially cured at this point, care must be taken while flushing to not rupture the channels. A particular problem was 'tunneling' along the interface between material cured on the first and second exposure whereby IPA essentially splits the interface creating an undesigned and undesirable channel. This is most likely due to differing degrees of curing (and hence levels of polymerization shrinkage) causing a stress fracture at the interface. Use of resins commercial resins designed specifically for this purpose will certainly improve the performance of this system. Note that any commercial resins will need to be supplied without photo-initiators and CQ/EDAB and *o*-Cl-HABI added. That being said we were able to fabricate the desired three-

dimensional microfluidic channel (see Fig. 4.5(c)) with the current resin and setup. To illustrate the three-dimensionality of this channel we introduced a bubble into the flowing stream. The movement of the bubble into and out of the focal plane, as can be seen in Fig. 4.5(d) clearly indicates a three-dimensional structure. The second design incorporates two overlapping channels with cured material between them (see Fig. 4.6). This is a particularly useful structure in microfluidics, particularly with the objective of developing compact devices, and incorporating functional structures such as 'Quake' valves[98]. As previously mentioned the lack of controllable ultraviolet in this system necessitates multiple exposures, for this device three exposures are necessary (see Fig. 4.6(b)). Similar to the first example device, the first ten second exposure uses blue light only and to gel the material around the channels, and form the backside channels. The second 13 s blue and UV exposure, forms the frontside channels and the overlapping region between the two channels, and the third seven second UV and blue exposure completes the curing of the frontside channels. It needs to be stressed that the material present in the overlap is exceptionally fragile, and the channels are extremely difficult to flush without piercing this material. Nevertheless, with extreme care overlapping channels are able to be fabricated as shown in Fig. 4.6(c), with overlapping flows with no mixing between channels able to be achieved (Fig. 4.6(d)). To improve the yield of overlapping channels fabricated by this method, alternative methods for removing uncured resin (such as centrifugation) should be explored. Additionally, decreasing the resin absorbance height by the addition of photoinitiator or absorbing dyes will improve the material properties of the weakly gelled material.

4.5 Conclusions

In conclusion, we have developed a method to fabricate three dimensional microfluidic devices using a dual-wavelength initiation and inhibition system. This method fabricates polymeric devices in place between glass slides in less than a minute using exposures from a simple two-color optical setup. Multilayer devices are easily designed using simple design software (e.g. Adobe Illustrator, MS Paint, etc.) and fabricated within seconds. This represents a significant advance in functionality over traditional lithography-based fabrication techniques which may lower the barrier-to-entry of microfluidics for a wide cross-section of users. Furthermore, the use of elastomeric resins with this method may enable fabrication of highly functional multilayer devices at unprecedented speed.

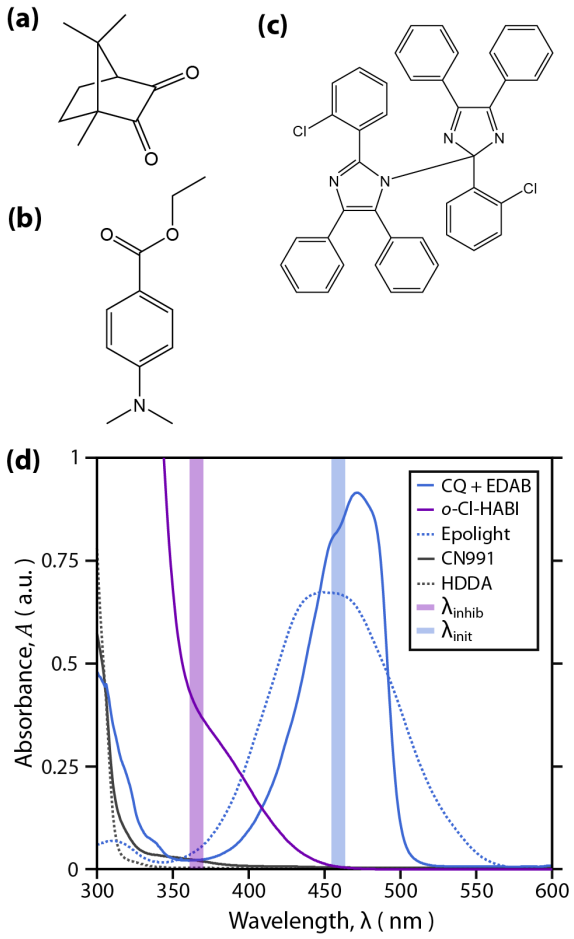

Figure 4.1: Structures and absorbance spectra of resin components. Structure of (a) photoinitiator (CQ), (b) co-initiator (EDAB), (c) photoinitiator (*o*-Cl-HABI, and (d) diluent (HDDA), the chemical structures of CN991 and Epolight 5675 are proprietary and not known. (e) Absorbance spectra of resin components diluted in tetrahydrofuran (THF) to concentrations, in wt.%, of 25, 6, 0.4, 0.06, and 2.3×10^{-4} for HDDA, CN991, CQ+EDAB, *o*-Cl-HABI, and Epolight 5675 respectively. The emission wavelength of the inhibition and initiating light sources used in experiments are shown in with shaded blue and purple boxes.

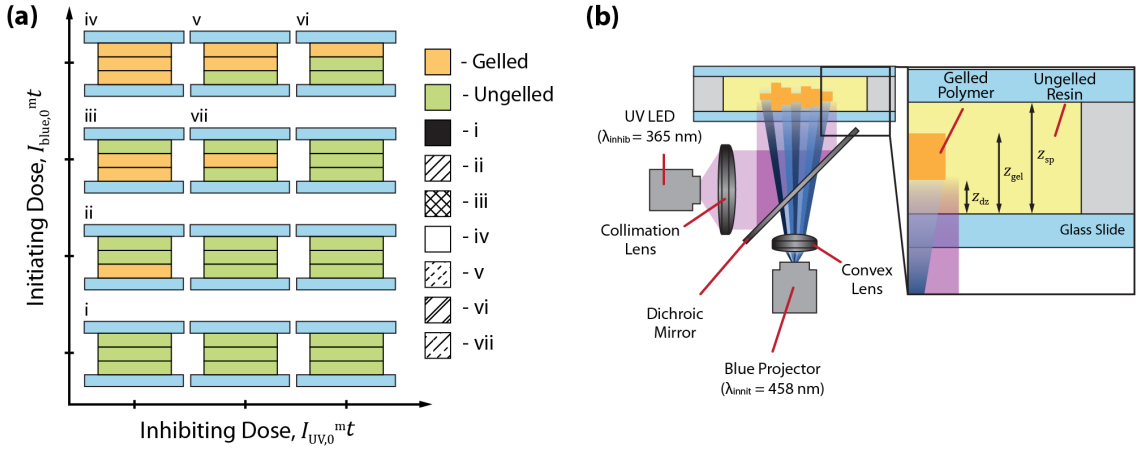

Figure 4.2: Microchannel fabrication with dual-wavelength irradiation. (a) Qualitative representation of the possible gelation permutations achievable with different relative initiating and inhibiting doses, with . Note the different hatches for these cases will be consistent throughout this paper.(b) Schematic of

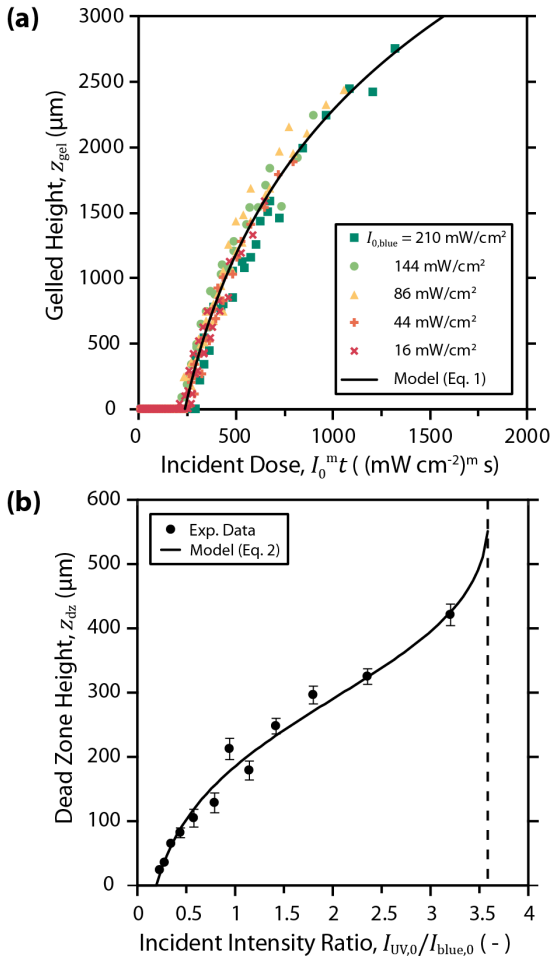

Figure 4.3: Optical Setup and Initiation and Inhibition of Resin. (a) Schematic of setup used in curing height, dead zone, and microfluidic device fabrication experiments. Note that the initiating wavelength is patterned by a DLP projector, whereas the UV is unpatterned. (b) Gelled height vs. Incident dose for the resin described in Table **??**, cured at intensities shown for times ranging from 0.1 to 50 s. Values for m, D_c and h_{blue} of 0.95, 230 (mJ/cm^2)^m, 1275 μm respectively are found by least squares fitting Eq. 4.1 and (c) Dead zone height vs. Incident intensity ratio for the same resin for 15 s exposures, the incident intensity ratio is varied by varying the grayscale value of the initiating light. Values for β, and h_{UV} of 4.3 and 125 μm are found by least squares fitting Eq. 4.2. The dashed line denotes the maximum intensity ratio at which material will gel.

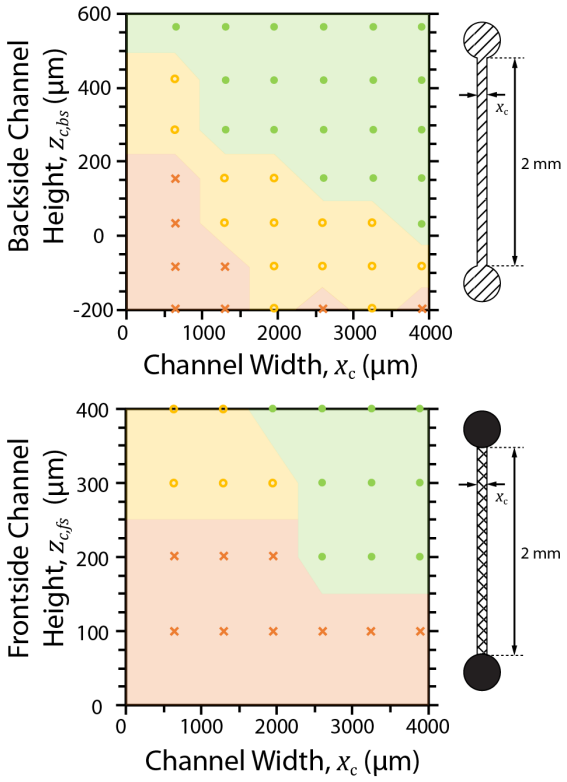

Figure 4.4: Determination of Minimum Channel Dimension. Channels dimensions which are cleanly flushed with IPA and hand pressure are denoted with solid green circles, poorly formed channels are shown with yellow circles, and channels which did not allow flow without rupturing are shown with red crosses. (a) Success of fabricating backside channels for channels of different widths and heights. Grayscale values for channels used in exposure were $p = [0.59, 0.63, 0.67, 0.71, 0.75, 0.78, 0.82]$ and all channels were exposed for 15s. (b) Success of fabricating backside channels for channels of different widths and heights. Grayscale values, chosen to give specific channel heights, used in experiments were $p = [0.98, 0.6, 0.4, 0.3]$ with exposure times of $t = [10, 20, 30, 60]$ s respectively and $I_{\mathrm{UV},0} = 100\mathrm{mW/cm}^2$.

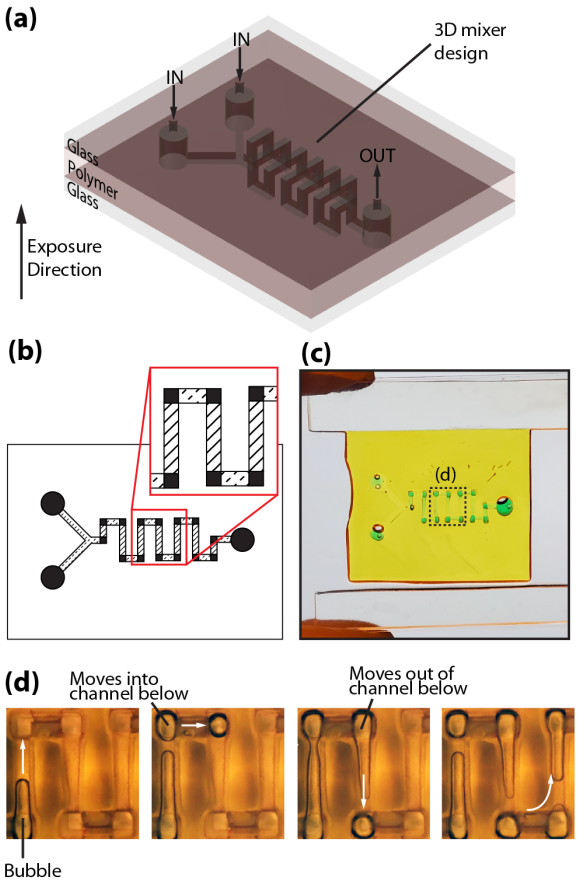

Figure 4.5: Three-dimensional multi-layer microfluidic mixer fabricated using dual-wavelength exposure. (a) Schematic of the channel layout. (b) Channel layout using the key from Fig. 4.4. (c) Macroscopic photograph of the prepared device with channels filled with blue food coloring. In this design the front and backside channels were 2000 μm wide and 400 μm deep. (d) Micrograph of region outlined in (c) showing a series of bubbled moving through the channel

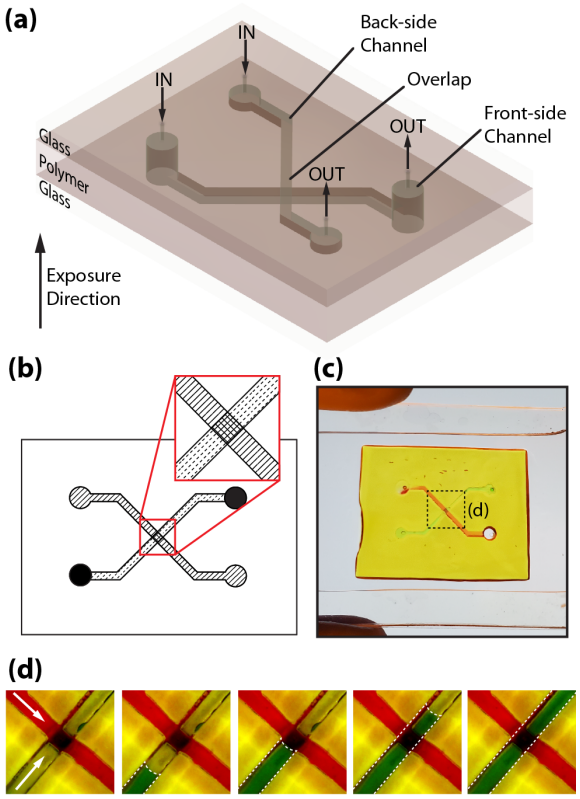

Figure 4.6: Multi-layer microfluidic device with crossing channels fabricated using dual-wavelength exposure. (a) Schematic of the channel showing flows and sandwich fabrication. (b) Channel layout using the key from Fig. 4.4. (c) Macroscopic photograph of a device with channels filled with blue and red food dye. In this design the front and backside channels were 2000 μm wide and 400 μm deep. (d) Micrograph of region outlined in (d) showing showing fluid flowing through each of the channels and overlapping without mixing.

CHAPTER V

Variable-Height Channels for Microparticle Separation and Display

This work was done in collaboration with Dr. Sarah Mena. My contributions were in the conception of the project, model development, device preparation and experimental data analysis.

5.1 Introduction

Separating cells and particles into distinct populations in microfluidic devices is a critical operation in many biomedical assays.[99, 100] Current methods for separating cells and particles can be categorized into active and passive methods. Active methods use external fields, such as magnetic,[101] electric,[102] or acoustic[103] forces, to exact separations. Passive methods rely on the interactions between the microchannel geometry and flow field,[104] and current methods include, flow fractionation,[105, 106] deterministic lateral displacement (DLD),[107] and filtration. Filtration is one of the most widely used passive techniques with separation achieved by size-exclusion using micro-structures such as weirs, pillars, or membranes incorporated into devices.[108] These devices are typically fabricated using conventional PDMS-glass microfabrication techniques[109] or silicon deep reactive ion etching (DRIE),[108] and are designed with openings or obstacles of targeted

size to achieve the desired separation. The conventional method of glass microfluidic device fabrication is wet etching with hydrofluoric acid (HF). Wet etching of glass produces channels of uniform height and has found limited applicability in fabrication of size-based μ-particle filters due its isotropic nature, which hinders fabrication of small aspect-ratio microstructures. In this work, we present a new wet etching protocol for fabricating variable-height glass microfluidic channels. We achieve variable height etching by using a linear stage to slowly lower wafers into an HF etchant solution. Etching in this way spatially controls exposure to the etchant and reproducibly creates channels with height variation along the length of the channel. Astute choice of this height variation allows μ-particles mixtures of discrete size distributions to be easily separated, trapped, and displayed. Since size fractionation is achieved by changes in the channel depth, relatively wide channels can be used for high-capacity trapping of large numbers of μ-particles before clogging. Microstructures with varying heights have previously been fabricated by grayscale photolithography[110, 111], and additive manufacturing[112], however channels prepared by these methods have not demonstrated height variation appropriate for μ-particle separation. Additionally, these methods require special equipment,[113] careful tuning of the properties of the photoresist,[114] and (in the case of additive manufacturing) are limited to accuracies in the z-direction on the order of 10 μm[15]. In addition to size-based separations, the devices can be used to measure the deformability of particles such as red blood cells (RBCs) These cells, typically 7.5-8.7 μm in diameter, routinely navigate 2-3 μm blood vessels in the microcirculatory system.[115] Diseases such as malaria, sickle cell disease, and diabetes are known to reduce RBC deformability.[116, 117, 118] Furthermore, the deformability of circulating tumor cells (CTCs) has been correlated to invasiveness with highly-

invasive CTCs having increased deformability.[119] Currently, there are no readily-available techniques for the assessment of RBC deformability in the clinical setting. Ektacytometry, which is used widely for RBC deformability measurements in research settings,[120] has not been widely implemented due to high equipment costs. Other notoriously cumbersome techniques[121] routinely used to study single RBCs include pipette aspiration,[117] atomic force microscopy (AFM),[117] and optical tweezers.[122] In recent decades, many innovative microfluidic devices have been proposed to measure RBC deformability based on a variety of direct and indirect methods including cell displacement measurements,[123, 124, 125] measurements of threshold pressure to drive cells through small constrictions,[126] observations of the cell shape under different flow fields,[127] changes in electrical signals,[128] and levitation in magnetic mediums.[129] . In our variable-height devices, the stopping distance (at constant pressure) can be used as a metric for RBC deformability. The ease-of-fabrication, simple operation, and macroscopically visible results make the devices described here a viable method of easily extracting qualitative results for both multiplexed μ-particle assays and as a measuring tool for cell deformability studies.

5.2 Materials and Methods

5.2.1 Wafer Preparation

Borofloat wafers (Precision Glass & Optics) were annealed for one hour in a furnace at 560 °C (Tempress S6T1) and piranha cleaned. A 200/2000 Å Cr/Au metal mask was evaporated onto the clean wafers with an electron beam evaporator (DV-502A, Denton Vacuum). Subsequently, a 3 μm layer of S1827 positive photoresist (MicroChem) was spin coated following the manufacturers specification and exposed for 15 s with 365 nm at 20 mW/cm^2 using a low-cost photomask sheet (Fineline

Imaging). Exposed wafers were developed for 60 s in AZ 726 (MicroChem). Au/Cr layers were removed by etching for 45 s in TFA gold etchant (Transene) and 10 s in CR- 1020 chrome etchant (Transene). To further protect from pinholes during etching, the photoresist was left on during the HF etching step. Inlet and outlet ports were drilled in a second glass wafer (Precision Glass & Optics) which was reversibly bonded to a backing wafer using Crystalbond 555 (Ted Pella) heated to 70 °C. Drilling layouts were prepared in Autodesk Fusion 360 and exported as gcode to a CNC router (Tormach PCNC). A peck-drilling operation with a 750 μm diamond micro drill (Amplex S-Series .030") was used with a drill speed of 10 000 RPM, peck height of 100 μm and feed rate of 5 mm/min.

5.2.2 Variable Height Etching

To create variable height devices, the masked wafers were gradually introduced into the HF etchant solution using the linear screw mechanism of a syringe pump (Harvard Apparatus, PHD 2000) modified with a 3D-printed Nylon adapter designed to hold wafers (Fig. 5.1(a)) The concentration of the etchant solution used in experiments ranged from 20 to 49% w/w (Note: HF is an extremely hazardous chemical and specific safety protocols should be followed including proper use of containers, engineering controls, and personal protective equipment). The 49% w/w HF was used as received from the manufacturer, and lower concentrations were prepared by diluting the stock HF solution with deionized water. The movement of the wafer into the HF was controlled by manually varying the flow rate of the syringe pump. After the channel were etched, the wafer was lifted out of the beaker and rinsed with deionized water for at least 5 min. After the etching step, the photoresist was removed with acetone, isopropyl alcohol, and hot PRS 2000 (J. T. Baker), and the Au/Cr layers were removed with their corresponding etchants (described above). The resulting

etched channels were measured using either a surface profilometer (Alpha Step 500, KLA-Tencor) or interferometer (Zygo NewView 5000).

5.2.3 Sized-Based μ-Particle Separation Experiments

Microparticles were purchased from Spherotech in different sizes and fluorescence such that only one type of particles is visible using the different optical filters in the microscope (Nikon inverted microscope Ti-S) as shown in Appendix D.1. The as-received particles were diluted with a phosphate buffered saline (PBS) (1x, 5% bovine serum albumin (BSA)) for those with mean diameters of 2.05$\pm$0.303 μm (goat anti-mouse IgG sky blue, MFP-2070-5), 6.20$\pm$1.15 μm (biotin coated pink, TFP-5058-5), and 7.37$\pm$0.591 mm (biotin coated yellow, TFP-705205) or a 0.05% v/v solution of Tween 20 in DI water for those with diameters of 3.36$\pm$0.662 μm (sky blue, FP-3010-2), 3.27$\pm$0.506 μm (nile red, FP-3056-2), and 3.25$\pm$0.554 μm (yellow, FP-3052). Channels were primed for one hour with the same PBS solution prior to experiments with non-FP-type particles, channels were not primed for the experiments with the FP-type particles.

5.2.4 Deformability-Based RBC Separation Experiments

Packed RBCs, purchased from the University of Michigan Blood Bank, were used in all RBC experiments. The cells were stored at 4 °C until testing. 40 μl of packed RBCs was diluted in 1000 μl of PBS (1x, 5% BSA, pH = 7.4). Glass channels were primed with the PBS/BSA solution for one hour prior to testing to prevent interactions between the cells and the device walls. To modify the deformability of the packed RBCs, 600 μl of RBCs was diluted with a 39.4 ml mixture of 0.02% v/v glutaraldehyde in PBS (1x, pH = 7.4) and incubated for one hour using gentle rotation at room temperature (20°C). After incubation, the cells were washed

three times with PBS (1x, pH=7.4). For microfluidic flow experiments, 40 μl of the modified RBCs was suspended in 1000 μl of PBS (1x, 5% w/w BSA, pH=7.4). Approximately 0.25 μl of diluted unmodified and GA-modified RBCs (3.8% v/v) was flowed into PBS-primed channels. After introduction of the cells, PBS (1x, 5% w/w BSA, pH=7.4) was flowed for 15 min to drive cells through the device. To account for variations in the channel height due to fabrication, fluorescent particles (mean diameters of 2.05±0.303 μm, 6.20±1.15 μm, and 7.37±0.591 μm) were introduced into the channel as a reference. Prior to the introduction of the fluorescent particles, RBCs were removed from the channel by applying backflow with PBS or vacuum applied directly into the inlet. The position of the band of fluorescent particles was noted and used to calculate the height of each individual channel.

5.2.5 Flow Experiment Protocol

The sample of suspended particles or cells was placed into a modified centrifuge tube. The centrifuge tube was adapted by drilling two holes to accommodate the pressure input (McMaster Carr, stainless steel dispensing needles with luer lock connection) and the tube to deliver the sample to the device (0.51-mm ID tubing (McMaster Carr, ETFE Tubing, 1.59 OD)) (see Fig. D.1). Tubing was connected to the inlet of the channel using a magnetic microfluidic adapter (Cor-Solutions microfluidic connectors BMP-LP-2X) and pneumatic pressure applied to drive flow into the channel.

5.2.6 Image Analysis Method

The threshold values of microscopy images (2048x1536 or 1920x1200 px) were adjusted in ImageJ to eliminate background noise and improve the visibility of particles. A grid with 250x250 μm squares was centered and overlaid on the image. The

Analyze Particles feature in ImageJ was used to count particles present in each 250 μm vertical slice of channel, the vertical box encompassed either the entire channel or the middle 40% (see Fig. D.2). This was repeated for all 250 μm vertical sections of the channel to give the distribution of particles along the channel length. To compensate particle agglomeration, the measured size of particles was divided by an average particle size (determined manually every 5 mm along the channel) and rounded to the nearest whole number.

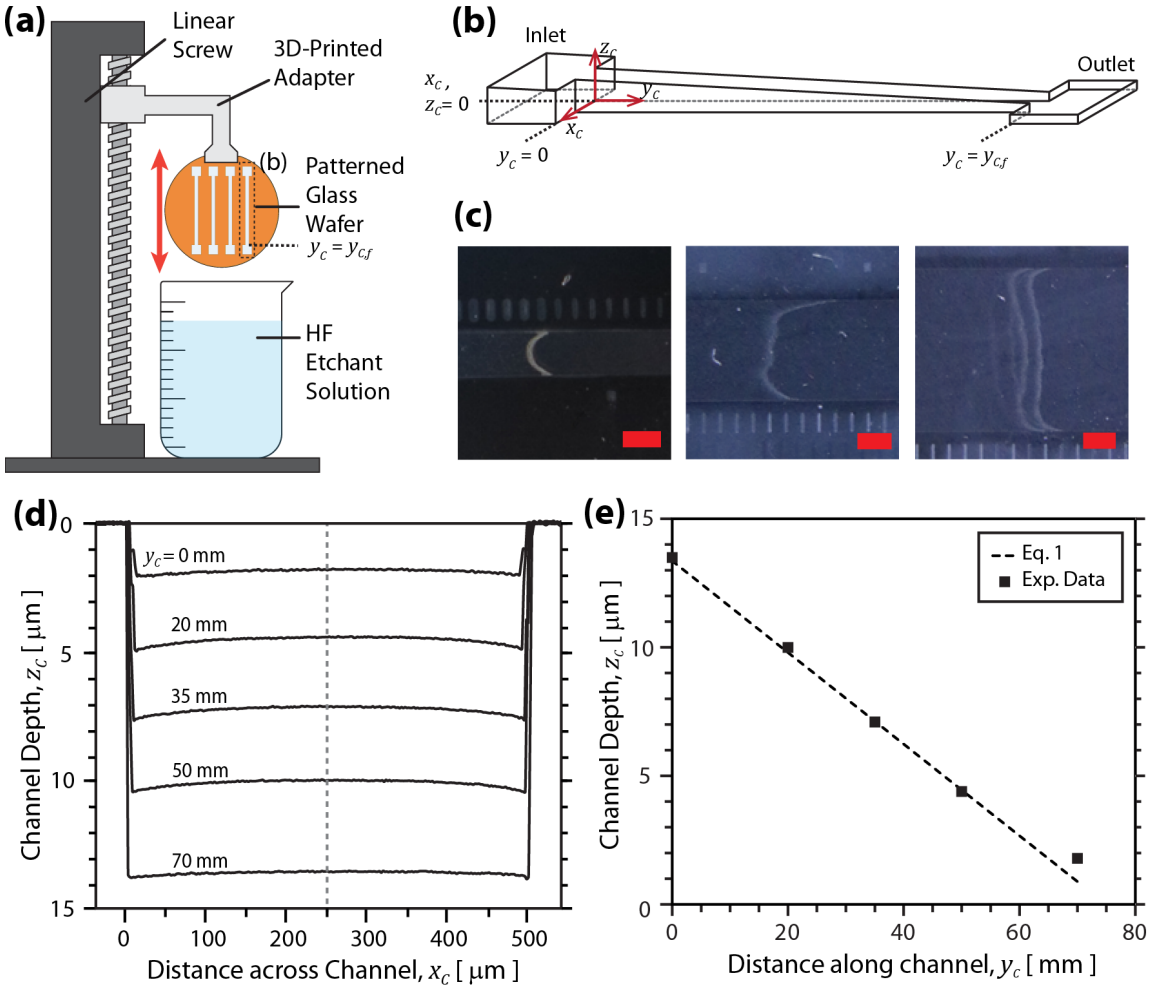

Figure 5.1: Fabrication of variable height channels. (a) Illustration of setup used to fabricate variable height microfluidic channels. (b) Co-ordinate system used where $y_c = 0$ is at the entrance of the channel. (c) Macroscopic images showing the curvature of the trapping region for channel widths of 1.25, 3 and 5 mm channel widths. Scale Bar = 1 mm . (d) Variation of the etched depth, z_c, across the width of the channel, x_c, at various distances along the channel. (e) Resulting height profile along the length of the channel. The experimental data are the etched depth measured at the centre of the channel (as shown by the dashed gray line in (d)) using a 3D interferometer (Zygo NewView 5000). The dashed line is the predicted depth of the channel according to equation 1 using the fabrication parameters for this wafer (R= 0.34 μm/min, s=1.9 mm/min.)

5.3 Results & Discussion

5.3.1 Variable Height Channels

Variable height channels can be fabricated by a simple procedure using non-uniform exposure to HF etchant. In the procedure, a wafer with a Cr/Au/photoresist

etch mask, patterned by conventional photolithography, is lowered into an HF solution by a linear screw actuator at an arbitrary but controlled speed (Fig. 5.1(a)). A schematic view (with coordinate system) of the resulting etched channel is shown in Fig. 5.1(b). For a wafer lowered at constant velocity, s, the etched-depth of the channel, z_{c}, is described by the straight-line equation (see Appendix D.4.1):

$$z_c = \frac{R}{s}(y_{\mathrm{c,f}} - y_{\mathrm{c}})\mathrm{u}(y_{\mathrm{c,f}} - y_{\mathrm{c}}) \tag{5.1}$$

Where R is the etch rate of the wet etchant, $y_{\mathrm{c,f}}$ is the distance along the channel at which movement stops, y_{c} is the channel position, and "u(x)" is the unit step function. Practically, it is difficult to achieve very small final heights (i.e. channel exit heights) using only this method due to residual etching from the HF before the post-etch rinse and vapour-phase HF etching that is observed above the liquid level. Instead, for these cases, specific channel exit heights were obtained by a two-step etching process. The first step involved constant-speed lowering of the wafer partway into the etchant solution, removing, and washing. The second step was a conventional whole-wafer etch for the appropriate time to achieve the desired height, t_{etch}. This two-step approach gives more controllable and consistent channel exit heights. For this case Equation 1 is modified to give:

$$z_C = \frac{R}{s}(y_{\mathrm{c,f}} - y_{\mathrm{c}})\mathrm{u}(y_{\mathrm{c,f}} - y_{\mathrm{c}}) + Rt_{\mathrm{etch}} \tag{5.2}$$

As an example, for an experimentally determined etch rate of 7.8 μm/min using a 49% w/w HF solution on annealed borosilicate glass, the residual etching occurring during the post-etch rinse step with this relatively high etch rate prevents fabricating channels with exit heights below 3 μm. Dilution of the 49% w/w HF to 20% w/w decreased the etch rate to approximately 0.3 μm/min, significantly reducing the

residual etch and providing better accuracy when etching shallow channels. Specifically, lowering wafers at 1.8 mm/min into 20% w/w HF to a depth of 55 mm, followed by 2.25 min of uniform etching forms channels with a height varying linearly along the length of the channel from 15 to 2 μm (Fig. 5.1(e)). The ratio of the etch rate to the wafer velocity (R/s) ultimately determines the slope of the channel. Therefore, for a fixed etch rate, adjusting the speed allows any desired slope to be obtained (see Fig. D.3). The etched depth is found to vary across the width of the channel, x_c, as seen by the trapping of particles in Fig. 1c and the interferometry measurements in Fig. 5.1(d). The depth at the center of the channel is found to be lower than at the edges by 250-500 nm. We suspect that this is due to surface tension effects during the etching process that cause HF to creep up along the channel edges (see Fig. D.4) and, as a result, etch the edges longer. Fabricating channels of larger widths, as shown in Fig. 5.1(c), diminished the lateral channel height variation. Note that the curvature of the trapped particles is caused by the height variation across the channel and not the parabolic flow profile within the channel.

Using a programmable linear screw, it is possible to program arbitrary velocity profiles for the wafers movement into the HF. The analytical solutions for constant and changing acceleration are derived in Appendix D.4.1 (more complex velocity profiles may yield interesting results but will need to be modelled numerically). To probe the different profiles that can be achieved, we varied a number of parameters in the variable height etching procedure. The varied parameters were (1) the speed of the immersion of the wafer into the etchant; (2) the acceleration of the immersion of the wafer into the solution; (3) the concentration of the etchant solution; and (4) the inclusion of pauses in the protocol. Table 5.1 gives the details for the different conditions used for Fig. 5.2 (a) and (b). Accelerating the wafer into the etchant

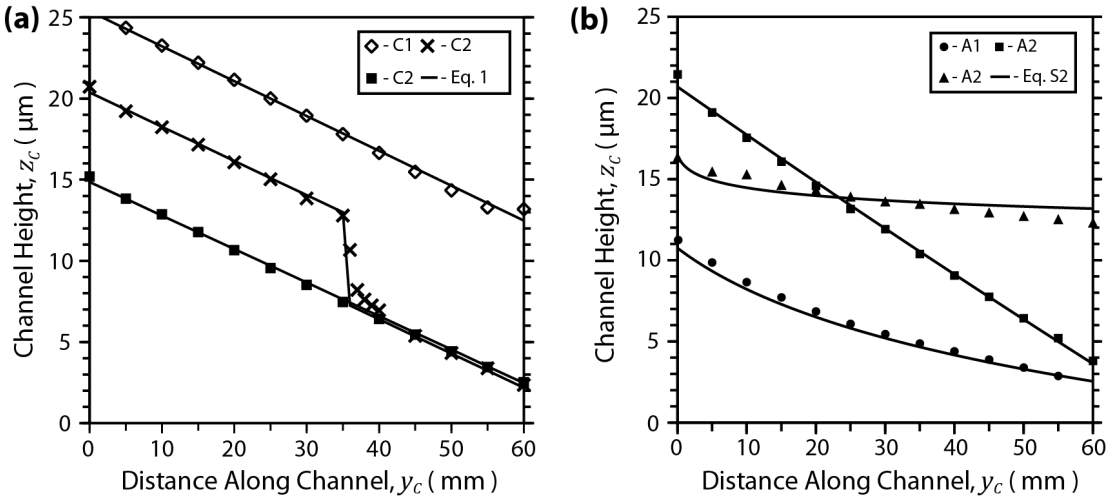

Figure 5.2: Channel height profiles obtained using different protocols for the introduction of the wafer in the etchant solution. (a) Protocols with a constant speed resulting in linear profiles, and (b) protocols with an acceleration resulting in quadratic profiles. Including pauses in the displacement of the wafer can create sharp steps as depicted in the curve with "x" in (a).

results in curved height profiles (see Fig. 5.2(b)). The amount of curvature is dependent on the degree of acceleration with velocity profiles with low acceleration tending towards straight lines.

Table 5.1: Parameters used in the fabrication of the different profiles in Figure 5.2

Protocol	HF (w/w %)	Initial Speed (cm/min)	Acceleration (mm/min^2)	Pause (min)	Uniform etch time (min)
C1	35	3.76	0	-	19
C2	20	1.88	0	-	2.25
C3	20	1.88	0	-	2.25
A1	20	1.54	0.01	-	0
A2	20	1.71	1.03	-	20
A3	20	1.71	0.21	-	2.25

5.3.2 Sized-Based Particle Separation

The ability of variable height channels to separate particles based on size was investigated. Three types of suspended fluorescent particles with mean diameters, D_p, of 2.05 μm, 6.20 μm, and 7.37 μm, and concentrations in an aqueous buffer solution of 0.1, 3.8, and 6.1% w/v, respectively, were simultaneously introduced using 86.9 kPa pressure into a single 1.25 mm wide channel with measured inlet and outlet heights of 15.7 μm and 1.4 μm, respectively. After flowing the solution for 10 min followed by a 5-10 min rinse with the PBS-BSA solution, the beads are trapped in three distinct positions in the channel according to their size. The regions where particles are trapped are clearly distinguishable by the naked eye, as shown by the macroscopic image in Fig. 5.3(a), and form the above-mentioned parabolic profile due to the height variation across the channel. The images in Fig. 5.3(b) were analysed with ImageJ using the above-described method (see Fig. D.2). The fraction of particles of each size in the center of the channel as a function of the distance along the channel, y_c, is plotted in Fig. 5.3(c). The distribution of particles along the length of the channels form sharp peaks with widths related to the size distributions of the supplied particles. The larger particles trapped across a wider distance (i.e. the 7.37 and 6.2 μm) had wider manufacturer-specified size distributions with standard deviations of 0.59 and 1.15 μm, respectively, compared to the 2.05 μm particles with a standard deviation of 0.3 μm. Analysis of the entire channel width is qualitatively similar but with a wider spread in the distributions due to the variation of the etch near the channel edges (see Fig. D.2). Variability between channels fabricated on the same wafer is quantified by the standard error between the size distributions for three experiments (as shown in by the shaded gray-region in Fig. 5.3(c)). The repeatability of particle capturing is consistent with particles being trapped within

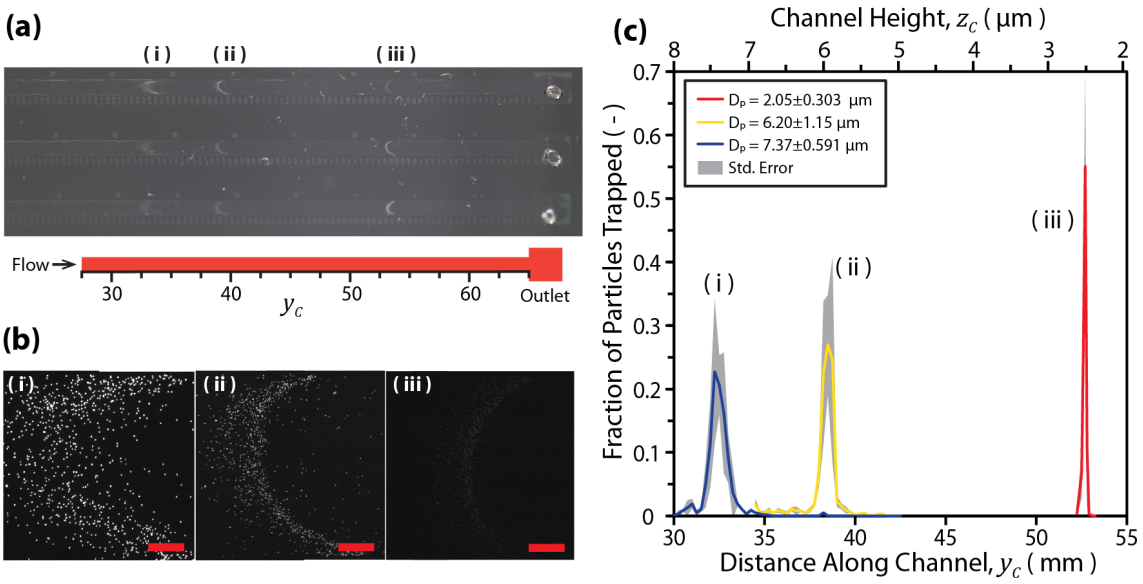

Figure 5.3: Separation of fluorescent particles by size in a variable height channel. (a) Macroscopic photograph showing three channels were fluorescent particles with three different sizes are reproducibly trapped in different regions of the channel according to their size. (b) Microscopic images of the three different particles with sizes (i) 7.37 μm particles, (ii) 6.20 μm, and (iii) 2.05 μm. The images show that the trapping occurs in a u-shaped region caused by the etching process All scale bars are 100 μm (c) Histograms showing the fraction of the particles trapped at different channel heights. Solid lines are histograms measured at the center of the channel, dashed lines are histograms measured in the center part of the channel, and the shaded area are the standard deviation of the histograms calculated from the three channels shown in (a).

0.5 mm across all three channels. The variability in the trapping position is most likely due to small misalignments of the wafer to the HF etchant liquid level during the fabrication process. The minimum size difference between particles required for separation in these devices is an important quantity. To investigate this, separations were attempted on sets of particles with close size distributions. Simultaneously introducing 3.358±0.662 μm (sky blue) and 3.272±0.506 μm (Nile red) , with concentrations of 0.005% w/v for both sizes resulted in particles being separated into two distinct bands after only a few minutes of flow (Fig. 5.4(a)). Quantitative analysis of the trapped particles in Fig. 5.4(a) reveals a clear difference (∼1 mm) between the trapping positions for these sizes (Fig. 5.4(b)). Flowing the particles for longer resulted in a linear increase in the number of particles being trapped (Fig. 5.4(b)),

resulting in bright, more-easily discernible bands. Furthermore it is seen that, as time progresses and the channels become more clogged with particles, the small particles begin to be trapped among the large particles. Experiments with particles of 3.272±0.506 μm and 3.246±0.554 μm in the same channel did not result in distinct bands at any point in time (Fig. 5.4(d)). Whether sets of particles of particular size distributions will separate into distinct, discernible bands depends on the slope of the channel (assuming appropriate channel height for trapping) and the size difference between the particles. Assuming 0.5 mm is required to visually distinguish bands of particles, the minimum difference in particle size, Δd, required to be separated in a channel of slope, m, is given by:

$$\Delta D_p = 0.5m = 0.5(R/s) \tag{5.3}$$

For the channel used in these experiments, with $R = 0.37$ m/min and $s = 1.75$ mm/min, the required difference ΔD_p is approximately 100 nm. This supports the experimental observation that particles with $\Delta D_p \approx 90$ nm are distinguishable however those with $\Delta D_p \approx 26$ nm are not. It is important to note that the slope of the channel can be adjusted to better separate narrow size distribution particles.

5.3.3 Deformability-Based Separation

At a set pressure, deformable particles should flow into smaller heights in the channel than more rigid particles.[119] To investigate whether the variable height channels could separate cells with different deformabilities, we used healthy RBCs and RBCs whose deformability had been chemically modified with glutaraldehyde (GA). GA has been extensively used in several studies to decrease RBC deformability.[121, 123, 125, 126, 130, 119] Note that, at the concentration of GA used in our experiments (0.02 wt.%) there was no change in the size of the cells, and

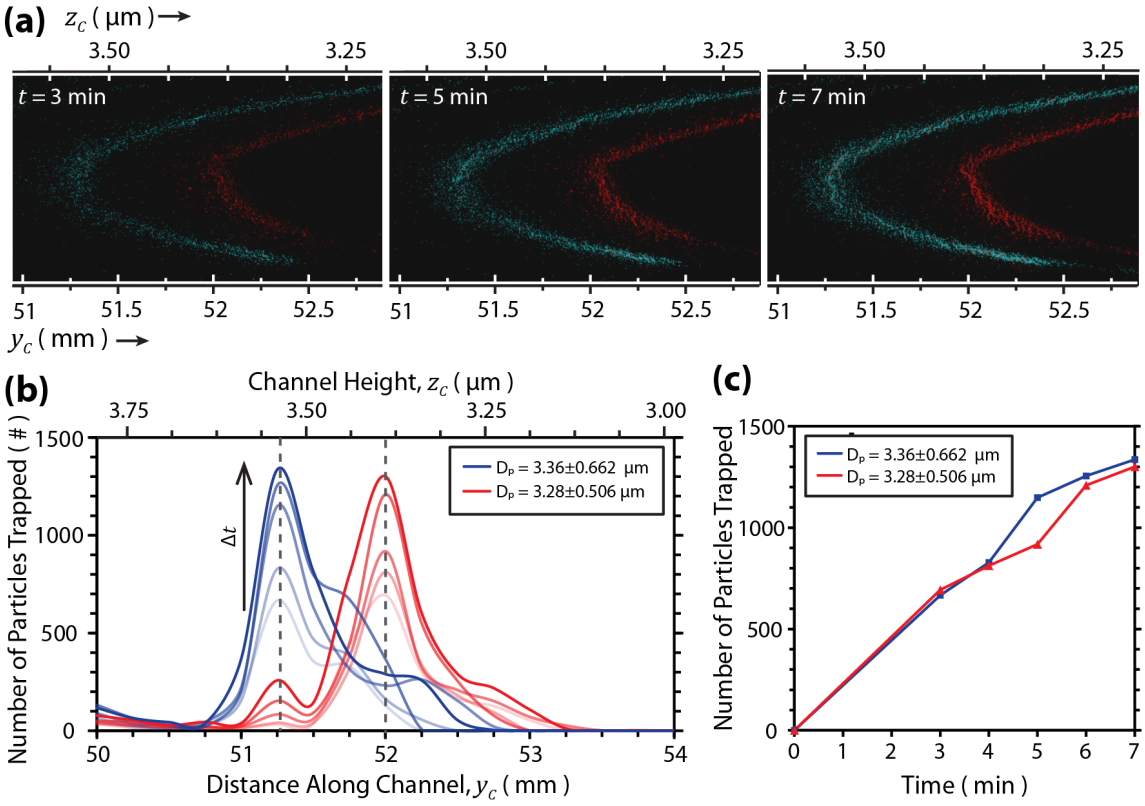

Figure 5.4: (a) Microscopic images showing the separation of two types of fluorescent particles with sizes of 3.358 μm (cyan) and 3.272 μm (red) at 7 minutes of flow (b) Number of particles trapped at different positions in the channel at different times for two particles with $\Delta D_p \approx$90 nm (c) Total number of particles trapped as a function of time. (d) Microscopic image of particles with mean diameters of 3.272 μm (red) and 3.246 μm (yellow) trapped in the same channels as those in (a). Images were coloured from grayscale images using ImageJ.

the inlet pressure (37.2 kPa) used is suitably low for application in portable, manual injection, point-of-care systems. The cells were injected into channels with an inlet height of 13.9 μm and an exit height of 1.3 μm. Fig. 5.5(a) shows that healthy cells are able to progress much further down the channel and squeeze into shallower channel heights than the GA-modified RBCs. Fig. 5.5(b) shows pictures images of the different regions in the channel taken with a 20x objective. Note that healthy RBCs are present in areas of the channel where the height is <2 μm, whereas there are almost no GA-modified RBCs past a channel height of ≈2.25 μm. Fig. 5.5(c) shows the quantitative analysis of the number of trapped cells using the method described

above. The difference in stopping points between the healthy and GA-modified RBCs is clearly apparent and found to be ≈4 mm. The same experiments were conducted on RBCs from two additional donors, and these experiments produced similar results (Fig. D.5).

5.4 Conclusions

We present a novel and simple fabrication procedure to create channels of variable height. Channel height profiles that are curved, linear, or have discontinuous steps can be formed by simply modifying the velocity of the wafer into the etchant solution. Experiments with particles and cells in these channels demonstrated that both size-based and deformability-based separations can be performed. The ability of these channels to separation different sized particles is dependent on the slope of the channel, which can be easily modified by adjusting the fabrication procedure. Application of for these devices in multi-analyte bead-based assays are plentiful and the macroscopic nature of the results, the simple operation, and the ease-of-fabrication make these devices a excellent candidate for use as point-of-care devices.

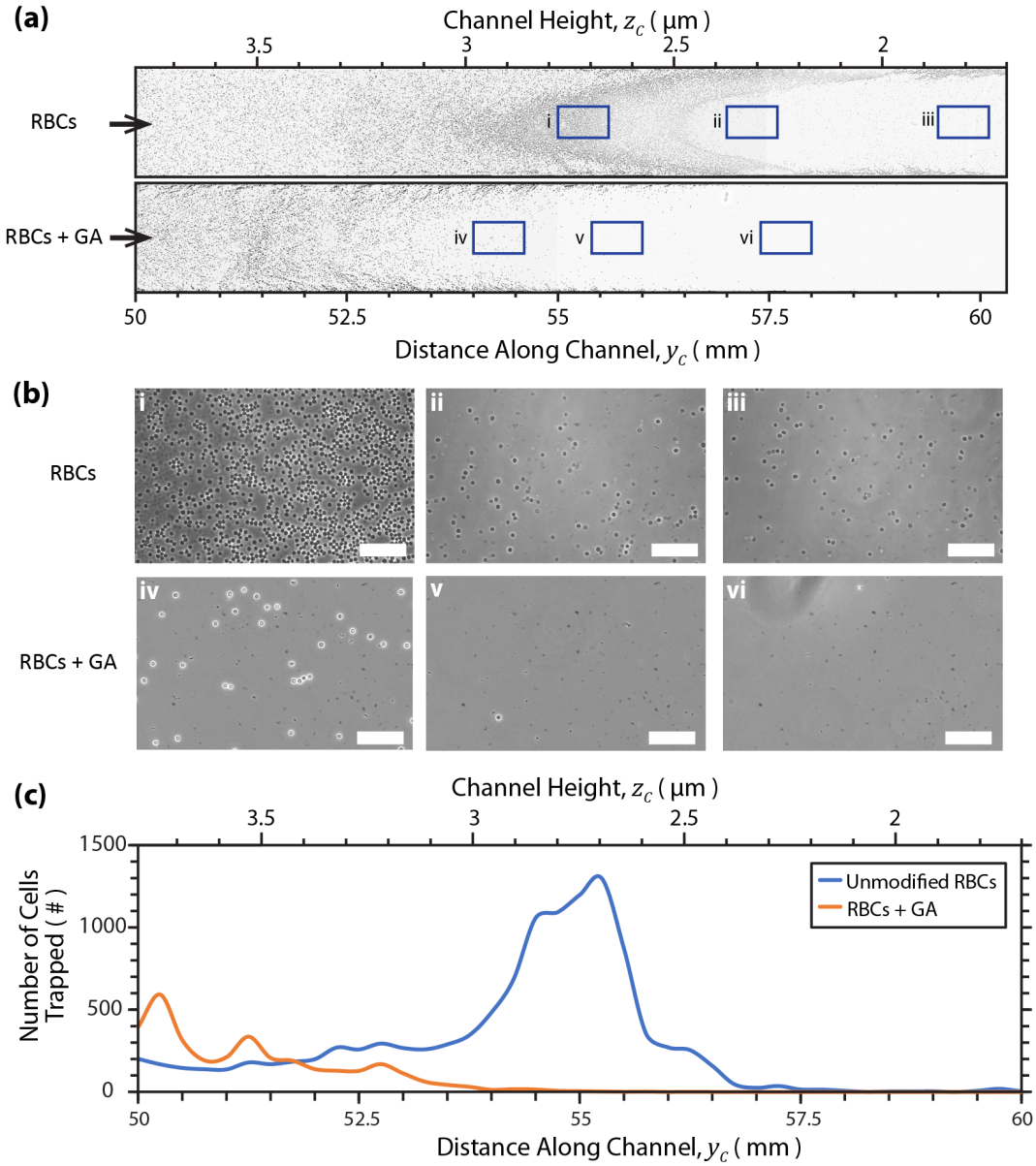

Figure 5.5: Trapping of Healthy RBCs with chemically modified deformability. (a) 4x images with a microscope of the section in the channel from 50-60 mm with heights between 3.2 and 1.6 μm. (b) 20x images of the cells trapped in the regions marked by blue rectangles in (a). The scale is 100 μm. (c) histograms of the number of RBCs trapped in the centre region of the channel between 50 mm and 60 mm with varying heights between 3.2 mm and 1.7 μm.

CHAPTER VI

CONCLUSIONS AND CONTINUING WORK

6.1 Conclusions

The aim of this dissertation work was to develop an alternative to oxygen-inhibition to facilitate rapid continuous additive manufacturing. Our investigation of photo-inhibition chemistry led us to discover *o*-Cl-HABI as a unreported photo-inhibitor molecule. *o*-Cl-HABI, when paired with a visible light photoinitiator (such as CQ), allowed controllable photo-inhibition and photo-initiation at two different positions in the absorbance spectrum (λ_{init} = 458 nm and $\lambda_{\text{inhib.}}$ = 365 nm. This light-controllable inhibition enabled dead zones orders of magnitude larger than those achievable with oxygen in a wide range of radical polymerization chemistries. The ability of these 'photo-inhibited' dead zones to facilitate continuous additive manufacturing was demonstrated by the development of the first ever dual-wavelength continuous additive manufacturing device. This device was able to continuously fabricate parts at speeds in excess of 2000 mm/hr - the fastest vertical print speed reported for continuous additive manufacturing at the time.

We found that high print speeds comes at the expense of unwanted curing beyond the desired geometry. In an attempt to achieve good part fidelity while maintaining high print speed we developed a model for the total accumulated dose within features

resulting from a given set of exposure projections. This allows us to define constraints and elucidated the form of achievable accumulated dose profiles within features in continuous AM. By algorithmically modifying the projected images we are able to match desired dose profile experimentally and reduce the appearance of cure-through by almost 90% in test models. This framework can be extended to deliver desired dose profiles in resins with dose-specific material properties, potentially increasing the functionality and application-space of additive manufacturing.

The ability of photo-inhibition to be easily controlled using projected light led us investigate its use in microfluidic device fabrication. Grayscale projection enables microfluidic channels of sub-millimeter heights to be fabricated in less than a minute from a single exposure. Additionally, multi-layer microfluidic devices can be fabricated in this process with no significant increase in fabrication time. This work reduces the skill associated with microfluidic device fabrication, lowering the financial and technical barrier-to-entry of this technology and potentially providing an avenue for wider-adoption of this technology.

Finally, the variable height fabrication procedure enables any arbitrary channel height profile by modifying the velocity of the wafer into the etchant solution. These channels are able to separate cells and particles based on their size or deformability. Since the slope of these channels are easily modified by adjusting the parameters used during fabrication this technique is applicable to any size distribution of microparticle. Possible application of these devices in multi-analyte bead-based assays are plentiful and the macroscopic nature of the results, the simple operation, and the ease-of-fabrication make these devices an excellent candidate for use as point-of-care devices.

6.2 Continuing Work

6.2.1 Investigation of Alternative Photoinhibitors

As previously mentioned, *o*-Cl-HABI forms exceptionally stable radicals upon ultraviolet irradiation. This stability gives *o*-Cl-HABI the ability to photo-inhibit polymerization in the presence of a suitable reducing basem, but also imparts the lophyl radicals generated upon photo-cleavage with extremely long solution half lives (on the order of 45 s). These long-lived, polymerization-inhibiting radicals have a significant effect on the printing process. These radicals are entrained in the resin flowing to replace the polymerizing resin in the growing part. This ultimately results in inhibition within the part, poor polymerization and hollow features. We hypothesize that decreasing the half life of the inhibiting radicals will decrease this effect and improve the printing process. Previous work shows a significant effect of substitution on the rate of radical disappearance [94]. An exploratory study into the inhibition activity of commercial and synthesized HABIs with different radical recombination rates may identify photoinhibitors with improved performance for continuous AM.

6.2.2 Flow Modelling for Slice Optimization

Another possible direction to address the poor curing within parts due to lingering inhibition of the lophyl radicals may be flow modelling coupled with slice modification. Finite element modelling can be used to model the flow within the dead zone beneath the growing part. Coupling the flow model with radical conservation equations allows us to describe the location and concentration of inhibiting radicals during the printing process (i.e. during exposure). Varying the images projected during printing effects the generation of radicals and we hypothesize can be used to obtain the desired lateral distribution of inhibiting radicals - enabling continuous

printing while minimizing adverse lingering inhibition.

6.2.3 Multi-Analyte Assays in Variable Height Microchannels

We have shown the ability of variable height devices to separate microparticles based on their size and/or deformability. If we incorporate functionality into these microparticles, such as a bead-based fluorescence assay, we can achieve an extremely simple, easy-to-use point-of-care device. The height of the channel can be tailored to exact clear separations between particles, and because only small distances are required to detect different size particles in theory the results from tens or hundreds of assays can be gleaned on a single device.

APPENDICES

APPENDIX A

Rapid, Continuous Additive Manufacturing by Volumetric Polymerization Inhibition Patterning

A.1 Derivation of Equation 2.1

The intensity of a beam of light of a given wavelength at any distance (x in an absorbing medium is given by the Beer-Lambert Law and is dependent on the incident intensity (I_0), the wavelength specific molar absorptivity of the absorbing species (ϵ), the molar concentration of the absorbing species (c), such that:

$$I(x) = I_0 10^{-\epsilon c x} \tag{A.1}$$

The reaction rate for photopolymerization in the present of a photoinhibitor has previously been shown to be dependent on the intensity of the initiating and inhibiting wavelengths, in this case blue and UV respectively, (I_{blue} and I_{UV}), the inhibition coefficient (β)—a constant that encompasses the ratio of inhibitor to initiator absorption cross section, quantum yields, and reaction rate constants—and the reaction rate constant (k). The reaction rate is thus:

$$R_{\text{poly}} = k(I_{\text{blue}} - \beta I_{\text{UV}})^{0.5} \tag{A.2}$$

Combining the above equations yields an equation for the reaction rate as a function of the distance into the absorbing media, where:

$$R_{\text{poly}} = k(I_{\text{blue},0}10^{-\epsilon_{\text{blue}}c_{\text{blue}}x} - \beta I_{\text{UV},0}10^{-\epsilon_{\text{UV}}c_{\text{UV}}x})^{0.5} \tag{A.3}$$

In the inhibition volume (IV), the rate of polymerization is zero since there is by definition no reaction, such that:

$$0 = k(I_{\text{blue},0}10^{-\epsilon_{\text{blue}}c_{\text{blue}}x} - \beta I_{\text{UV},0}10^{-\epsilon_{\text{UV}}c_{\text{UV}}x})^{0.5}$$

$$0 = (I_{\text{blue},0}10^{-\epsilon_{\text{blue}}c_{\text{blue}}x} - \beta I_{\text{UV},0}10^{-\epsilon_{\text{UV}}c_{\text{UV}}x})$$

$$I_{\text{blue},0}10^{-\epsilon_{\text{blue}}c_{\text{blue}}x} = \beta I_{\text{UV},0}10^{-\epsilon_{\text{UV}}c_{\text{UV}}x} \tag{A.4}$$

We can define the absorbance height at a given wavelength, h_i, as:

$$\epsilon_i c_i = 1/h_i \tag{A.5}$$

Substitution yields:

$$I_{\text{blue},0}10^{-x_{\text{DZ}}/h_{\text{blue}}} = \beta I_{\text{UV},0}10^{-x_{\text{DZ}}/h_{\text{UV}}}$$

Rearrangement:

$$10^{-x_{\text{DZ}}/h_{\text{blue}}+x_{\text{DZ}}/h_{\text{UV}}} = \beta(\frac{I_{\text{UV},0}}{I_{\text{blue},0}})$$

Solving for x_{DZ} yields:

$$x_{\text{DZ}} = \frac{\log_{10}(\frac{\beta I_{\text{UV},0}}{I_{\text{blue},0}})}{\frac{1}{h_{\text{UV}}} - \frac{1}{h_{\text{blue}}}} \tag{A.6}$$

For the dead zone thickness to be identically zero, the numerator of this equation needs to equal zero, such that:

$$0 = \log_{10}(\frac{\beta I_{\text{UV},0}}{I_{\text{blue},0}})$$

$$1 = \frac{\beta I_{\text{UV},0}}{I_{\text{blue},0}}$$

$$1/\beta = \frac{I_{\text{UV},0}}{I_{\text{blue},0}} \tag{A.7}$$

This gives the minimum $I_{\text{UV}}/I_{\text{blue}}$ ratio which results in an inhibition volume.

A.2 Derivation of Equation 2.2

In a bottom-up 3D-printing application, the intensity of initiating light from the projection window is given by the Beer-Lambert Law, where:

$$I_{\text{blue}}(x) = I_{\text{blue},0}10^{-x/h_{\text{blue}}} \tag{A.8}$$

Integrating this for all exposure times gives the total applied dosage for any vertical position, such that:

$$E_{\text{blue}} = \int_0^{\infty} I_{\text{blue},0}10^{-x/h_{\text{blue}}}dt \tag{A.9}$$

Since the build head is translating at speed, s, the position relative to the print window is given by:

$$x(t) = x_0 + st \tag{A.10}$$

Integrating over distance yields:

$$E_{\text{blue}} = \int_0^{\infty} \frac{I_{\text{blue},0}10^{-x/h_{\text{blue}}}}{s}dx \tag{A.11}$$

Since the inhibition is generated by another wavelength of light we can define a new critical dose which is required to cure the polymer and overcome the inhibition, where:

$$E_{\text{c}}^{*} = E_{\text{c}} + \int_0^{\infty} \frac{\beta I_{\text{UV},0}10^{-x/h_{\text{UV}}}}{s}dx \tag{A.12}$$

When the dose delivered by the blue light equals the critical dose the speed is at a maximum, since any additional dose is effectively wasted (i.e. $E_{\text{blue}} = E_{\text{c}}^{*}$), such that:

$$\int_0^{\infty} \frac{I_{\text{blue},0}10^{-x/h_{\text{blue}}}}{s_{\text{max}}}dx = E_{\text{c}} + \int_0^{\infty} \frac{\beta I_{\text{UV},0}10^{-x/h_{\text{UV}}}}{s_{\text{max}}}dx$$

Combining the integrals, integrating and solving yields:

$$\int_0^{\infty} \frac{I_{\text{blue},0}10^{-x/h_{\text{blue}}}}{s_{\text{max}}} - \int_0^{\infty} \frac{\beta I_{\text{UV},0}10^{-x/h_{\text{UV}}}}{s_{\text{max}}}dx = E_{\text{c}}$$

$$s_{\max} = \frac{I_{\text{blue},0} h_{\text{blue}} - \beta I_{\text{UV},0} h_{\text{UV}}}{E_{\text{c}} \ln 10} \tag{A.13}$$

This maximum rate is difficult to achieve owing to lingering lophyl radicals, mechanical properties of the curing resin, and liquid resin reflow into the inhibition volume. We can define an achievable maximum print speed, $S^*_{\max}$, which is what is observed experimentally, as:

$$S^*_{\max} = \eta S_{\max} = \frac{\eta (I_{\text{blue},0} h_{\text{blue}} - \beta I_{\text{UV},0} h_{\text{UV}})}{E_{\text{c}} \ln 10} \tag{A.14}$$

A.3 Supplementary Figures

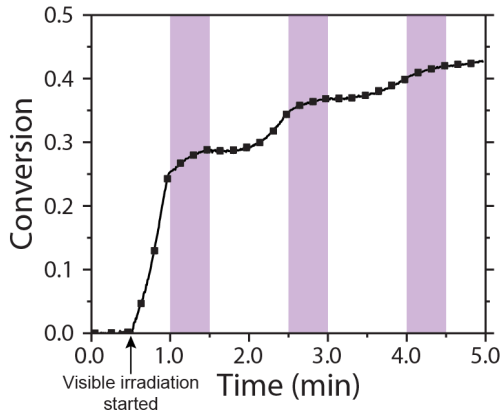

Figure A.1: Wavelength selective photoinitiation and transient photoinhibition of methacrylate polymerization. Methacrylate conversion versus time for bisGMA/TEGDMA formulated with CQ/EDAB and o-Cl-HABI under continuous irradiation, starting at 0.5 minutes, with 470 nm @ 100 mW/cm^2 and intermittent irradiation with 365 nm @ 30 mW/cm^2 during the shaded periods as indicated. Rapid polymerization proceeds upon visible light irradiation, while the accumulation of lophyl radicals during the 30 second UV irradiation periods afford decreased polymerization rates. Upon cessation of UV irradiation, the polymerization rates recover after induction times of approximately 30 seconds owing to the relatively slow consumption of lophyl radicals by recombination.

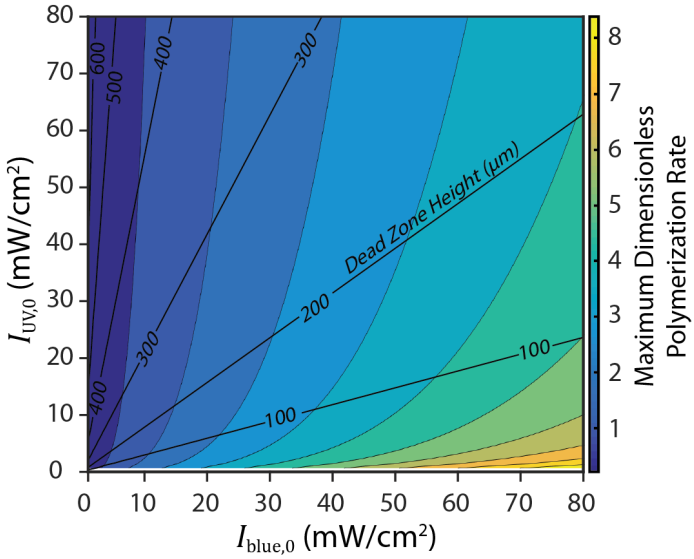

Figure A.2: Effect of incident UV and blue illumination intensities on inhibition volume thickness and polymerization rate. Adjustment of $I_{\mathrm{UV},0}/I_{\mathrm{blue},0}$ along an isorate line allows for adjustment of the inhibition volume thickness while maintaining the same polymerization rate. Additionally, raised polymerization rates can be attained for a given inhibition volume thickness.

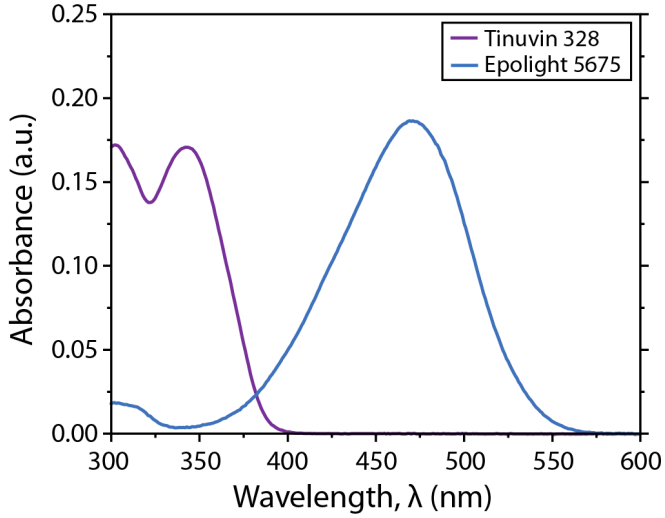

Figure A.3: UV-vis spectra of ultraviolet and blue light absorbers. The absorbance spectra of Tinuvin 328 and Epolight 5675 (1.1×10^{-4} M and 1×10^{-2} g/L, respectively) in isopropyl alcohol reveal no absorbance by Tinuvin 328 in the visible region of the spectrum and relatively low absorbance by Epolight 5675 in the near UV spectral region, enabling their use to independently control resin absorbance in the blue and near UV.

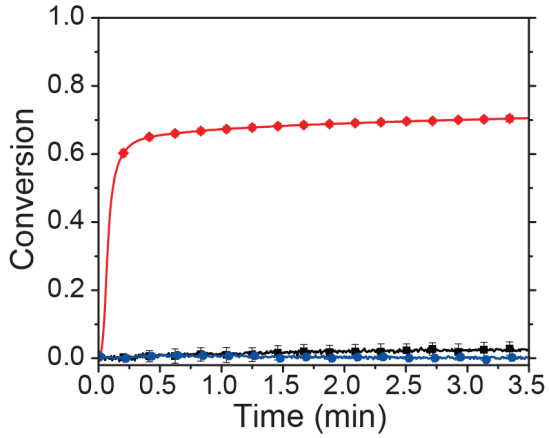

Figure A.4: Influence of co-initiator on *o*-Cl-HABI photoinitiation. Methacrylate conversion versus time for bisGMA/TEGDMA formulated with *o*-Cl-HABI and either no co-initiator (black line, squares), EDAB (blue line, circles), or MBT (red line, diamonds) under continuous irradiation with 365 nm @ 30 mW/cm^2. Whereas inclusion of MBT in the resin formulation results in rapid photopolymerization, the formulated methacrylate resin in the absence of a co-initiator exhibits negligible conversion upon UV irradiation. Similarly, no polymerization is observed during the irradiation of the resin formulated to include EDAB, indicating that the lophyl radicals are unable to generate polymerization-initiating radicals by hydrogen abstraction from the tertiary amine which can thus be employed as a CQ-selective co-initiator.

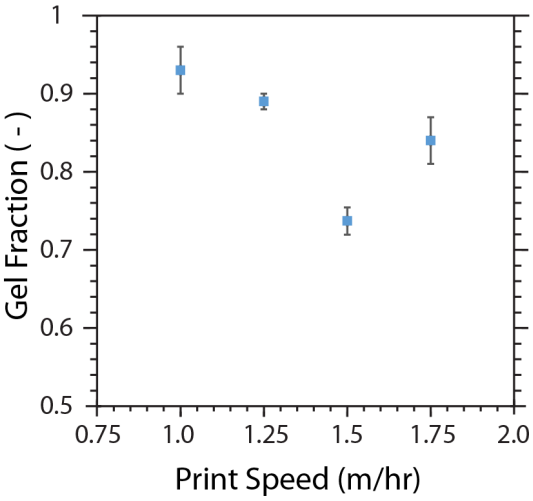

Figure A.5: Effect of print speed on the gel fraction of printed part. Gel fraction versus printing speed determined using Soxhlet extraction for printing resins with $h_{\text{blue}} = 4500$ μm and $h_{\text{UV}} = 100$ μm. Model used was a solid ($\phi = 0$) ASTM D638 Type V dog bone.

APPENDIX B

Modelling and Correcting Cure-Through in Continuous Stereolithographic 3D Printing

B.1 Derivation of Dose Equations

The build platform begins in contact with the window and moves upward as the print proceeds. The coordinate system is defined with respect to the build platform, with $z = 0$ at the platform and increasing in the direction of the window (downward). Since the projected slices are patterned and intensity degrades as the light propagates, dose and intensity are functions of x, y, and z; however, for simplicity our notation will only include z with the understanding that each equation applies at a particular (x, y) position. Printing consists of both continuous and discrete processes: as the build platform continuously ascends, exposure patterns change at discrete intervals with each slice projected in sequence. To account for the discrete projection of slices, the total accumulated dose at a point is a sum of contributions from each slice projected. $D_{\mathrm{T}}(z)$ is the total dose delivered to position z in the final part; the contribution of slice n to the total dose is denoted as $D_{\mathrm{n}}(z)$. Thus,

$$D_{\mathrm{T}}(z) = \sum_{n=0}^{N} D_{\mathrm{n}}(z) \tag{B.1}$$

where slices are numbered from 0 to N in the order of exposure. To determine the dose contribution from each slice as the build platform continuously ascends, we

integrate over the time period when the slice is projected. The change in dose at a point is given by:

$$\frac{d}{dt}D_{\mathrm{n}}(z,t) = I_{\mathrm{n}}(z,t) \tag{B.2}$$

where t is time and I_{n} is the light intensity for slice n. The light intensity at any depth in the resin bath, $I_{\mathrm{n}}(z)$, is given by Beer's Law. Recalling that $z = 0$ at the build platform, $z_{\mathrm{w}} - z$ gives the distance from the position of the window (z_{w}) to the position of interest (z). From Beer's Law,

$$I_{\mathrm{n}}(z,t) = I_{\mathrm{n,w}} 10^{-[z_{\mathrm{w}}t - z]h_a^{-1}} \tag{B.3}$$

where $I_{\mathrm{n,w}} = I_{\mathrm{n}}(z_{\mathrm{w}})$ is the incident intensity and h_{a} is the resin absorbance height (the inverse of the absorption coefficient). Movement of the build platform is included via the print speed. Since the coordinate system is defined with respect to the build platform, the print speed s is represented in terms of the ever-increasing value of $z_{\mathrm{w}}(t)$:

$$s = \frac{dz_{\mathrm{w}}}{dt} \tag{B.4}$$

Substituting Equation (B.4) and (B.3) into Equation (B.2),

$$\frac{d}{dz_{\mathrm{w}}}D_{\mathrm{n}}(z, z_{\mathrm{w}}) = \frac{I_{\mathrm{n,w}}}{s} 10^{-[z\mathrm{w}(t) - z]h_{\mathrm{a}}^{-1}} \tag{B.5}$$

To calculate the dose contribution from slice n, Equation (B.5) is integrated with respect to z_{w}. The limits of integration are the values of z_{w} when slice n is first projected and when the next slice, $n+1$, is projected: nh_{s} and $(n+1)h_{\mathrm{s}}$, respectively, where h_{s} is the slicing height. Thus,

$$D_{\mathrm{n}}(z) = \int_{nh_{\mathrm{s}}}^{(n+1)h_{\mathrm{s}}} \frac{I_{\mathrm{n,w}}}{s} 10^{-[z\mathrm{w}(t) - z]h_{\mathrm{a}}^{-1}} = \frac{I_{\mathrm{n,w}} h_{\mathrm{a}}}{s \ln 10} \left(10^{-(nh_{\mathrm{s}} - z)h_{\mathrm{a}}^{-1}} - 10^{-((n+1)h_{\mathrm{s}} - z)h_{\mathrm{a}}^{-1}} \right) \tag{B.6}$$

If the cross-section at height z is exposed to slice n (i.e., $z \leq nh_\mathrm{s}$), Equation B.6 gives the contribution of slice n to the total dose at that point. If the cross-section is not exposed to slice n (i.e., $z \geq (n+1)h_\mathrm{s}$), the dose contribution is zero. As a simplification, we will consider only values of z which are multiples of h_s (i.e., z-values of simulated slices). For a treatment of all real values of z, see Appendix B.2 below. Note that this model implicitly assumes that a packet of resin tends to stay in the same (x, y, z)-position as the print progresses.

Combining Equation B.1 and B.6,

$$D_\mathrm{T}(z) = \sum_{n=0}^{N} \frac{I_\mathrm{n,w} h_\mathrm{a}}{s\ln 10} \left(10^{-(nh_\mathrm{s}-z)h_\mathrm{a}^{-1}} - 10^{-((n+1)h_\mathrm{s}-z)h_\mathrm{a}^{-1}}\right) \tag{B.7}$$

Equation B.7 allows calculation of the total accumulated dose at any point in the final printed part. For convenience we may define several dimensionless variables. The dimensionless dose, Ω, is normalized by the critical dose, D_c:

$$\Omega_\mathrm{n} \equiv \frac{D_\mathrm{n}}{D_\mathrm{c}}$$

The critical dose is experimentally determined for each resin formulation and is related to the dose at which the resin becomes insoluble in the rinse solvent, IPA (i.e., reaches the gelation point). A resin packet with $\Omega_T < 1$ is considered uncured, while resin with $\Omega_T \geq 1$ is considered cured. The dimensionless light intensity at the window, Φ, is normalized by a critical intensity; I_c is the minimum intensity at which it is possible to reach D_c for h_a and s (for additional discussion, see Appendix B.2 below).

$$\Phi_\mathrm{n} \equiv \frac{I_\mathrm{n,w}}{I_\mathrm{c}} = \frac{I_\mathrm{n,w} h_\mathrm{a}}{D_\mathrm{c} s \ln 10}$$

The dimensionless z-position, ζ, is normalized by the slice height:

$$\zeta \equiv \frac{z}{h_\mathrm{s}}$$

Table B.1: Total dose by layer (from Equation B.9)

ζ	$\Omega_T(\zeta)$
N	$\Phi_{\mathrm{N}}(1-10^{-\eta})$
$N-1$	$\Phi_{\mathrm{N\text{-}1}}(1-10^{-\eta})+\Omega_T(N)10^{-\eta}$
...	...
0	$\Phi_0(1-10^{-\eta})+\Omega_T(N)10^{-\eta}$

With this normalization, slice n is first projected when $\zeta_{\mathrm{w}} = n$. Finally, the dimensionless constant η is the ratio of the slicing height to the absorbance height:

$$\eta \equiv \frac{h_{\mathrm{s}}}{h_{\mathrm{a}}}$$

Rewriting Equation B.7 in dimensionless terms,

$$\Omega_{\mathrm{T}}(\zeta) = \sum_{n=\zeta}^{N} \Phi_{\mathrm{n}} \left(10^{-(n-\zeta)\eta} - 10^{-[(n+1)-\zeta]\eta}\right) \tag{B.8}$$

This can be simplified such that $\Omega_{\mathrm{T}}(\zeta)$ is a function of $\Omega_{\mathrm{T}}(\zeta+1)$:

$$\Omega_{\mathrm{T}}(\zeta) = \Phi_{\zeta}(1-10^{-}\eta) + \Omega(\zeta+1)10^{-\eta} \tag{B.9}$$

In Equation B.9, we find the relationship that will allow quick dose calculation and slice correction. Starting at the end of the part (i.e., $\zeta = N$), we may calculate the total dose in each layer sequentially by considering only the current layer and the preceding layer. Table B.1 gives expressions for Ω_{T} at several values of ζ.

B.2 Effect of Finite Contrast Ratio

A deeper examination of behavior while black pixels are projected will highlight the significance of the projector contrast ratio. The contrast ratio of a display system is defined as the ratio of intensities for white and black; this is a finite quantity since pure black (i.e., an irradiance of zero) is unachievable. Consider a point ζ in the part

envelope with a corresponding grayscale pixel value—that is, the pixel value for slice $n = \zeta$—is zero. From Equation B.9, the total dose at this position depends on the minimum intensity and the total dose of the layer below:

$$\Omega_{\mathrm{T}}(\zeta) = \Phi_{\min}(1 - 10^{-\eta}) + \Omega_{\mathrm{T}}(\zeta + 1)10^{-\eta}$$

When the dose contribution from the minimum intensity matches the exponential decay from the dose at $\zeta + 1$, a constant dose is maintained:

$$\Omega_{\min}(\zeta) = \Phi_{\min}(1 - 10^{-\eta}) + \Omega_{\min}10^{-\eta} = \Phi_{\min}$$

This dose, $\Omega_{\min}$, acts as an effective minimum dose: if $\Omega_{\mathrm{T}} \geq \Omega_{\min}$ at position (x_0, y_0, z_0), then $\Omega_{\mathrm{T}} \geq \Omega_{\min}$ for all points $(x_0, y_0, z \leq z_0)$. The minimum dose is determined by the resin properties and the print speed as well as the contrast ratio of the projection system. For our printer, we have measured a minimum intensity of 1 mW cm^{-2}, resulting in a minimum dose of approximately 5 mJ cm^{-2} (varying with other parameters).

B.3 Equations for Target Dose Region Constraints

In a region of constant-intensity exposure, the dose at any point can be calculated if the dose at one point is known. If ζ_0 and Ω_0 are the known position and dose and Φ_0 is the constant intensity,

$$\Omega(\zeta) = \Omega_0 10^{-(\zeta_0 - \zeta)\eta} + \Phi_0 \left(1 - 10^{-(\zeta_0 - \zeta)\eta}\right) \tag{B.10}$$

For the constraint curves defining target dose regions, each curve has a constant intensity exposure ($\Phi_{\max}$ for constraint (ii) and $\Phi_{\min}$ for constraint (iii)), and the dose at the top and bottom edges are known (Ω_{c}). If the upper and lower edges of the feature are located at ζ_{U} and ζ_{L} (see Figure B.1),

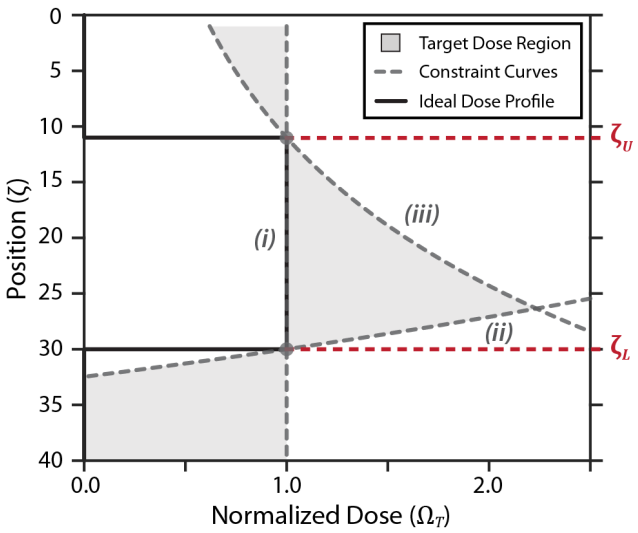

Figure B.1: Dose constraint curves (i)–(iii) and target dose region. ζ_{U} and ζ_{L} are the positions of the top and bottom of the feature, respectively.

$$\Omega_{\mathrm{ii}}(\zeta) = \Omega_c 10^{-(\zeta_{\mathrm{L}}-\zeta)\eta} + \Phi_{\max}\left(1 - 10^{-(\zeta_{\mathrm{L}}-\zeta)\eta}\right) \tag{B.11}$$

$$\Omega_{\mathrm{iii}}(\zeta) = \Omega_c 10^{-(\zeta_{\mathrm{U}}-\zeta)\eta} + \Phi_{\min}\left(1 - 10^{-(\zeta_{\mathrm{U}}-\zeta)\eta}\right) \tag{B.12}$$

The constraint curves, and thus the target dose region, are dependent on several system parameters. The relative effect of a change in each parameter is shown below in Figure B.2. In Figure 3.3, we compare dose profiles with varying maximum doses; however, the chosen maximum dose may not be reached for some features. As is evident from Figure B.2, several factors determine the shape of the target dose region for a feature. While most parameters are constant throughout the print ($I_{\max}$, s, and h_{a}), the feature size may vary considerably. For a constant set of system parameters, each feature has a maximum achievable $\Omega_{\max}$ as a function of its height. To determine this value, Equations B.11 and B.12 are first equated to determine the point at which the curves meet.

$$\zeta^* = \frac{1}{\eta}\log_{10}\left[\frac{\Phi_{\max} - \Phi_{\min}}{(\Omega_{\mathrm{c}} - \Phi_{\min})10^{-\zeta_{\mathrm{U}}\eta} - (\Omega_{\mathrm{c}} - \Phi_{\max})10^{-\zeta_{\mathrm{L}}\eta}}\right] \tag{B.13}$$

Using Equation B.13, we can write the maximum dose (assuming the edges are at the critical dose) as a function of feature height:

$$\delta \equiv \zeta_{\mathrm{L}} - \zeta_{\mathrm{U}}$$

$$\zeta^* = \frac{1}{\eta}\log_{10}\left[\frac{\Phi_{\max} - \Phi_{\min}}{(\Omega_{\mathrm{c}} - \Phi_{\min})10^{-\zeta_{\mathrm{U}}\eta} - (\Omega_{\mathrm{c}} - \Phi_{\max})10^{-(\zeta_{\mathrm{U}}+\delta)\eta}}\right]$$

$$\zeta^* = \frac{1}{\eta}\log_{10}\left[\frac{\Phi_{\max} - \Phi_{\min}}{(\Omega_{\mathrm{c}} - \Phi_{\min})10^{-\zeta_{\mathrm{U}}\eta} - (\Omega_{\mathrm{c}} - \Phi_{\max})10^{-\delta\eta}}\frac{1}{10^{-\zeta_{\mathrm{U}}\eta}}\right]$$

$$\zeta^* = \frac{1}{\eta}\log_{10}\left[\frac{\Phi_{\max} - \Phi_{\min}}{(\Omega_{\mathrm{c}} - \Phi_{\min})10^{-\zeta_{\mathrm{U}}\eta} - (\Omega_{\mathrm{c}} - \Phi_{\max})10^{-\delta\eta}}\right] - \frac{1}{\eta}\log_{10}(10^{-\zeta_{\mathrm{U}}\eta})$$

$$\zeta^* = \frac{1}{\eta}\log_{10}\left[\frac{\Phi_{\max} - \Phi_{\min}}{(\Omega_{\mathrm{c}} - \Phi_{\min})10^{-\zeta_{\mathrm{U}}\eta} - (\Omega_{\mathrm{c}} - \Phi_{\max})10^{-\delta\eta}}\right] + \zeta_{\mathrm{U}} \tag{B.14}$$

Substituting Equation B.14 into Equation B.12,

$$\Omega^* \equiv \Omega(\zeta^*) = \frac{(\Omega_{\mathrm{c}} - \Phi_{\min})(\Phi_{\max} - \Phi_{\min})}{(\Omega_{\mathrm{c}} - \Phi_{\min}) - (\Omega_{\mathrm{c}} - \Phi_{\max})10^{-\delta\eta}} + \Phi_{\min} \tag{B.15}$$

Figure B.3 shows Ω^* as a function of feature height.

B.4 Optimizing D_{c} and $\Omega_{\max}$

Effective slice correction requires that correction parameters are optimized for the resin being used. Figure B.4 illustrates two limits on the maximum achievable dose for printing with Resin 1 at 750 mm h^{-1}; these limits exist independently from the chosen value of $\Omega_{\max}$. As discussed in Appendix B.3, an infinitely long exposure at ϕ asymptotically approaches the dose $\Omega_\infty(\Phi)$. Thus, the maximum intensity defines a maximum possible dose in the model: $\Omega_\infty(\Phi_{\max}) = \Phi_{\max}$. Figure B.4(a) shows the distance that must be exposed at the maximum intensity before the critical dose is reached. This relationship suggests than certain feature-dense geometries may not be amenable to correction with these print settings; however, slower print speeds or higher light intensities may be used to compress the curve downward (for a constant exposure height, $D \propto Is^{-1}$).

For individual features, the maximum dose is the lesser of the prescribed $\Omega_{\max}$ and Ω^* as defined in Appendix B.3. Analogous to Figure B.3, Figure B.4(b) shows D^*/D_{gel} as a function of feature height for Resin 1 at 750 mm h^{-1} and several values of D_{c}.

In addition to optimizing the critical dose parameter D_{c}, we also conducted experiments investigating the effect of the maximum dose parameter $\Omega_{\max}$, with results shown in Figure B.5. Setting higher values of $D_{\max}$ makes the fidelity less sensitive to feature size, though the effect is minor. Based on this result and the desire to maximize green strength, we chose to operate the correction with an unconstrained maximum dose ($\Omega_{\max} = \infty$).

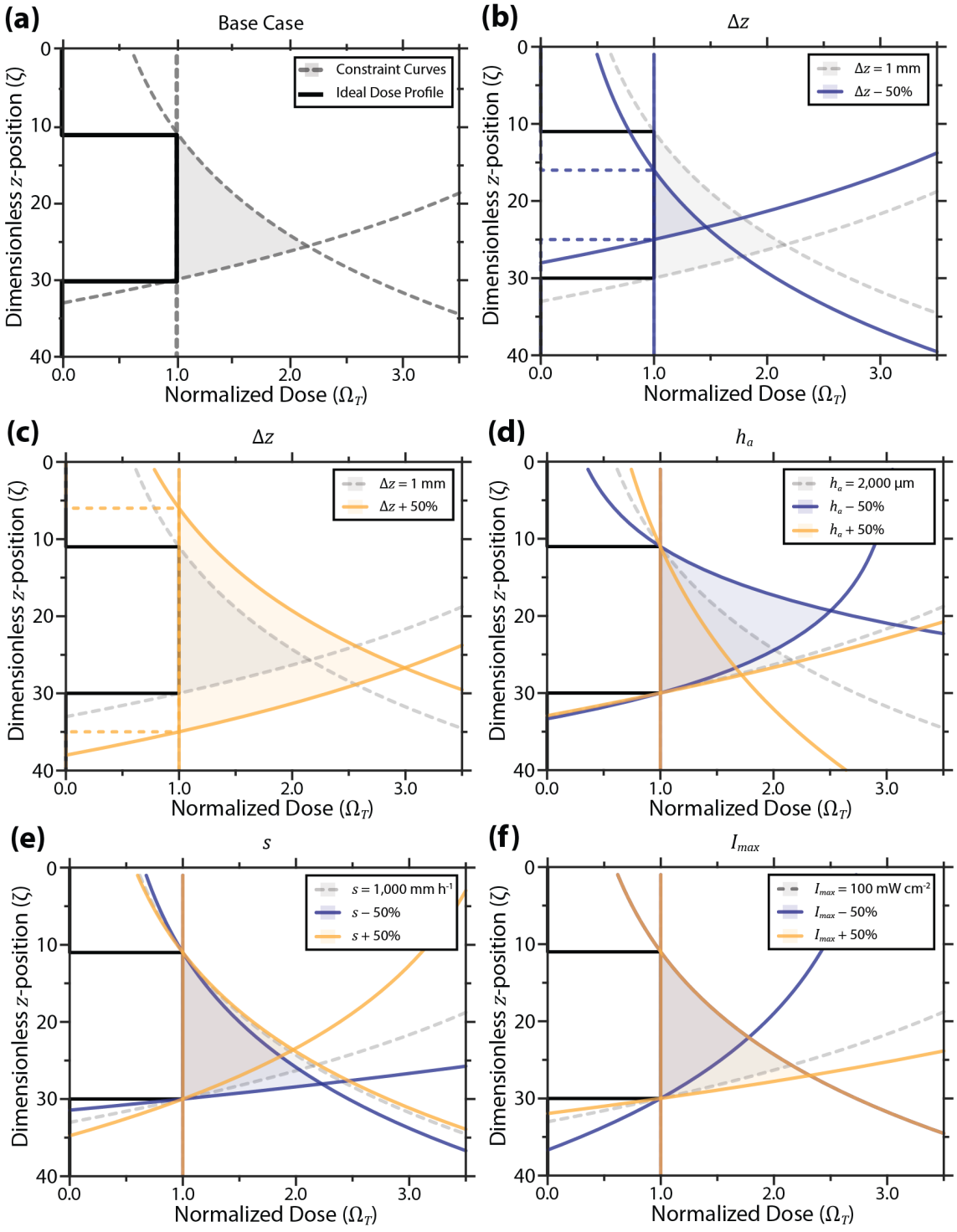

Figure B.2: Effect of increasing (yellow curves) and decreasing (blue curves) parameters by 50%: (a) Base case. $h_s = 50$ μm, $\Delta z = 1$ mm, $h_a = 2,000$ μm, $s = 1,000$ mm h^{-1}, and $I_{max} = 100$ mW cm^{-2}. (b) Decreasing feature height. (c) Increasing feature height. (d) Varying absorbance height. (e) Varying print speed. From Equation B.1, varying the critical dose has an identical effect. (f) Varying the maximum projector intensity.

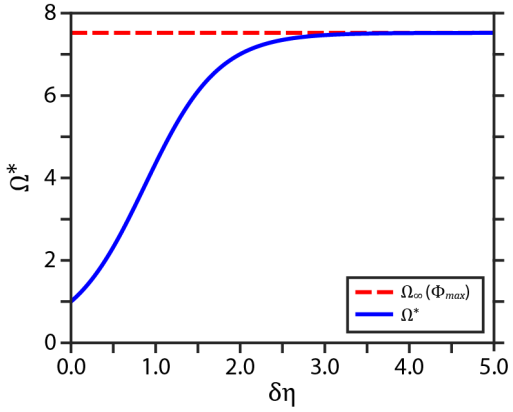

Figure B.3: Maximum dose as a function of $\delta\eta = (z_{\mathrm{L}} - z_{\mathrm{U}})h_{\mathrm{a}}^{-1}$. As the feature height increases, the maximum dose approaches the limit Ω_∞ described in Appendix B.3. Parameters: $h_{\mathrm{s}} = 50$ μm, $h_{\mathrm{a}} = 2,000$ μm, $s = 1,000$ mm h^{-1}, $I_{\max} = 120$ mW cm^{-2}, $I_{\min} = 2$ mW cm^{-2}.

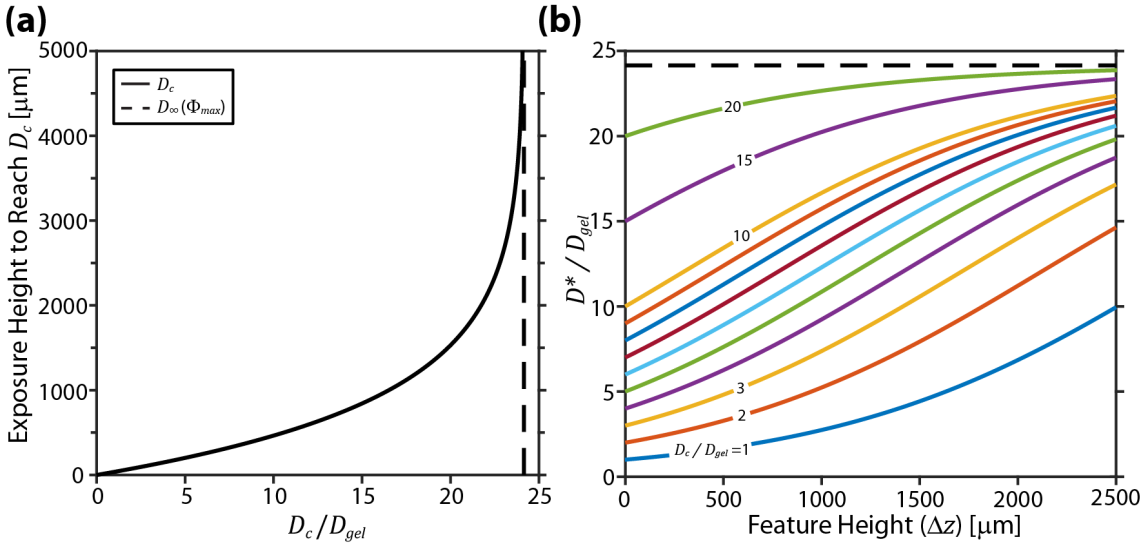

Figure B.4: Maximum dose limits for our presented optimization (Resin 1, $s = 750$ mm h^{-1} , $I_{\max} \approx 75$ mW cm^{-2}). a) Exposure height to reach the critical dose starting from zero dose. Printing at a constant speed, larger height ranges must be exposed to reach higher doses. b) The maximum possible dose for a feature of a given height, as determined by the dose constraint equations (Eq. B.15) in Appendix B.3). When the correction is applied, the maximum dose within a feature is the minimum of D^* and the chosen $D_{\max}$.

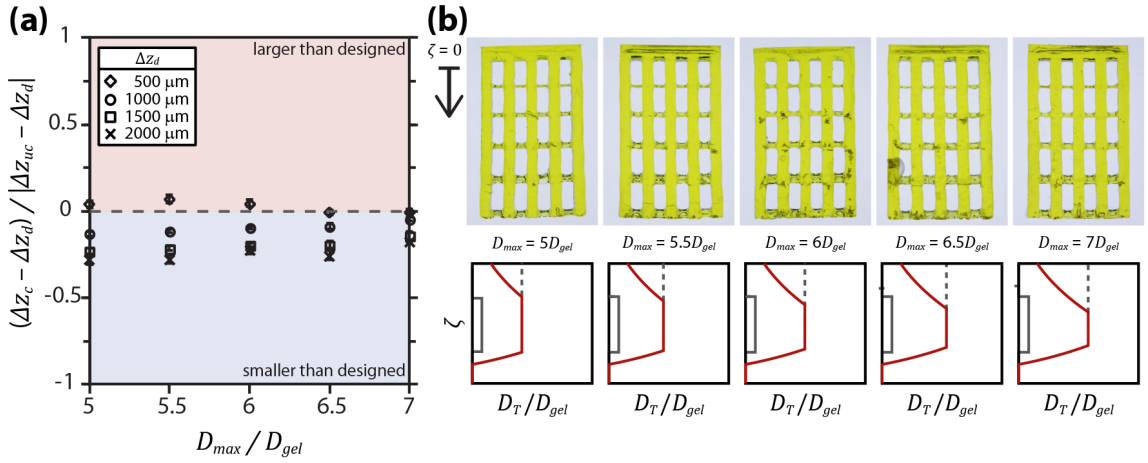

Figure B.5: Varying $D_{\max}$ with $D_c = 5D_{gel}$. a) Ratio of height errors (corrected-to-uncorrected) for a range of feature sizes and values of $D_{\max}$. A ratio of zero corresponds to a perfectly corrected feature. Error bars indicate standard error. b) Parts printed at 750 mm h^{-1} using slices corrected with $D_c = 5D_{gel}$ and different values for $D_{\max}$.

APPENDIX C

Dual-Wavelength Fabrication of Multilayered Microfluidic Devices

C.1 Calibration Data for Blue and UV Intensities

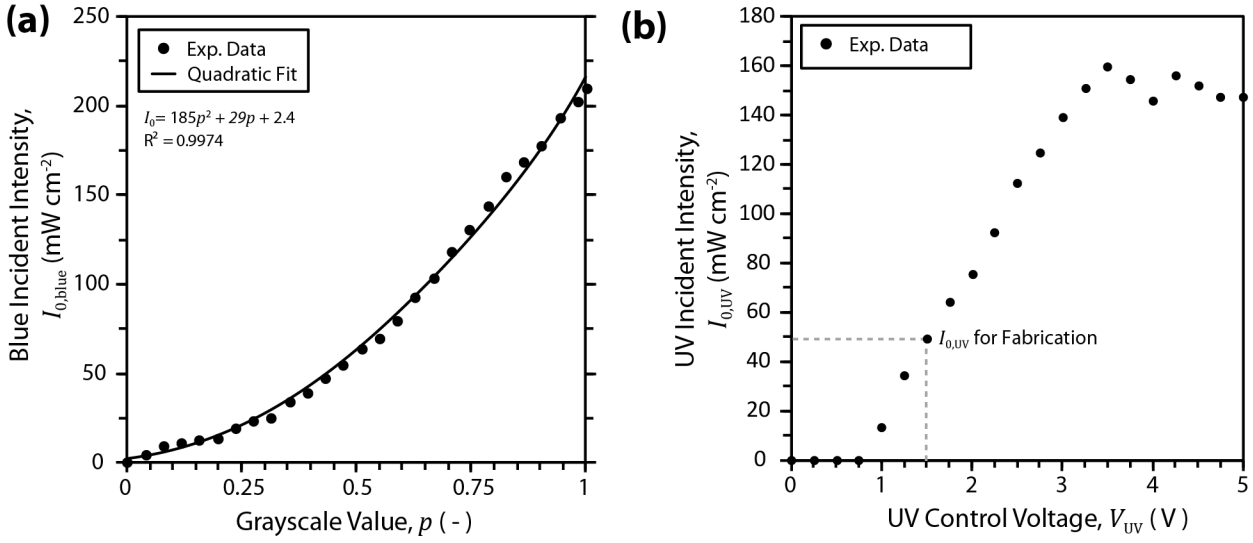

Figure C.1: Calibration data for blue and UV intensities measured at the front edge of the liquid resin for experimental setup shown in 4.2. It is important to once again note that pixel-level $I_{0,\mathrm{blue}}$ control is possible through grayscale PWM modulation of the DMD mirrors but pixel-level control of $I_{0,\mathrm{UV}}$ is not possible in the current system (a) Incident blue intensity, $I_{0,\mathrm{blue}}$, versus grayscale value, p. The grayscale value for a given pixel is defined as the [R,G,B]/255 where R=G=B. (b) Incident UV intensity, $I_{0,\mathrm{UV}}$, versus analog control voltage, V_{UV}.

C.2 Derivation of Unsteady State Dose Model

C.2.1 Blue-only exposure

For blue light exposure with no UV, there is no inhibition. The following simplified reaction scheme is used:

photolysis	$\mathrm{PI} \xrightarrow{h\nu} \mathrm{R}^\bullet$
chain initiation	$\mathrm{R}^\bullet + \mathrm{M} \longrightarrow \mathrm{RM}^\bullet$
chain propagation	$\mathrm{RM}_n^\bullet + \mathrm{M} \xrightarrow{k_p} \mathrm{RM}_{n+1}^\bullet$
chain termination	$\mathrm{RM}_n^\bullet + \mathrm{RM}_m^\bullet \xrightarrow{k_t} \mathrm{RM}_n\mathrm{M}_m$

The rate of initiator photolysis is proportional to the rate of photon absorption:

$$r_a = -\varphi \frac{\partial I(z)}{\partial z}$$

where φ is the quantum yield and $I(z)$ is the light intensity as a function of depth into the resin. From Beer's Law,

$$\frac{\partial I(z)}{\partial z} = -\frac{I(z)}{h_b}$$

$$I(z) = I_b e^{-z/h_b}$$

where $h_b \equiv (\varepsilon[\mathrm{PI}])^{-1}$ and I_b is the light intensity at the window. Thus,

$$r_a = \varphi h_b^{-1} I_b e^{-z/h_b} \tag{C.1}$$

In this model, all radicals are lumped into a single term, $\mathrm{X}^\bullet$. Since chain initiation and chain propagation result in no net generation or consumption of radicals, Equation C.1 gives the rate of radical generation.

Under the steady state approximation, there is assumed to be no net accumulation of radicals. That is, radical generation is matched by radical consumption:

$$r_c = r_a$$

Radical consumption occurs only in the termination step. Thus,

$$r_c = 2k_t[\mathrm{X}^\bullet]^2$$

$$2k_t[\mathrm{X}^\bullet]^2 = r_a$$

$$[\mathrm{X}^\bullet] = \left(\frac{r_a}{2k_t}\right)^{1/2} = \left(\frac{\varphi I_b e^{-z/h_b}}{2k_t h_b}\right)^{1/2} \tag{C.2}$$

which gives the steady-state concentration of radicals while the resin is exposed to blue light.

Our ultimate aim is to derive a relationship between degree of curing and energy input (i.e., exposure at intensity $I_{\mathrm{blue},0}$ over time period t). The threshold for curing is generally set at the gelation point, which is assumed to occur at a certain double-bond conversion. $\xi \equiv [\mathrm{M}]/[\mathrm{M}_0]$ gives the fraction of double bonds which remain unreacted and can be written from the rate of chain propagation.

$$\frac{\partial[\mathrm{M}]}{\partial t} = -k_p[\mathrm{X}^\bullet][\mathrm{M}]$$

$$\frac{\partial \xi}{\partial t} = -k_p[\mathrm{X}^\bullet]\xi$$

Substituting from Equation C.2,

$$\frac{\partial \xi}{\partial t} = -k_p \left(\frac{\varphi I_b e^{-z/h_b}}{2k_t h_b}\right)^{1/2} \xi$$

Rearranging and solving. The dose analogue $D' \equiv -\ln\xi/K$ can be defined with units $(\mathrm{mW\ cm^{-2}})^{1/2}\mathrm{s}$.

$$K \equiv k_p \left(\frac{\varphi}{2k_t h_b}\right)^{1/2}$$

$$\frac{\partial \xi}{\partial t} = -K\left(I_b e^{-z/h_b}\right)^{1/2} \xi$$

$$\xi = \exp\left[-K\left(I_b e^{-z/h_b}\right)^{1/2} t\right]$$

$$D' \equiv -\frac{\ln \xi}{K} = \left(I_b e^{-z/h_b}\right)^{1/2} t$$

$$D' = [I_b(z)]^{1/2} t \tag{C.3}$$

With Equation C.3, we have an analogue to the standard dose equation $D = I(z)\, t$.

For cure depth experiments, resin is exposed at a constant intensity for varying times. Measuring the depth to which the resin has cured allows fitting of the parameters h_b and D'_c. Assuming that the gelation point occurs at some critical double-bond conversion and solving for the cure depth,

$$\begin{aligned} D'_c &= \left(I_b e^{-z_c/h_b}\right)^{1/2} t \\ e^{-z_c/h_b} &= \frac{D'^2_c}{I_b t^2} \\ z_c &= 2h_b \ln\left(\frac{I_b^{1/2} t}{D'_c}\right) \end{aligned} \tag{C.4}$$

Equation (C.4) can be linearized to simplify fitting of h_b and D'_c:

$$z_c = 2h_b \ln\left(I_b^{1/2} t\right) - 2h_b \ln D'_c \tag{C.5}$$

A linear fit of z_c vs. $\ln\left(I_b^{1/2} t\right)$ data thus has a slope of $2h_b$ and a y-intercept of $-2h_b \ln D'_c$.

C.2.2 Blue and UV exposure

Under concurrent exposure from blue and UV light, inhibitor photolysis and chain inhibition are added to the reaction scheme.

initiator photolysis	$\mathrm{PI} \xrightarrow{h\nu} \mathrm{R}^\bullet$
inhibitor photolysis	$\mathrm{PZ} \xrightarrow{h\nu} \mathrm{Z}^\bullet$
chain initiation	$\mathrm{R}^\bullet + \mathrm{M} \longrightarrow \mathrm{RM}^\bullet$
chain propagation	$\mathrm{RM}_n^\bullet + \mathrm{M} \xrightarrow{k_p} \mathrm{RM}_{n+1}^\bullet$
chain termination	$\mathrm{RM}_n^\bullet + \mathrm{RM}_m^\bullet \xrightarrow{k_t} \mathrm{RM}_n\mathrm{M}_m$
chain inhibition	$\mathrm{RM}_n^\bullet + \mathrm{Z}^\bullet \xrightarrow{k_z} \mathrm{RM}_n\mathrm{Z}$

The dual wavelength derivation will follow the same pattern as the blue-only derivation above. Beginning with radical and inhibitor generation,

$$r_{a\mathrm{X}} = \varphi_b h_b^{-1} I_b e^{-z/h_b}$$

$$r_{a\mathrm{Z}} = \varphi_{uv} h_{uv}^{-1} I_{uv} e^{-z/h_{uv}}$$

The steady state approximation is applied to both $\mathrm{X}^\bullet$ and $\mathrm{Z}^\bullet$.

$$r_{a\mathrm{X}} = 2k_t[\mathrm{X}^\bullet]^2 + k_z[\mathrm{X}^\bullet][\mathrm{Z}^\bullet]$$

$$r_{a\mathrm{Z}} = k_z[\mathrm{X}^\bullet][\mathrm{Z}^\bullet]$$

Subtracting and solving for $[\mathrm{X}^\bullet]$,

$$r_{a\mathrm{X}} - r_{a\mathrm{Z}} = 2k_t[\mathrm{X}^\bullet]^2$$

$$\begin{aligned}[\mathrm{X}^\bullet] &= \left(\frac{r_{a\mathrm{X}} - r_{a\mathrm{Z}}}{2k_t}\right)^{1/2} \\ &= \left(\frac{\varphi_b h_b^{-1} I_b e^{-z/h_b} - \varphi_{uv} h_{uv}^{-1} I_{uv} e^{-z/h_{uv}}}{2k_t}\right)^{1/2}\end{aligned}$$

As above, we will solve the differential equation for $\xi \equiv [\mathrm{M}]/[\mathrm{M}_0]$ and define a dose analogue.

$$\frac{\partial \xi}{\partial t} = -k_p[\mathrm{X}^\bullet]\xi$$

$$\frac{\partial \xi}{\partial t} = -k_p\left(\frac{\varphi_b h_b^{-1} I_b e^{-z/h_b} - \varphi_{uv} h_{uv}^{-1} I_{uv} e^{-z/h_{uv}}}{2k_t}\right)^{1/2} \xi$$

$$K \equiv k_p\left(\frac{\varphi_b}{2k_t h_b}\right)^{1/2} \qquad \beta \equiv \frac{\varphi_{uv} h_{uv}^{-1}}{\varphi_b h_b^{-1}}$$

$$\frac{\partial \xi}{\partial t} = -K\left(I_b e^{-z/h_b} - \beta I_{uv} e^{-z/h_{uv}}\right)^{1/2} \xi$$

$$\xi = \exp\left[-K\left(I_b e^{-z/h_b} - \beta I_{uv} e^{-z/h_{uv}}\right)^{1/2} t\right]$$

$$D' \equiv -\frac{\ln \xi}{K} = \left(I_b e^{-z/h_b} - \beta I_{uv} e^{-z/h_{uv}}\right)^{1/2} t$$

$$D' = \left[I_b(z) - \beta I_{uv}(z)\right]^{1/2} t \tag{C.6}$$

D' again has units of $(\mathrm{mW\ cm^{-2}})^{1/2}\mathrm{s}$.

C.3 Effect of Exposure Time on Dead Zone Thickness

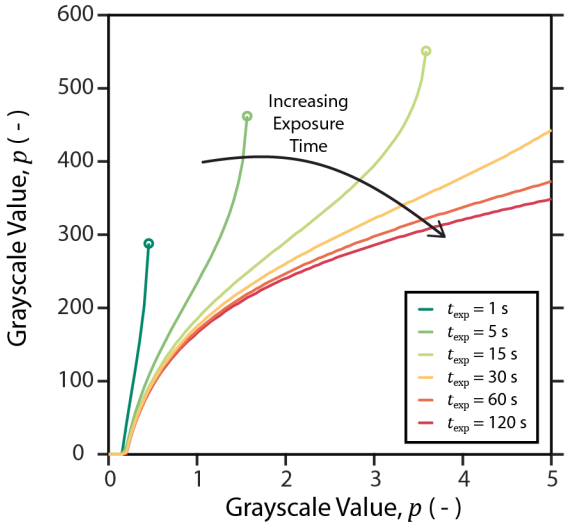

Figure C.2: Dead zone height versus $I_{0,\text{blue}}/I_{0,\text{UV}}$ (where $I_{0,\text{UV}}$ is maintained constant and $I_{0,\text{blue}}$ is varied) plotted for different exposure times. The presence of a *dead zone* is predicated by the gelation of material at some point beyond the *dead zone*, therefore for a given exposure time as $I_{0,\text{blue}}/I_{0,\text{UV}}$ increases (i.e. $I_{0,\text{blue}}$ decreases) there comes a point beyond which no material is gelled and no dead zone appears, the position of this point logically moves to higher $I_{0,\text{blue}}/I_{0,\text{UV}}$ as the exposure time increases. As $t \to \infty$ the unsteady state model tends to the previously described steady state case.

C.4 Reactive Diluent Characterization

Table C.1: Comparison of reactive diluent curing dose and inhibition coefficient

Diluent	Curing Dose, D_c (mJ/cm^2)	Inhibition Coefficient, β (-)
Trimethylolpropane Triacrylate (TMPTA)	70	4
1,6-Hexanediol diacrylate (HDDA)	138	25
Isobornyl acrylate (IBOA)	276	42
Sartomer SC531	15900	-
Triethyleneglycol dimethacrylate (TEGDMA)	1660	10

APPENDIX D

Variable-Height Channels for Microparticle Separation and Display

D.1 Properties of Fluorescent Particles

Particle Name	Mfr. Part number	Mean (μm)	S.D. (μm)	Excitation Filter (nm)	Dichroic Cutoff (nm)	Barrier Filter (nm)
Gt anti-Ms IgG (H&L)	MFP-2070-5	2.05	0.303	590-650	660	663-738
Biotin pink	TFP-5058-5	6.201	1.153	528-553	565	590-650
Biotin yellow	TFP-7052-5	7.368	0.591	490-510	515	520-550
Fluorescent yellow	FP-3052-2	3.246	0.554	465-495	505	515-555
Fluorescent nile Red	FP-3056	3.272	0.506	528-553	565	590-650
Fluorescent sky blue	FP-3070-2	3.358	0.662	590-950	660	663-738

D.2 Pneumatic Sample Vials

(see Figure D.1)

D.3 Image Analysis

(see Figure D.2)

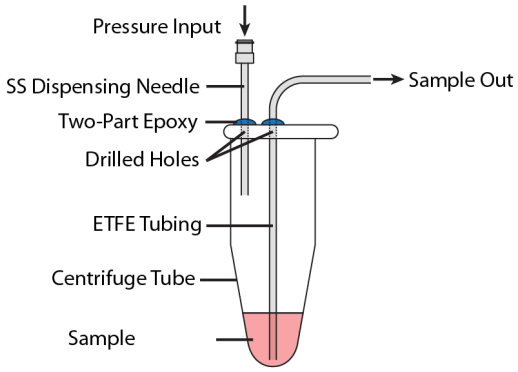

Figure D.1: Diagram of modifications to centrifuge tube for delivering sample to variable height channels. The flow rate of the sample out is controlled by adjusting the pressure input with a pressure controller.

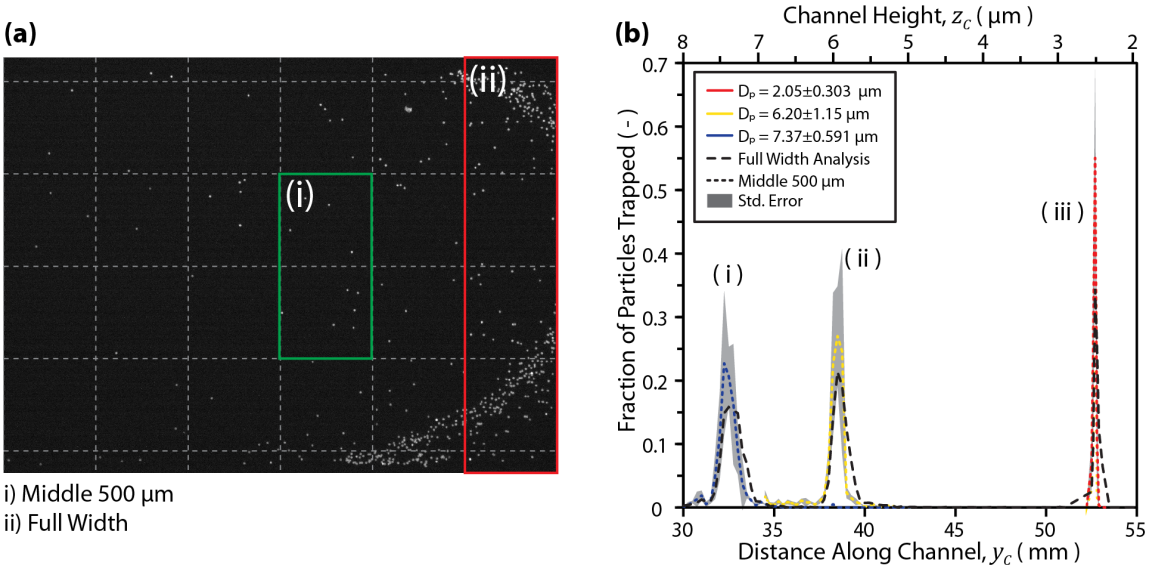

Figure D.2: Influence of image analysis on measured distribution of particles. a) Image of channel with 250 μm grid overlaid and typical areas for particle counting shown with green and red boxes. The green box encompasses the middle 500 μm of the channel and the red box the whole channel. b) The fraction of particles trapped at different positions within the channel shows is not significantly affected by the image analysis method, however particle counting with the full channel width shifts the measured distributions down the channels slightly due to the particles at the edge moving further down the channel for reasons discussed elsewhere

D.4 Derivation of Equations for Channel Height

D.4.1 Constant Velocity

The change in the height of the channel over time (i.e. the etch rate) can be defined as:

$$\frac{dz_c}{dt} = R$$

The speed of the wafer moving into the etchant can be expressed as a function of position (note this speed is negative with respect to the co-ordinate system chosen in Fig. 5.1b), with the speed being the rate of change of position over time:

$$s = \frac{dy_c}{dt} = s(y_c)$$

$$dt = \frac{-dy_c}{s(y_c)}$$

Substituting this equation into the definition of the etch rate gives an equation relating the change in the channel height to the position in the channel:

$$dz_c = \frac{-R}{s(y_c)} dy_c$$

Evaluating the indefinite integral gives the general form for the channel height for any arbitrary speed profile, $s(y_c$:

$$z_c = -R \int \frac{dy_c}{s(y_c)}$$

This equation can be used to evaluate the etching profile for any arbitrary velocity function input. For the case where the velocity is constant for the entire wafers movement into the etchant (i.e. $s(y_c) = s$):

$$z_c = -R \int \frac{dy_c}{s}$$

Evaluating the indefinite integral:

$$z_c = \frac{-R}{s} y_c + C_1$$

We define the boundary conditions for this as the channel height being zero at the final position (i.e. the wafer is not etched at any position which was not submerged in etchant solution):

$$z_{\mathrm{c}} = 0 \ @ \ y_{\mathrm{c}} = y_{\mathrm{c,f}}$$

Substituting and solving yields the equation for the channel height as a function of position along the channel:

$$z_{\mathrm{c}} = \frac{R}{s}(y_{\mathrm{c,f}} - y_{\mathrm{c}})$$

Since this equation results in negative values for $y_{\mathrm{c}} > y_{\mathrm{c,f}}$ we incorporate the unit step function such that the etch depth is always greater than or equal to zero:

$$z_{\mathrm{c}} = \frac{R}{s}(y_{\mathrm{c}} - y_{\mathrm{c,f}}\mathrm{u}(y_{\mathrm{c}} - y_{\mathrm{c,f}})$$

Taking into account the second etch step we can add the height for a conventional etching process, Rt_{etch} globally to this:

$$z_{\mathrm{c}} = \frac{R}{s}(y_{\mathrm{c}} - y_{\mathrm{c,f}}\mathrm{u}(y_{\mathrm{c}} - y_{\mathrm{c,f}}) + Rt_{\mathrm{etch}}$$

D.4.2 Non-Constant Velocity

For the case of a uniformly accelerating velocity profile, i.e. $s(y_{\mathrm{c}}) = ay_{\mathrm{c}} + s_0$. Substitution of this velocity function into the general form, integrating with the same boundary conditions (i.e. $z_{\mathrm{c}} = 0 @ y_{\mathrm{c}} = y_{\mathrm{c,f}}$), and rearranging yields:

$$z_{\mathrm{c}} = -\frac{R}{a}\log\left(\frac{ay_{\mathrm{c}} + s_0}{ay_{\mathrm{c,f}} + s_0}\right)$$

Similarly for a parabolic velocity profile, i.e. $s(y_{\mathrm{c}}) = ay_{\mathrm{c}}^2 + by_{\mathrm{c}} + s_0$, the channel height as a function of position is given by:

$$z_{\mathrm{c}} = \frac{2R}{\sqrt{4as_0 - b^2}}\left(\tan^{-1}\left(\frac{ay_{\mathrm{c}} + b}{\sqrt{4as_0 - b^2}}\right) - -\tan^{-1}\left(\frac{ay_{\mathrm{c,f}} + b}{\sqrt{4as_0 - b^2}}\right)\right)$$

D.5 Effect of Etch Parameters on Channel Profile

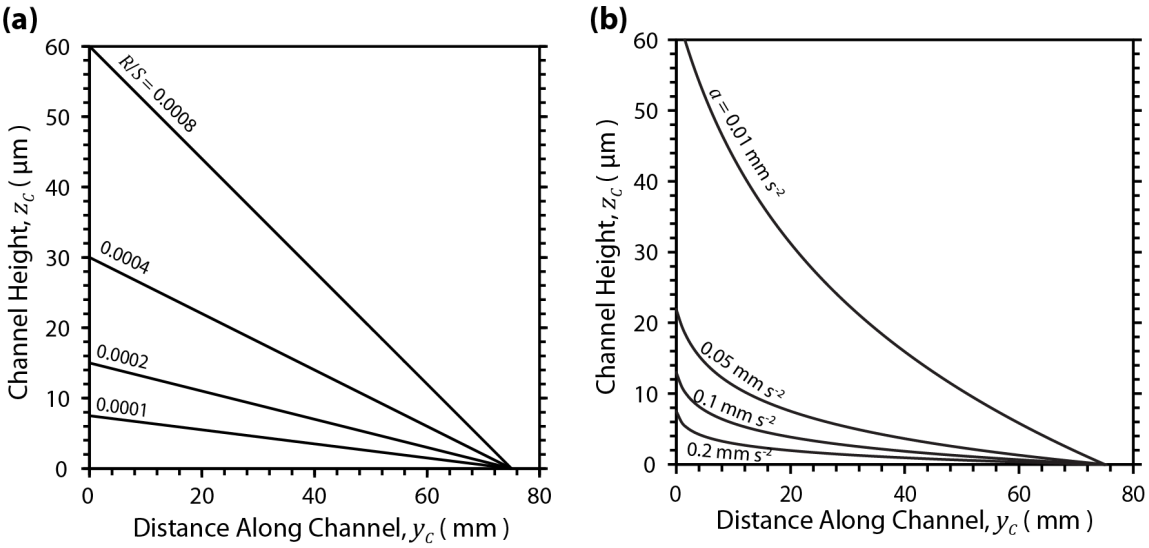

Figure D.3: Theoretical effect of fabrication parameters on the channel height. a) For wafers moving into the liquid with constant velocity, the ratio of etch rate to lowering velocity (R/s) determines the slope of the channel. Increasing R/s either by decreasing the velocity the wafer is lowered at or increasing the etch rate of the solution will result in deeper channels with higher slopes. b) Wafers which are accelerated into the etchant can obtain curved height profiles. The curvature of the height profile is dependent on the acceleration, a. As a decreases (i.e. approaches zero) the height profile tends towards the constant velocity case shown in (a).

D.6 Effect of Surface Tension on Etch Profile

(see Figure D.4)

D.7 Additional RBC Deformability on Patient Blood Samples

(see Figure D.5)

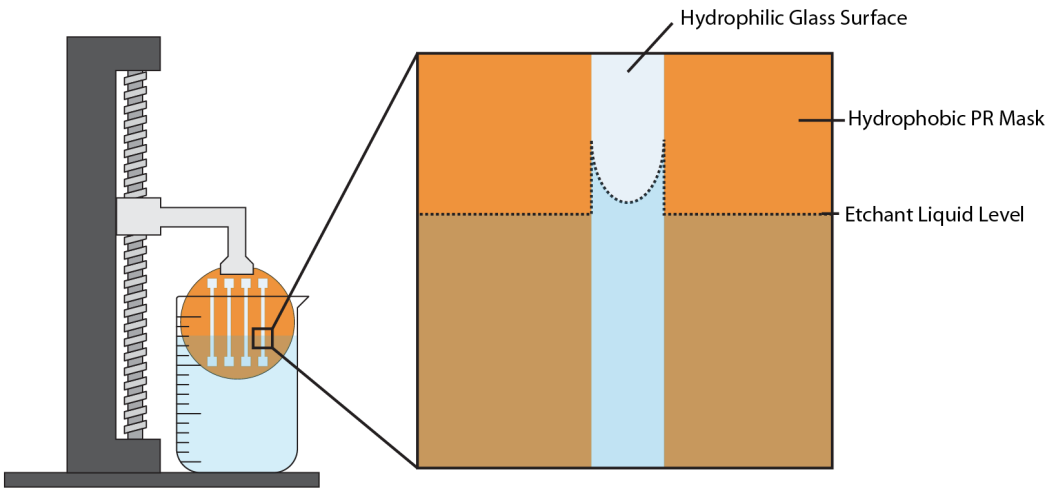

Figure D.4: Diagram highlighting the surface tension effects observed during etching. Adhesive forced between the hydrophilic glass substrate and liquid HF etchant cause the etchant to be drawn slightly upward during etching. This causes the edges of the channels to be exposed to the etchant for slightly longer, resulting in visible height variation across the width of the channel.

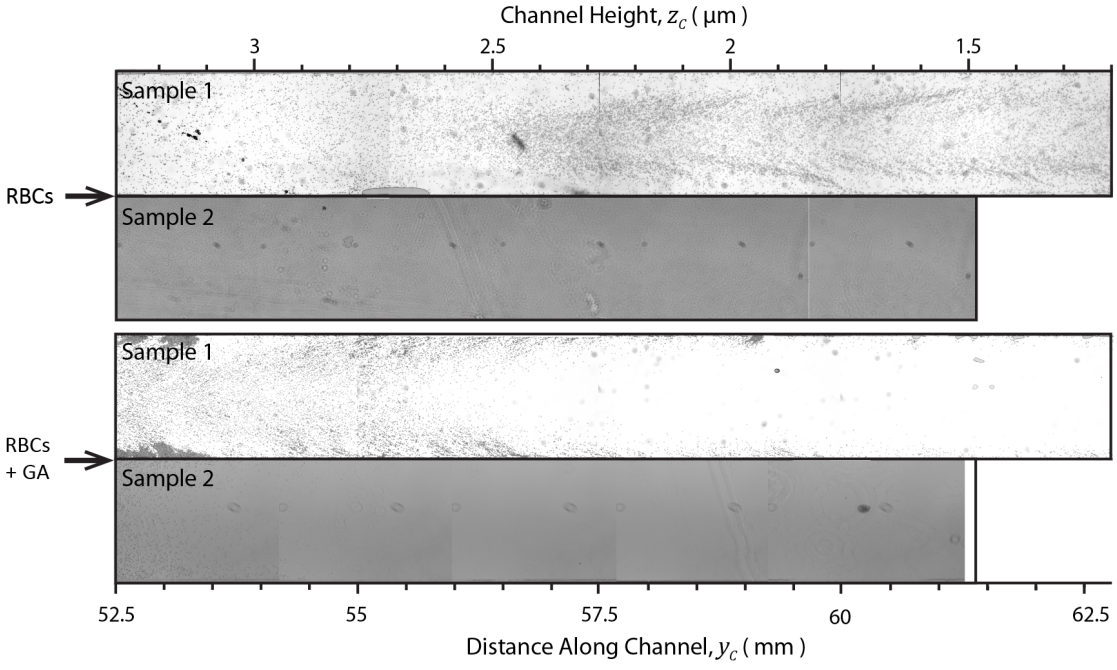

Figure D.5: Diagram highlighting the surface tension effects observed during etching. Adhesive forced between the hydrophilic glass substrate and liquid HF etchant cause the etchant to be drawn slightly upward during etching. This causes the edges of the channels to be exposed to the etchant for slightly longer, resulting in visible height variation across the width of the channel.

BIBLIOGRAPHY

BIBLIOGRAPHY

[1] #3DBenchy – The jolly 3D printing torture-test.

[2] Easter Eggs by Antonin Nosek - Thingiverse.

[3] https://reprap.org/wiki/reprap (1/21/2020).

[4] Charles W Hull. Apparatus for production of three-dimensional objects by stereolithography, 1989.

[5] A Bertsch, J Y Jézéquel, and J C André. Study of the spatial resolution of a new 3D microfabrication process: the microstereophotolithography using a dynamic mask-generator technique. *Journal of Photochemistry and Photobiology A: Chemistry*, 107(1):275–281, July 1997.

[6] C Sun, N Fang, D M Wu, and X Zhang. Projection micro-stereolithography using digital micro-mirror dynamic mask. *Sensors and Actuators A*, 121(1):113–120, May 2005.

[7] Rolando Quintana, Jae Won Choi, Karina Puebla, and Ryan Wicker. Effects of build orientation on tensile strength for stereolithography- manufactured ASTM D-638 type i specimens. *International Journal of Advanced Manufacturing Technology*, 46(1-4):201–215, January 2010.

[8] John R Tumbleston, David Shirvanyants, N. Ermoshkin, Rima Janusziewicz, Ashley R Johnson, David Kelly, Kai Chen, Robert Pinschmidt, Jason P Rolland, Alexander Ermoshkin, Edward T Samulski, and J. M. DeSimone. Continuous liquid interface production of 3D objects. *Science*, 347(6228):1349–1352, March 2015.

[9] Rima Janusziewicz, John R Tumbleston, Adam L Quintanilla, Sue J Mecham, and Joseph M DeSimone. Layerless fabrication with continuous liquid interface production. *Proceedings of the National Academy of Sciences*, 113(42):11703–11708, October 2016.

[10] David A. Walker, James L. Hedrick, and Chad A. Mirkin. Rapid, large-volume, thermally controlled 3D printing using a mobile liquid interface. *Science*, 366(6463):360–364, October 2019.

[11] Brett E. Kelly, Indrasen Bhattacharya, Hossein Heidari, Maxim Shusteff, Christopher M. Spadaccini, and Hayden K. Taylor. Volumetric additive manufacturing via tomographic reconstruction. *Science*, 363(6431):1075–1079, March 2019.

[12] Pilnam Kim, Keon Woo Kwon, Min Cheol Park, Sung Hoon Lee, Sun Min Kim, & Kahp, and Yang Suh. Soft Lithography for Microfluidics: a Review. *BioChip Journal*, 2(1):1–11, 2008.

[13] James Friend and Leslie Yeo. Fabrication of microfluidic devices using polydimethylsiloxane. *Biomicrofluidics*, 4(2), 2010.

[14] Casey C. Glick, Mitchell T. Srimongkol, Aaron J. Schwartz, William S. Zhuang, Joseph C. Lin, Roseanne H. Warren, Dennis R. Tekell, Panitan A. Satamalee, and Liwei Lin. Rapid assembly of multilayer microfluidic structures via 3D-printed transfer molding and bonding. *Microsystems and Nanoengineering*, 2, 2016.

[15] Sidra Waheed, Joan M. Cabot, Niall P. Macdonald, Trevor Lewis, Rosanne M. Guijt, Brett Paull, and Michael C. Breadmore. 3D printed microfluidic devices: Enablers and barriers, 2016.

[16] Gregor Weisgrab, Aleksandr Ovsianikov, and Pedro F. Costa. Functional 3D Printing for Microfluidic Chips. *Advanced Materials Technologies*, 4(10):1900275, October 2019.

[17] Jia Min Lee, Meng Zhang, and Wai Yee Yeong. Characterization and evaluation of 3D printed microfluidic chip for cell processing. *Microfluidics and Nanofluidics*, 20(1):1–15, January 2016.

[18] Philip J. Kitson, Mali H. Rosnes, Victor Sans, Vincenza Dragone, and Leroy Cronin. Configurable 3D-Printed millifluidic and microfluidic 'lab on a chip' reactionware devices. *Lab on a Chip*, 12(18):3267, 2012.

[19] Philip J. Kitson, Mark D. Symes, Vincenza Dragone, and Leroy Cronin. Combining 3D printing and liquid handling to produce user-friendly reactionware for chemical synthesis and purification. *Chemical Science*, 4(8):3099–3103, July 2013.

[20] Aliaa I. Shallan, Petr Smejkal, Monika Corban, Rosanne M. Guijt, and Michael C. Breadmore. Cost-effective three-dimensional printing of visibly transparent microchips within minutes. *Analytical Chemistry*, 86(6):3124–3130, March 2014.

[21] Anthony K. Au, Nirveek Bhattacharjee, Lisa F. Horowitz, Tim C. Chang, and Albert Folch. 3D-printed microfluidic automation. *Lab on a Chip*, 15(8):1934–1941, April 2015.

[22] Tobias Dahlberg, Tim Stangner, Hanqing Zhang, Krister Wiklund, Petter Lundberg, Ludvig Edman, and Magnus Andersson. 3D printed water-soluble scaffolds for rapid production of PDMS micro-fluidic flow chambers. *Scientific Reports*, 8(1), December 2018.

[23] Ho Nam Chan, Yangfan Chen, Yiwei Shu, Yin Chen, Qian Tian, and Hongkai Wu. Direct, one-step molding of 3D-printed structures for convenient fabrication of truly 3D PDMS microfluidic chips. *Microfluidics and Nanofluidics*, 19(1):9–18, July 2015.

[24] Germán Comina, Anke Suska, and Daniel Filippini. PDMS lab-on-a-chip fabrication using 3D printed templates. *Lab on a Chip*, 14(2):424–430, jan 2014.

[25] Anthony K. Au, Wonjae Lee, and Albert Folch. Mail-order microfluidics: Evaluation of stereolithography for the production of microfluidic devices. *Lab on a Chip*, 14(7):1294–1301, April 2014.

[26] Ansgar Waldbaur, Bernardo Carneiro, Paul Hettich, and Bastian E Rapp. COMPUTER AIDED MICROFLUIDICS (CAMF)-HIGH-RESOLUTION PROJECTION LITHOGRAPHY FOR THE RAPID CREATION OF LARGE-SCALE MICROFLUIDIC STRUCTURES. In *16th International Conference on Miniaturized Systems for Chemistry and Life Sciences*, 2012.

[27] Hua Gong, Bryce P. Bickham, Adam T. Woolley, and Gregory P. Nordin. Custom 3D printer and resin for 18 μm $\times$ 20 μm microfluidic flow channels. *Lab on a Chip*, 17(17):2899–2909, August 2017.

[28] Hua Gong, Michael Beauchamp, Steven Perry, Adam T. Woolley, and Gregory P. Nordin. Optical approach to resin formulation for 3D printed microfluidics. *RSC Adv.*, 5(129):3627–3637, 2015.

[29] H Lipson and M Kurman. Fabricated The New World of 3D Printing - Hod Lipson, Melba Kurman - Google Books, 2013.

[30] Samuel H Huang, Peng Liu, Abhiram Mokasdar, and Liang Hou. Additive manufacturing and its societal impact: a literature review. *The International Journal of Advanced Manufacturing Technology*, 67(5-8):1191–1203, July 2013.

[31] C Lee Ventola. Medical Applications for 3D Printing: Current and Projected Uses. *P & T : a peer-reviewed journal for formulary management*, 39(10):704–11, October 2014.

[32] Helena N Chia and Benjamin M Wu. Recent advances in 3D printing of biomaterials. *Journal of Biological Engineering*, 9, March 2015.

[33] Qingbin Liu, Ming C Leu, and Stephen M Schmitt. Rapid prototyping in dentistry: technology and application. *The International Journal of Advanced Manufacturing Technology*, 29(3-4):317–335, June 2006.

[34] Terry T Wohlers. *Wohlers report 2009: state of the industry annual worldwide progress report.* Wohlers Associates, Fort Collins, Col., 2009.

[35] Disruptive technologies: Advances that will transform life, business, and the global economy — McKinsey.

[36] Kensuke Takagishi and Shinjiro Umezu. Development of the Improving Process for the 3D Printed Structure. *Scientific Reports*, 7(1):39852, February 2017.

[37] Hu Chen, Xu Yang, Litong Chen, Yong Wang, and Yuchun Sun. Application of FDM three-dimensional printing technology in the digital manufacture of custom edentulous mandible trays. *Scientific Reports*, 6:19207, January 2016.

[38] Joseph T Belter and Aaron M Dollar. Strengthening of 3D Printed Fused Deposition Manufactured Parts Using the Fill Compositing Technique. *PLOS ONE*, 10(4):e0122915, April 2015.

[39] William E Frazier. Metal Additive Manufacturing: A Review. *Journal of Materials Engineering and Performance*, 23(6):1917–1928, June 2014.

[40] Wei Gao, Yunbo Zhang, Devarajan Ramanujan, Karthik Ramani, Yong Chen, Christopher B Williams, Charlie C L Wang, Yung C Shin, Song Zhang, and Pablo D Zavattieri. The status, challenges, and future of additive manufacturing in engineering. *Computer-Aided Design*, 69:65–89, December 2015.

[41] Wei Zhu, Kathryn R Tringale, Sarah A Woller, Shangting You, Susie Johnson, Haixu Shen, Jacob Schimelman, Michael Whitney, Joanne Steinauer, Weizhe Xu, Tony L Yaksh, Quyen T Nguyen, and Shaochen Chen. Rapid continuous 3D printing of customizable peripheral nerve guidance conduits. *Materials Today*, April 2018.

[42] J G Leprince, W M Palin, M A Hadis, J Devaux, and G Leloup. Progress in dimethacrylate-based dental composite technology and curing efficiency. *Dental materials : official publication of the Academy of Dental Materials*, 29(2):139–156, February 2013.

[43] Bruce M Monroe and Gregory C Weed. Photoinitiators for free-radical-initiated photoimaging systems. *Chemical Reviews*, 93(1):435–448, January 1993.

[44] Yihui Zhang, Fan Zhang, Zheng Yan, Qiang Ma, Xiuling Li, Yonggang Huang, and John A Rogers. Printing, folding and assembly methods for forming 3D mesostructures in advanced materials. *Nature Reviews Materials*, 2(4):17019, April 2017.

[45] Yayue Pan, Haiyang He, Jie Xu, and Alan Feinerman. Study of separation force in constrained surface projection stereolithography. *Rapid Prototyping Journal*, 23(2):353–361, March 2017.

[46] Bethany C. Gross, Jayda L. Erkal, Sarah Y. Lockwood, Chengpeng Chen, and Dana M. Spence. Evaluation of 3D printing and its potential impact on biotechnology and the chemical sciences. *Analytical Chemistry*, 86(7):3240–3253, 2014.

[47] Ji-Won Park, Gyu-Seong Shim, Jong-Ho Back, Hyun-Joong Kim, Seunghan Shin, and Taek-Sung Hwang. Characteristic shrinkage evaluation of photocurable materials. *Polymer Testing*, 56:344–353, December 2016.

[48] Xavier Allonas, Houssam Obeid, Jean-Pierre Fouassier, Makoto Kaji, Yasuhisa Ichihashi, and Yasuharu Murakami. Photochemistry and Polymerization Efficiency of Bis-imidazole based Photoinitiator Systems. *Journal of Photopolymer Science and Technology*, 16(1):123–128, 2003.

[49] T. F. Scott, B. A. Kowalski, A. C. Sullivan, C. N. Bowman, and R. R. McLeod. Two-Color Single-Photon Photoinitiation and Photoinhibition for Subdiffraction Photolithography. *Science*, 324(5929):913–917, May 2009.

[50] Fischer Joachim and Wegener Martin. Three-dimensional optical laser lithography beyond the diffraction limit. *Laser & Photonics Reviews*, 7(1):22–44, March 2012.

[51] Zongsong Gan, Yaoyu Cao, Richard A Evans, and Min Gu. Three-dimensional deep sub-diffraction optical beam lithography with 9 nm feature size. *Nature Communications*, 4:2061, June 2013.

[52] L. G. Lovell, B. J. Elliott, J. R. Brown, and C. N. Bowman. The effect of wavelength on the polymerization of multi(meth)acrylates with disulfide/benzilketal combinations. *Polymer*, 42(2):421–429, 2001.

[53] Neil D Dolinski, Zachariah A Page, E Benjamin Callaway, Fabian Eisenreich, Ronnie V Garcia, Roberto Chavez, David P Bothman, Stefan Hecht, Frank W Zok, and Craig J Hawker. Solution Mask Liquid Lithography (SMaLL) for One-Step, Multimaterial 3D Printing. *Advanced Materials*, 30(31):1800364, August 2018.

[54] Dowon Ahn, Sameer S Sathe, Brian H Clarkson, and Timothy F Scott. Hexaarylbiimidazoles as visible light thiol–ene photoinitiators. *Dental Materials*, 31(9):1075–1089, September 2015.

[55] Tuan D Ngo, Alireza Kashani, Gabriele Imbalzano, Kate T Q Nguyen, and David Hui. Additive manufacturing (3D printing): A review of materials , methods , applications and challenges. *Composites Part B*, 143:172–196, 2018.

[56] Olayinka Oderinde, Fang Yao, Hussain Imtiaz, Kewen Li, Mengmeng Kang, Guodong Fu, and Shunli Liu. Multifaceted polymeric materials in three-dimensional processing (3DP) technologies: Current progress and prospects. *Polymers for Advanced Technologies*, 29(6):1586–1602, June 2018.

[57] R. Daniel Pedde, Bahram Mirani, Ali Navaei, Tara Styan, Sarah Wong, Mehdi Mehrali, Ashish Thakur, Nima Khadem Mohtaram, Armin Bayati, Alireza Dolatshahi-Pirouz, Mehdi Nikkhah, Stephanie M. Willerth, and Mohsen Akbari. Emerging Biofabrication Strategies for Engineering Complex Tissue Constructs. *Advanced Materials*, 29(19):1606061, May 2017.

[58] Akhilesh K. Gaharwar, Lauren M. Cross, Charles W. Peak, Karli Gold, James K. Carrow, Anna Brokesh, and Kanwar Abhay Singh. 2D Nanoclay for Biomedical Applications: Regenerative Medicine, Therapeutic Delivery, and Additive Manufacturing, June 2019.

[59] Kyunghun Kim, Bongjoong Kim, and Chi Hwan Lee. Printing Flexible and Hybrid Electronics for Human Skin and Eye-Interfaced Health Monitoring Systems, July 2019.

[60] Pingqiang Cai, Zhuyun Li, Ela Sachyani Keneth, Luying Wang, Changjin Wan, Ying Jiang, Benhui Hu, Yun Long Wu, Shutao Wang, Chwee Teck Lim, Eugene V. Makeyev, Shlomo Magdassi, and Xiaodong Chen. Differential Homeostasis of Sessile and Pendant Epithelium Reconstituted in a 3D-Printed "GeminiChip". *Advanced Materials*, 31(28):1900514, July 2019.

[61] Dena Shahriari, Gabriel Loke, Ian Tafel, Seongjun Park, Po-Han Chiang, Yoel Fink, and Polina Anikeeva. Scalable Fabrication of Porous Microchannel Nerve Guidance Scaffolds with Complex Geometries. *Advanced Materials*, 31(30):1902021, July 2019.

[62] Yang Yang, Xuan Song, Xiangjia Li, Zeyu Chen, Chi Zhou, Qifa Zhou, and Yong Chen. Recent Progress in Biomimetic Additive Manufacturing Technology: From Materials to Functional Structures, September 2018.

[63] Audrey Velasco-Hogan, Jun Xu, and Marc A. Meyers. Additive Manufacturing as a Method to Design and Optimize Bioinspired Structures. *Advanced Materials*, 30(52):1800940, dec 2018.

[64] Gianluca Etienne, Irvine Lian Hao Ong, and Esther Amstad. Bioinspired Viscoelastic Capsules: Delivery Vehicles and Beyond. *Advanced Materials*, 31(27):1808233, July 2019.

[65] Rouhollah D. Farahani, Martine Dubé, and Daniel Therriault. Three-Dimensional Printing of Multifunctional Nanocomposites: Manufacturing Techniques and Applications, July 2016.

[66] Luca Hirt, Alain Reiser, Ralph Spolenak, and Tomaso Zambelli. Additive Manufacturing of Metal Structures at the Micrometer Scale, May 2017.

[67] Daxian Cao, Yingjie Xing, Karnpiwat Tantratian, Xiao Wang, Yi Ma, Alolika Mukhopadhyay, Zheng Cheng, Qing Zhang, Yucong Jiao, Lei Chen, and Hongli Zhu. 3D Printed High-Performance Lithium Metal Microbatteries Enabled by Nanocellulose. *Advanced Materials*, 31(14):1807313, April 2019.

[68] Haiyang Wang, Jinpeng Shen, Dylan J. Kline, Noah Eckman, Niti R. Agrawal, Tao Wu, Peng Wang, and Michael R. Zachariah. Direct Writing of a 90 wt% Particle Loading Nanothermite. *Advanced Materials*, 31(23):1806575, June 2019.

[69] Daryl W. Yee, Max L. Lifson, Bryce W. Edwards, and Julia R. Greer. Additive Manufacturing of 3D-Architected Multifunctional Metal Oxides. *Advanced Materials*, 31(33):1901345, August 2019.

[70] Wenji Yang, Jie Yang, Jae Jong Byun, Francis P. Moissinac, Jiaqi Xu, Sarah J. Haigh, Marco Domingos, Mark A. Bissett, Robert A.W. Dryfe, and Suelen Barg. 3D Printing of Freestanding MXene Architectures for Current-Collector-Free Supercapacitors. *Advanced Materials*, 31(37):1902725, September 2019.

[71] Nicole Kleger, Martina Cihova, Kunal Masania, André R. Studart, and Jörg F. Löffler. 3D Printing of Salt as a Template for Magnesium with Structured Porosity. *Advanced Materials*, 31(37):1903783, September 2019.

[72] Matt Ratto and Robert Ree. Materializing information: 3D printing and social change. *First Monday*, 17(7), July 2012.

[73] Martin P de Beer, Harry L van der Laan, Megan A Cole, Riley J Whelan, Mark A Burns, and Timothy F Scott. Rapid, continuous additive manufacturing by volumetric polymerization inhibition patterning. *Science Advances*, 5(1):eaau8723, January 2019.

[74] Jae-Won Choi, Ryan B Wicker, Seok-Hyun Cho, Chang-Sik Ha, and Seok-hee Lee. Cure depth control for complex 3D microstructure fabrication in dynamic mask projection microstereolithography. *Rapid Prototyping Journal*, 15(1):59–70, January 2009.

[75] Paul F O'Neill, Nigel Kent, and Dermot Brabazon. Mitigation and control of the overcuring effect in mask projection micro-stereolithography. In *AIP Conference Proceedings*, volume 200012, page 200012, 2017.

[76] Ameya Shankar Limaye and David W Rosen. Compensation zone approach to avoid print-through errors in mask projection stereolithography builds. *Rapid Prototyping Journal*, 12(5):283–291, October 2006.

[77] S. Zissi, A. Bertsch, J. Y. Jézéquel, S. Corbel, D. J. Lougnot, and J. C. André. Stereolithography and microtechniques. *Microsystem Technologies*, 2(1):97–102, March 1995.

[78] C. Sun and X. Zhang. Experimental and numerical investigations on microstereolithography of ceramics. *Journal of Applied Physics*, 92(8):4796–4802, October 2002.

[79] A. S. Limaye and D. W. Rosen. Process planning method for mask projection microstereolithography. *Rapid Prototyping Journal*, 13(2):76–84, 2007.

[80] Max J. Männel, Lukas Selzer, Ricardo Bernhardt, and Julian Thiele. Optimizing Process Parameters in Commercial Micro-Stereolithography for Forming Emulsions and Polymer Microparticles in Nonplanar Microfluidic Devices. *Advanced Materials Technologies*, 4(1):1800408, January 2019.

[81] Dhananjay Dendukuri, Priyadarshi Panda, Ramin Haghgooie, Ju Min Kim, T. Alan Hatton, and Patrick S. Doyle. Modeling of Oxygen-Inhibited Free Radical Photopolymerization in a PDMS Microfluidic Device. *Macromolecules*, 41(22):8547–8556, November 2008.

[82] Zilu Wang, Heyi Liang, and Andrey V. Dobrynin. Computer Simulations of Continuous 3-D Printing. *Macromolecules*, 50(19):7794–7800, 2017.

[83] Swarnavo Sarkar and Sheng Lin-Gibson. Computational Design of Photocured Polymers Using Stochastic Reaction-Diffusion Simulation. *Advanced Theory and Simulations*, 1(7):1800028, July 2018.

[84] Chi Zhou, Yong Chen, and Richard A Waltz. Optimized Mask Image Projection for Solid Freeform Fabrication. *Journal of Manufacturing Science and Engineering*, 131(6):1–12, December 2009.

[85] Creative Tools Sweden AB. #3DBenchy – The jolly 3D printing torture-test.

[86] Gregory I. Peterson, Johanna J. Schwartz, Di Zhang, Benjamin M. Weiss, Mark A. Ganter, Duane W. Storti, and Andrew J. Boydston. Production of Materials with Spatially-Controlled Cross-Link Density via Vat Photopolymerization. *ACS Applied Materials and Interfaces*, 8(42):29037–29043, 2016.

[87] Paul F Jacobs. Fundamentals of Stereolithography. Technical report, 3D Systems, Inc., 1992.

[88] Eric Livak-Dahl, Irene Sinn, and Mark Burns. Microfluidic Chemical Analysis Systems. *Annual Review of Chemical and Biomolecular Engineering*, 2(1):325–353, July 2011.

[89] Guansheng Du, Qun Fang, and Jaap M.J. den Toonder. Microfluidics for cell-based high throughput screening platforms-A review, January 2016.

[90] Todd A. Duncombe, Augusto M. Tentori, and Amy E. Herr. Microfluidics: Reframing biological enquiry, August 2015.

[91] Marianah Masrie, Burhanuddin Yeop Majlis, and Jumril Yunas. Fabrication of multilayer-PDMS based microfluidic device for bio-particles concentration detection. In *Bio-Medical Materials and Engineering*, volume 24, pages 1951–1958. IOS Press, 2014.

[92] Mark A. Eddings, Michael A. Johnson, and Bruce K. Gale. Determining the optimal PDMS-PDMS bonding technique for microfluidic devices. *Journal of Micromechanics and Microengineering*, 18(6), jun 2008.

[93] Eric Leclerc, Yasuyuki Sakai, and Teruo Fujii. A multi-layer PDMS microfluidic device for tissue engineering applications. In *Proceedings of the IEEE Micro Electro Mechanical Systems (MEMS)*, pages 415–418, 2003.

[94] Rolf Dessauer. The Invention of Dylux® Instant-Access Imaging Materials and the Development of HABI Chemistry-A Personal History. In *Advances in {Photochemistry}*, pages 129–261. Wiley-Blackwell, April 2005.

[95] Mohammad Atai, Mehdi Ahmadi, Samal Babanzadeh, and David C Watts. Synthesis, characterization, shrinkage and curing kinetics of a new low-shrinkage urethane dimethacrylate monomer for dental applications. *Dental materials : official publication of the Academy of Dental Materials*, 23(8):1030–41, aug 2007.

[96] Jim H. Lee, Robert K. Prud'homme, and Ilhan A. Aksay. Cure depth in photopolymerization: Experiments and theory. *Journal of Materials Research*, 16(12):3536–3544, 2001.

[97] Robin H Liu, Mark A Stremler, Kendra V Sharp, Michael G Olsen, Juan G Santiago, Ronald J Adrian, Hassan Aref, and David J Beebe. Passive Mixing in a Three-Dimensional Serpentine Microchannel. Technical Report 2, 2000.

[98] Marc A. Unger, Hou Pu Chou, Todd Thorsen, Axel Scherer, and Stephen R. Quake. Monolithic microfabricated valves and pumps by multilayer soft lithography. *Science*, 288(5463):113–116, apr 2000.

[99] Ali Asgar S Bhagat, Hansen Bow, Han Wei Hou, Swee Jin Tan, Jongyoon Han, and Chwee Teck Lim. Microfluidics for cell separation, October 2010.

[100] P Sajeesh and Ashis Kumar Sen. Particle separation and sorting in microfluidic devices: A review, 2014.

[101] Stefan Miltenyi, Werner Müller, Walter Weichel, and Andreas Radbruch. High gradient magnetic cell separation with MACS. *Cytometry*, 11(2):231–238, 1990.

[102] Xiaoming Chen, Yukun Ren, Weiyu Liu, Xiangsong Feng, Yankai Jia, Ye Tao, and Hongyuan Jiang. A Simplified Microfluidic Device for Particle Separation with Two Consecutive Steps: Induced Charge Electro-osmotic Prefocusing and Dielectrophoretic Separation. *Analytical Chemistry*, 89(17):9583–9592, September 2017.

[103] Ming Dao, Subra Suresh, Tony Jun Huang, Peng Li, Zhangming Mao, Zhangli Peng, Lanlan Zhou, Yuchao Chen, Po Hsun Huang, Cristina I Truica, Joseph J Drabick, and Wafik S El-Deiry. Acoustic separation of circulating tumor cells. *Proceedings of the National Academy of Sciences of the United States of America*, 112(16):4970–4975, April 2015.

[104] Siddhartha Tripathi, Y V.Bala Varun Kumar, Amit Prabhakar, Suhas S Joshi, and Amit Agrawal. Passive blood plasma separation at the microscale: A review of design principles and microdevices, August 2015.

[105] John Oakey, Josh Allely, and David W M Marr. Laminar-flow-based separations at the microscale. *Biotechnology Progress*, 18(6):1439–1442, November 2002.

[106] Jae Sung Park and Hyo Il Jung. Multiorifice flow fractionation: Continuous size-based separation of microspheres using a series of contraction/expansion microchannels. *Analytical Chemistry*, 81(20):8280–8288, October 2009.

[107] Lotien Richard Huang, Edward C Cox, Robert H Austin, and James C Sturm. Continuous Particle Separation Through Deterministic Lateral Displacement. *Science*, 304(5673):987–990, May 2004.

[108] Hong Miao Ji, Victor Samper, Yu Chen, Chew Kiat Heng, Tit Meng Lim, and Levent Yobas. Silicon-based microfilters for whole blood cell separation. *Biomedical Microdevices*, 10(2):251–257, April 2008.

[109] Thomas J Levario, Mei Zhan, Bomyi Lim, Stanislav Y Shvartsman, and Hang Lu. Microfluidic trap array for massively parallel imaging of Drosophila embryos. *Nature Protocols*, 8(4):721–736, March 2013.

[110] Roberto Fallica, Robert Kirchner, Helmut Schift, and Yasin Ekinci. High-resolution grayscale patterning using extreme ultraviolet interference lithography. *Microelectronic Engineering*, 177:1–5, June 2017.

[111] Javier Atencia, Susan Barnes, Jack Douglas, Mark Meacham, and Laurie E. Locascio. Using pattern homogenization of binary grayscale masks to fabricate microfluidic structures with 3D topography. *Lab on a Chip*, 7(11):1567–1573, 2007.

[112] Reza Amin, Stephanie Knowlton, Alexander Hart, Bekir Yenilmez, Fariba Ghaderinezhad, Sara Katebifar, Michael Messina, Ali Khademhosseini, and Savas Tasoglu. 3D-printed microfluidic devices. *Biofabrication*, 8(2):22001, June 2016.

[113] James Loomis, Dilan Ratnayake, Curtis McKenna, and Kevin M. Walsh. Grayscale lithography—automated mask generation for complex three-dimensional topography. *Journal of Micro/Nanolithography, MEMS, and MOEMS*, 15(1):13511, March 2016.

[114] Christopher Stilson, Rajan Pal, and Ronald A. Coutu. Fabrication of 3D surface structures using grayscale lithography. volume 8973, page 89730E. International Society for Optics and Photonics, March 2014.

[115] Monica Diez-Silva, Ming Dao, Jongyoon Han, Chwee-Teck Lim, and Subra Suresh. Shape and Biomechanical Characteristics of Human Red Blood Cells in Health and Disease. Technical report.

[116] Bernhard Sebastian and Petra S. Dittrich. Microfluidics to Mimic Blood Flow in Health and Disease. *Annual Review of Fluid Mechanics*, 50(1):483–504, January 2018.

[117] Fiona K. Glenister, Ross L. Coppel, Alan F. Cowman, Narla Mohandas, and Brian M. Cooke. Contribution of parasite proteins to altered mechanical properties of malaria-infected red blood cells. *Blood*, 99(3):1060–1063, February 2002.

[118] S. Suresh. Mechanical response of human red blood cells in health and disease: Some structure-property-function relationships. *Journal of Materials Research*, 21(8):1871–1877, 2006.

[119] Jae Youn Hwang, Jihun Kim, Jin Man Park, Changyang Lee, Hayong Jung, Jungwoo Lee, and K. Kirk Shung. Cell Deformation by Single-beam Acoustic Trapping: A Promising Tool for Measurements of Cell Mechanics. *Scientific Reports*, 6(1):27238, June 2016.

[120] S. Shin, J. X. Hou, J. S. Suh, and M. Singh. Validation and application of a microfluidic ektacytometer (RheoScan-D) in measuring erythrocyte deformability. *Clinical Hemorheology and Microcirculation*, 37(4):319–328, 2007.

[121] Quan Guo, Simon P. Duffy, Kerryn Matthews, Aline T. Santoso, Mark D. Scott, and Hongshen Ma. Microfluidic analysis of red blood cell deformability. *Journal of Biomechanics*, 47(8):1767–1776, 2014.

[122] Xianxian Chen, Lie Feng, Hua Jin, Shufen Feng, and Yao Yu. Quantification of the erythrocyte deformability using atomic force microscopy: Correlation study of the erythrocyte deformability with atomic force microscopy and hemorheology. *Clinical Hemorheology and Microcirculation*, 43(3):243–251, 2009.

[123] J. P. Mills, M. Diez-Silva, D. J. Quinn, M. Dao, M. J. Lang, K. S.W. Tan, C. T. Lim, G. Milon, P. H. David, O. Mercereau-Puijalon, S. Bonnefoy, and S. Suresh. Effect of plasmodial RESA protein on deformability of human red blood cells harboring Plasmodium falciparum. *Proceedings of the National Academy of Sciences of the United States of America*, 104(22):9213–9217, May 2007.

[124] Aline T. Santoso, Xiaoyan Deng, Jeong Hyun Lee, Kerryn Matthews, Simon P. Duffy, Emel Islamzada, Sarah M. McFaul, Marie Eve Myrand-Lapierre, and Hongshen Ma. Microfluidic cell-phoresis enabling high-throughput analysis of red blood cell deformability and biophysical screening of antimalarial drugs. *Lab on a Chip*, 15(23):4451–4460, 2015.

[125] Sergey S. Shevkoplyas, Tatsuro Yoshida, Sean C. Gifford, and Mark W. Bitensky. Direct measurement of the impact of impaired erythrocyte deformability on microvascular network perfusion in a microfluidic device. *Lab on a Chip*, 6(7):914–920, 2006.

[126] Hansen Bow, Igor V. Pivkin, Monica Diez-Silva, Stephen J. Goldfless, Ming Dao, Jacquin C. Niles, Subra Suresh, and Jongyoon Han. A microfabricated deformability-based flow cytometer with application to malaria. *Lab on a Chip*, 11(6):1065–1073, 2011.

[127] Marie Eve Myrand-Lapierre, Xiaoyan Deng, Richard R. Ang, Kerryn Matthews, Aline T. Santoso, and Hongshen Ma. Multiplexed fluidic plunger mechanism for the measurement of red blood cell deformability. *Lab on a Chip*, 15(1):159–167, 2015.

[128] Giovanna Tomaiuolo, Luca Lanotte, Rosa D'Apolito, Antonio Cassinese, and Stefano Guido. Microconfined flow behavior of red blood cells. *Medical Engineering and Physics*, 38(1):11–16, January 2016.

[129] Yi Zheng, John Nguyen, Chen Wang, and Yu Sun. Electrical measurement of red blood cell deformability on a microfluidic device. *Lab on a Chip*, 13(16):3275–3283, August 2013.

[130] Edward J. Felton, Anthony Velasquez, Shulin Lu, Ryann O. Murphy, Abdala Elkhal, Ofer Mazor, Pavel Gorelik, Anish Sharda, and Ionita C. Ghiran. Detection and quantification of subtle changes in red blood cell density using a cell phone. *Lab on a Chip*, 16(17):3286–3295, 2016.